Transverse flow in 158 AGeV/c Pb+Pb at the CERN SPS

By

LYNN SCOTT WOOD

B.S. (Lewis and Clark College) 1991

M.S. (University of California, Davis) 1993

DISSERTATION

Submitted in partial satisfaction of the requirements for the degree of

DOCTOR OF PHILOSOPHY

in

Physics

in the

OFFICE OF GRADUATE STUDIES

of the

UNIVERSITY OF CALIFORNIA

DAVIS

Approved:

Committee in Charge

1998

Lynn Scott Wood
June 1998
Physics

Transverse flow in 158 AGeV/c Pb+Pb at the CERN SPS

Abstract

Transverse flow of particles in nucleus-nucleus collisions has been studied at beam energies from 10 A·MeV up to 10 A·GeV at the AGS accelerator at Brookhaven National Laboratory. Recently, heavy-ion beams of 160 A·GeV Pb ions have been studied at the CERN SPS. This thesis examines transverse flow measurements at this energy and compares results to measurements at lower energies. In particular, any possible significance for detection of the quark-gluon plasma will be discussed.

The NA49 detector system was designed to provide wide coverage of the many charged particles, but the actual acceptance in the azimuthal angle (critical for transverse flow measurements) is far from perfect. Acceptance correction methods for the detectors are discussed and evaluated.

Acknowledgements

I would like to thank my advisor, Daniel Cebra, for saying to me the now immortal words, "Why don't you look at transverse flow?" as well as his continuing support and optimism. During my graduate student years, Paul Brady and Ramona Vogt also provided valuable advice and information. I would also like to especially thank Jim Draper for his efforts alongside mine in this research. In my time at U.C. Davis, I have greatly appreciated the nuclear physics group, both the group I started with and the new, younger group that I am leaving behind.

I am grateful to the NA49 Collaboration for allowing me to participate in this exciting process of discovery. In particular, Art Poskanzer of Lawrence Berkeley National Laboratory provided valuable assistance in the transverse flow studies.

I thank my parents for loving me and for their constant encouragement of my interests. I will be forever grateful to my wife Valerie for marrying me despite knowing that I would have to go through all this, and for her unfailing love and support during this lengthy process.

Most of all, I thank my God for giving me a mind that can not only examine the physical world in minute detail, but can also feel awe at the wonders He has created.

This work was supported by U.C. Davis and the National Science Foundation under grant PHY-96-01271.

Contents

List of Figures

List of Tables

Chapter 1

Introduction

1.1 Overview

This thesis examines transverse flow measurements at the CERN Super Proton Synchrotron (SPS), which currently provides the highest densities and temperatures of nuclear matter possible in the laboratory. Transverse flow has been measured extensively at lower beam energies (up to about 1.2 A·GeV) and more recently at AGS energies (up to 10 A·GeV) [Reis98]. With the large acceptance of the NA49 experiment at the CERN SPS, transverse flow measurements at 160 A·GeV are now possible and have been done for protons and pions.

Chapter 1 provides an introduction to the nuclear equation of state and transverse flow; chapter 2 describes the NA49 experiment itself; chapter 3 examines the particle identification possible in NA49; chapter 4 describes the methods used to measure transverse flow; chapter 5 describes the problems with acceptance in the detectors and their affect on transverse flow; chapter 6 discusses results; and chapter 7 presents conclusions.

1.2 Heavy-Ion Reactions

All common knowledge of nuclear matter comes from studies near the ground state – but many situations occur where nuclear matter is expected to be far from the ground state, a common occurrence in astrophysics and cosmology. The cores of neutron stars are believed to consist of nuclear matter at densities of about four times normal nuclear matter [Glen89]. The state of matter in the early universe in the Big Bang model is thought to consist of a "quark-gluon plasma", an ultradense soup of unbound quarks and gluons. All of these situations can only be examined at stellar distances, but the hope of heavy-ion reactions is to provide nuclear matter densities and temperatures in the laboratory that approach these levels and provide insight into the state of nuclear matter at extreme temperatures and densities.

To attain these extremes, heavier and heavier nuclei have been accelerated to higher and higher energies, from Au ions at $\sqrt{s}$ = 1.5 A·GeV [1] at the Bevalac at Lawrence Berkeley National Laboratory in the 1980's up to the presently running Pb ions at $\sqrt{s}$ = 17.3 A·GeV at CERN's SPS. About a year from now, antiparallel Au ion beams will intersect at $\sqrt{s}$ = 200 A·GeV at the Relativistic Heavy Ion Collider at Brookhaven National Laboratory. And, within the next decade, the Large Hadron Collider planned at CERN will accelerate Au ions to a center-of-mass energy of $\sqrt{s}$ = 5.5 A·TeV.

Figure 1.1 shows a simplified view of a relativistic heavy-ion collision. In the top picture, the two nuclei are approaching one another at a particular impact parameter. This impact parameter is random, but can be selected to some degree in a heavy-ion experiment to study effects of event centrality. In the middle picture, the two ions are colliding. The nucleons in the overlap region are squeezed together and lose most of their momentum as pressure and temperature increase rapidly. In the bottom picture, the interaction between the two ions is over. The "spectator" remnants of the ions that did not collide continue on at their initial velocities, while the nucleons that were compressed rebound, expanding in all directions, but mostly longitudinal.

During the actual collision, the particles in the overlapping regions of the two nuclei experience extreme changes in density – up to ten times normal nuclear matter at SPS energies. This part of the sequence is currently of the most interest to nuclear physicists, but is also the most difficult to observe. After the collision, the participant

[1] $\sqrt{s}$ is the total energy of the system in the center-of-mass frame.

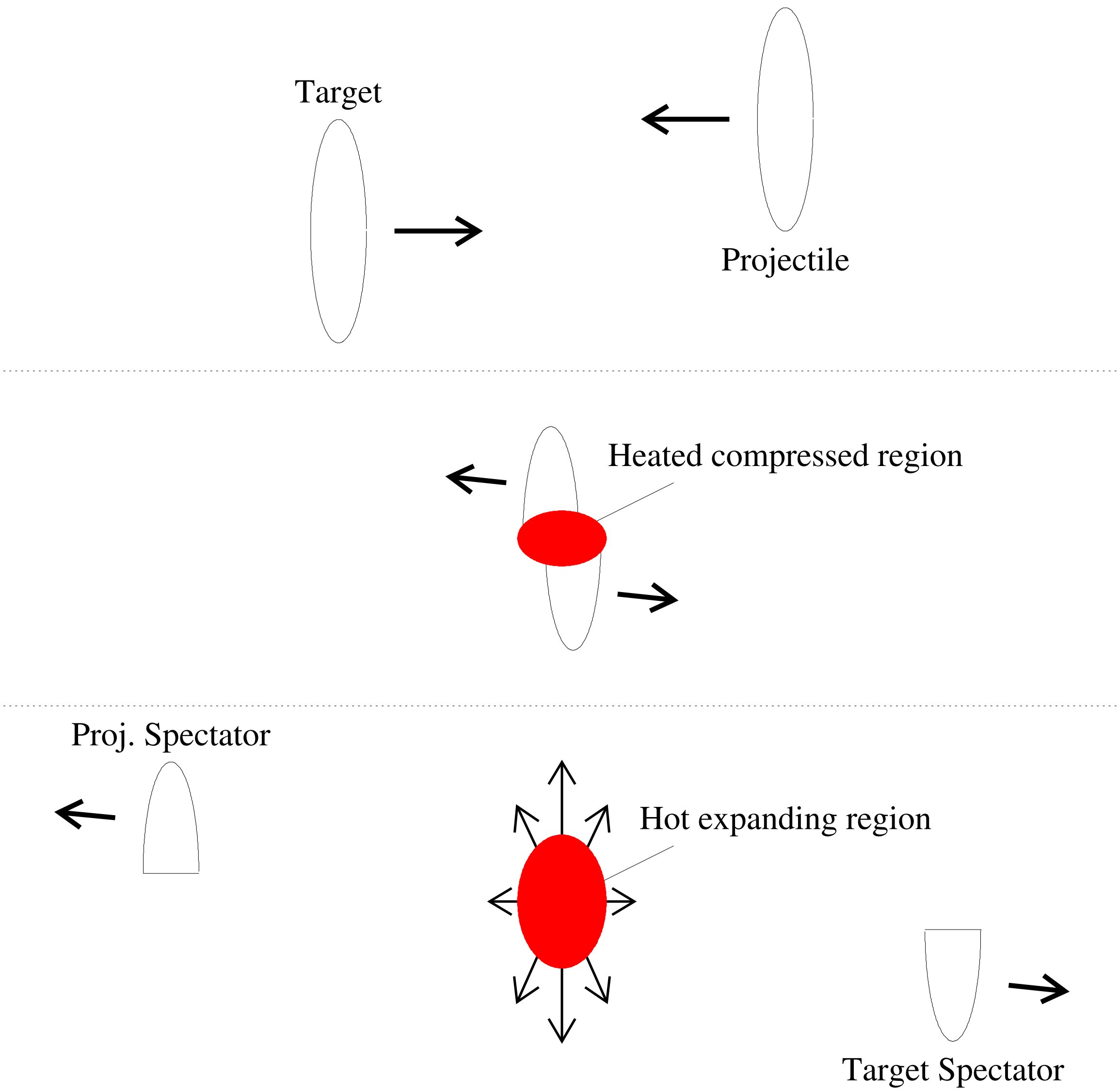

Figure 1.1: Simple picture of a medium-bias heavy-ion collision, center of mass view. Top: target and projectile approach each other. Middle: as the nuclei collide, the central region is heated and compressed between the two uncolliding remnants. Bottom: the spectator fragments continue traveling with nearly the same velocity, while the previously compressed region expands outward.

particles expand outward, effectively "erasing" any of the high densities achieved during the collision. Any information about the dense region of the collision must be inferred from these measured particles.

Figure 1.2 shows the generally-accepted phase diagram for nuclear matter. Normal nuclear matter lies at the point "nm" in the figure, where $\rho_{nm} = 1.4 \text{ fm}^{-3}$ and the temperature is near 0 MeV. At higher temperatures, the nucleons are able to overcome the binding energy of the nucleus and a "hadron gas" is formed, consisting of unbound hadrons in an ideal gas-like phase. At still higher temperatures and/or densities, the nucleons may be squeezed so close together that individual nucleons will be poorly-defined, and a plasma-like state of quarks and gluons will be formed. The QGP will be discussed more in section 1.2.2.

1.2.1 The Nuclear Equation of State

The often-stated goal of these experiments is to produce the quark-gluon plasma (QGP), but a great deal of other nuclear physics can be learned as well. Of particular interest are insights to the equation of state of nuclear matter.

The equation of state (EOS) can be written with three terms [Stöc86]:

$$W(\rho, T) = E_T(\rho, T) + E_C(\rho) + W_0$$

where W is the energy per baryon, ρ is the density, and T is the temperature. The first term, E_T, represents the thermal energy, while the second, E_C, represents the compressional energy. The third term, W_0, is the rest energy of a nucleon, defined as 923 MeV = (939 MeV - 16 MeV) when the binding energy of a nucleon in a nucleus is subtracted out.

The compressional energy term is of particular interest. It is clear that $E_C = 0$ for dilute nuclear matter ($\rho = 0$), and that it is at a minimum at normal densities. It is typically modeled as

$$E_C(\rho) = \alpha(\rho/\rho_0) + \beta(\rho/\rho_0)^\sigma$$

where $\sigma > 1$, $\alpha > 0$, and $\beta < 0$. If the values of α and β are fixed by matching to the correct binding energy and normal nuclear matter density, then σ will be determined

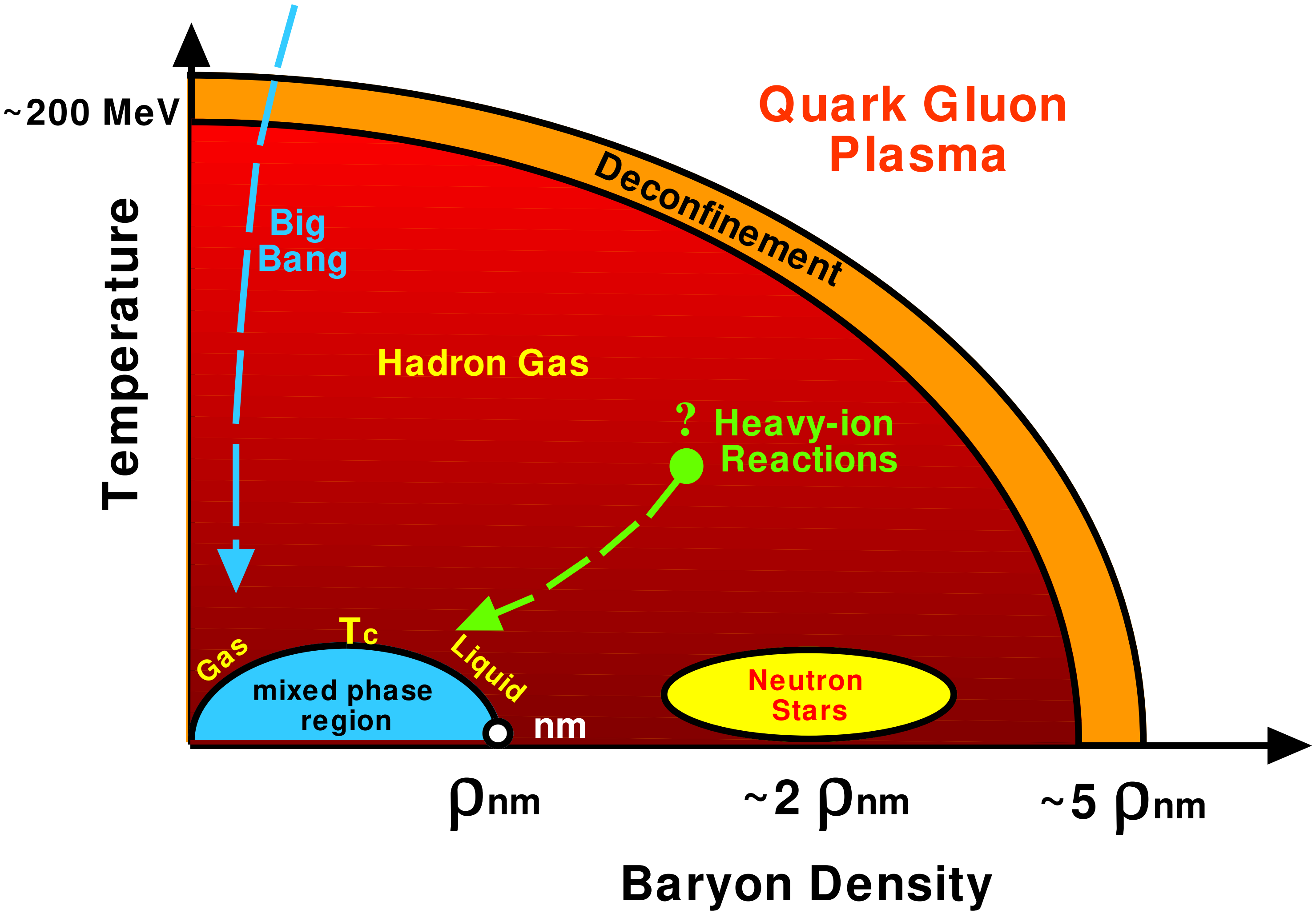

Figure 1.2: Phase diagram of nuclear matter [Kint95].

by the compressibility.

In reality, it is quite difficult to determine any of these properties (temperature, density, compressiblity) of nuclear matter – as mentioned above, they must all be inferred from some other measurement. Some ideas about the compressibility have been found through analysis of monopole resonances [Blai76, Pear91], providing a value for the bulk modulus of nuclear matter of $K = 210 - 220$ MeV. Analysis of neutron stars [Glen89] has also provided some information about the incompressiblity, providing a lower limit of $K > 200$ MeV. However, theoretical models of supernovae explosions [Latt96] require much softer equations of state, with $K \sim 180$ MeV.

The idea of an equation of state for nuclear matter only applies, of course, if the system is in global thermal equilibrium. If that is not the case (it will not be for a phase transition into the QGP), then the idea of an equation of state is poorly defined in that system, although once above the phase transition an equation of state could again be defined. Whether this is the case or not in the NA49 experiment remains to be determined.

1.2.2 The Quark-Gluon Plasma

Of pressing interest to this thesis is whether the nucleons in a heavy-ion collision are compressed to a high enough density to undergo a phase transition to a quark-gluon plasma. Recent lattice QCD calculations [Kars95, Laer96] have confirmed a critical temperature $T_c \sim 150$ MeV (which corresponds to an energy density of $\epsilon_c \sim$ 1-3 GeV/fm^3) for the transition of a hadronic system into the QGP.

Of great concern is our ability to recognize when a quark-gluon plasma has been formed. As mentioned earlier, few direct clues from the highly-compressed part of an heavy-ion collision remain to be examined by experimental detectors. A number of signatures have been suggested, each with its own advantages and drawbacks. Several will be discussed here (for other signatures, see [Cser94, Wong94, Harr96]).

Electromagnetic probes: Photons and leptons formed in the QGP are considered to be some of the cleanest signals since they will interact only weakly with the hadronic matter surrounding the collision region. A quark and antiquark in the QGP can produce a lepton pair via a virtual photon: $q+\overline{q} \rightarrow \gamma^* \rightarrow l^+ + l^-$. Similarly, direct photons can be produced in the QGP. The difficulty in measuring these signals lies in clean identification of the particles as arising from the QGP and not one of many other sources. Drell-Yan lepton pair production, vector meson decay, and hard interactions at early stages of the experiment all produce lepton pairs that form a large background. Similarly, large numbers of π^0 and η produced in heavy-ion collisions produce a large γ background [Cser94].

J/Ψ **suppression**: The J/Ψ consists of a $c\overline{c}$ quark pair and has a easily identified $\mu^+\mu^-$ decay mode. A suppression of J/Ψ production when compared to the Drell-Yan background has been predicted [Mats86] due to color screening effects in the QGP (similar to the charge-screening effects of a normal plasma). The $c\overline{c}$ pairs typically form a bound state soon after their creation, but if this creation occurred in a QGP then the color screening effects present would reduce the occurrence of a $c\overline{c}$ bound state, producing D mesons instead. More recent studies have shown that a variety of absorption methods of the J/Ψ in normal hadronic matter can also produce the same effect [Vogt91, Gavi97], However, new results from the NA50 experiment at the CERN SPS [Abre97] have shown significant deviation of the J/Ψ production rate in 158 GeV/c Pb+Pb collisions from the trends seen in smaller systems and lower energies.

Strangeness enhancement: In a nucleus-nucleus interaction, $s\overline{s}$ pairs can be formed and will produce strange particles. In the QGP, this will also occur, but the free interaction of quarks and gluons may produce "chemical equilibrium", where the number of particles of each type is in a balanced state. If this is the case, many more $s\overline{s}$ pairs will be produced than are in nucleus-nucleus collisions. This effect is known as "strangeness enhancement", and can be studied by comparing the yields of strange particles to normal ones (i.e. K^+/π^+). This result, however, can be complicated by several things, including whether the QGP actually reaches chemical equilibrium [Wong94] and enhanced production of strange particles in the baryon-rich dense region surrounding the collision [Brow91]. Measuring ratios of doubly- and triply-strange particles (i.e. Ξ^- and Ω^-) has been studied to reduce these uncertainties (see [Judd95, DiBa95] as examples). In addition, the correlation of strangeness enhancement with other signals such as total multiplicity have been studied [Lete92].

Transverse flow: Collective effects of the many nucleons in a heavy-ion collision can provide useful information about the event itself. One effect, and the topic of this thesis, is transverse flow, or the flow of particles in the plane at right angles to the beam. This effect is directly related to the equation of state, and is possibly a sensitive probe to the state of the nuclear matter during the collision. Near the phase transition region the equation of state becomes "soft", and transverse flow will be small. Beyond the phase transition, transverse flow should again increase. Recent experimental results [Agga97, Ahle98, Appe98] have shown, however, that transverse flow is more difficult to observe at large beam energies, making the signal more difficult to determine. This will be discussed in more detail in the next section.

An additional complication to all QGP signatures is the uncertainty whether any QGP formed will actually be in thermal equilibrium or not. Indeed, many of the QGP models used to study possible signals assume a large region of thermally-equilibrated plasma. In reality, however, things will be more complicated: there could very well be regions of QGP mixed with regions of hadronic matter [Prat98], and the finite size of the QGP region has a definite effect on the actual phase transition [Spie98] – the picture is complicated further.

As can be seen, there appears to be no single obvious signal for the quark-gluon plasma. Modern experiments attempt to examine multiple signals simultaneously to look for changes indicating that a quark-gluon plasma has been formed. Indeed, current correlations between various QGP signatures are creating a promising picture that the QGP may have indeed been created at the SPS [Gazd98], but the final decision is far from over.

1.3 Transverse Flow

The compression and resulting expansion in a heavy-ion collision produces a collective "flow" of particles. These effects are usually broken down into several components:

- *longitudinal flow* – along the beam direction;
- *transverse flow* – at right angles to the beam direction; and
- *radial flow* – an azimuthally symmetric overall flow measurement.

This thesis will concentrate on transverse flow. Radial flow measurements are currently of interest due to their effects on the p_T spectra of particle types [Siem79, Naga81]. Longitudinal flow is not in itself studied as often since it is more difficult to determine at high beam energies.

The ideas behind this collective motion were first motivated by Landau's hydrodynamic treatment of nucleon-nucleus collisions [Land53] which utilized the equation of state of a relativistic gas. Later studies used ideal hydrodynamic models to examine the effects of shock waves during nucleus-nucleus collisions [Sche74]. In particular, it was shown that soon after the collision the transverse motion of the stopped nucleons was greater than that of the forward-going nucleons, i.e. nucleons were being pushed outward in the plane transverse to the incoming nuclei.

The first evidence of this collective motion was seen at the Bevalac in the Streamer Chamber and Plastic Ball detectors [Gust84, Renf84] in 1984. Of more importance was the fact that the collective flow observed could be reproduced by a theoretical hydrodynamic model [Stöc86], supporting the hydrodynamic nature of the flow. Transverse flow has since been studied in great detail at lower energies at a variety of accelerators, including the Bevalac, Michigan State University, and the GSI SIS (see [Reis98] for a current review), and experiments at the AGS are now reporting detailed results [Barr94, Hemm96, Barr97, Ahle98, Liu97]. Experiments at the SPS have just recently started reporting results [Wein96, Agga97, Appe98].

The collective motion of the particles is shown in graphical form in figure 1.3. The ellipsoid on the top half of the figure represents the flow of all particles involved in the collision, and the angle θ_{flow} is nonzero in events with transverse flow. One of the earlier methods of searching for flow was to determine θ_{flow}, but as beam energies increase θ_{flow} becomes too small to measure – at SPS beam energies θ_{flow} was calculated to be much less than one degree. The bottom half of the figure is a

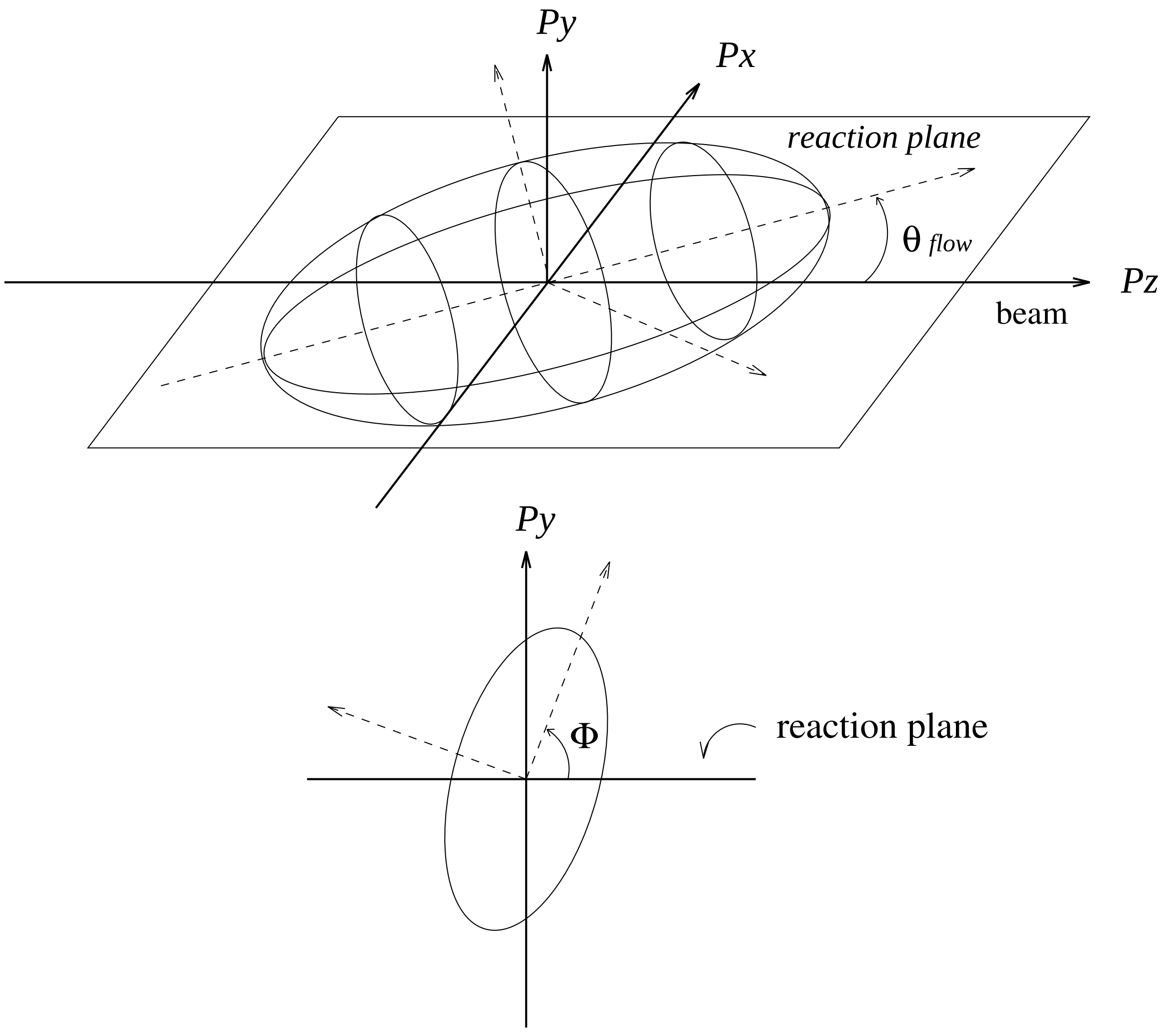

Figure 1.3: Flow ellipsoid in the center-of-mass frame(from [Huan97]). The ellipsoid represents the distribution of the momenta of particles emerging from the collision. The bottom figure looks along the major axis of the ellipsoid, within the reaction plane along the direction of θ_{flow}. The angle Φ represents the orientation of the semimajor axis of the ellipse.

cross-sectional view of the flow ellipsoid looking down the longest axis, in the direction of θ_{flow}. This is the distribution that is looked at to measure flow. Note that at SPS beam energies this plot is effectively the $p_x - p_y$ plane.

The traditional measure of transverse flow is to examine the mean transverse momentum of the particles with respect to the reaction plane (see figure 1.3 in a single event as a function of rapidity). An example of this can be seen in figure 1.4 for the EOS experiment. The mean transverse momentum of the particles measured along the reaction plane is plotted vs. the normalized rapidity $y_N = (y - y_{CM})/y_{CM}$. This renormalization of the rapidity is done to allow comparison of flow values at different beam energies. As should be expected from the top of figure 1.3, the flow is positive above midrapidity and negative below. The details of how these calculations are made, including the critical task of finding the event plane, will be discussed in detail in chapter 4.

Recent work to measure flow using detectors without any momentum measurement capability [Barr94, Hemm96, Barr97, Wein96, Huan97] raised interest in a new flow measurement method. By not using p_T in the flow calculation, anisotropies in azimuthal distribution of number are measured. This has proven to be a useful tool and is expected to play a big role in flow measurements in the future.

Another flow measurement of interest is elliptical flow – the measure of flow distributions that have $\cos(2\phi)$ dependence. This was first seen at the Bevalac as "squeeze-out" of protons [Gutb90] and of pions [Kint95]. Squeeze-out is defined as the emission of particles at right angles to the event plane. In figure 1.3b, the elongation of the ellipsoid in the p_y direction would be a squeeze-out signal. At AGS energies, it has been seen that the squeeze-out effect rotates into the reaction plane – this has also been seen at SPS energies.

This elliptical measurement can and has been generalized with the azimuthal anisotropy method, and has been measured at AGS and SPS energies. This higher-order flow is of scientific interest as well: recent studies [Sorg97] have suggested that measurements of elliptical as well as radial flow will provide detailed information about the pressures the particles feel at several times during the collision. In addition, elliptical flow has been seen to be greatest at midrapidity, the region that most RHIC

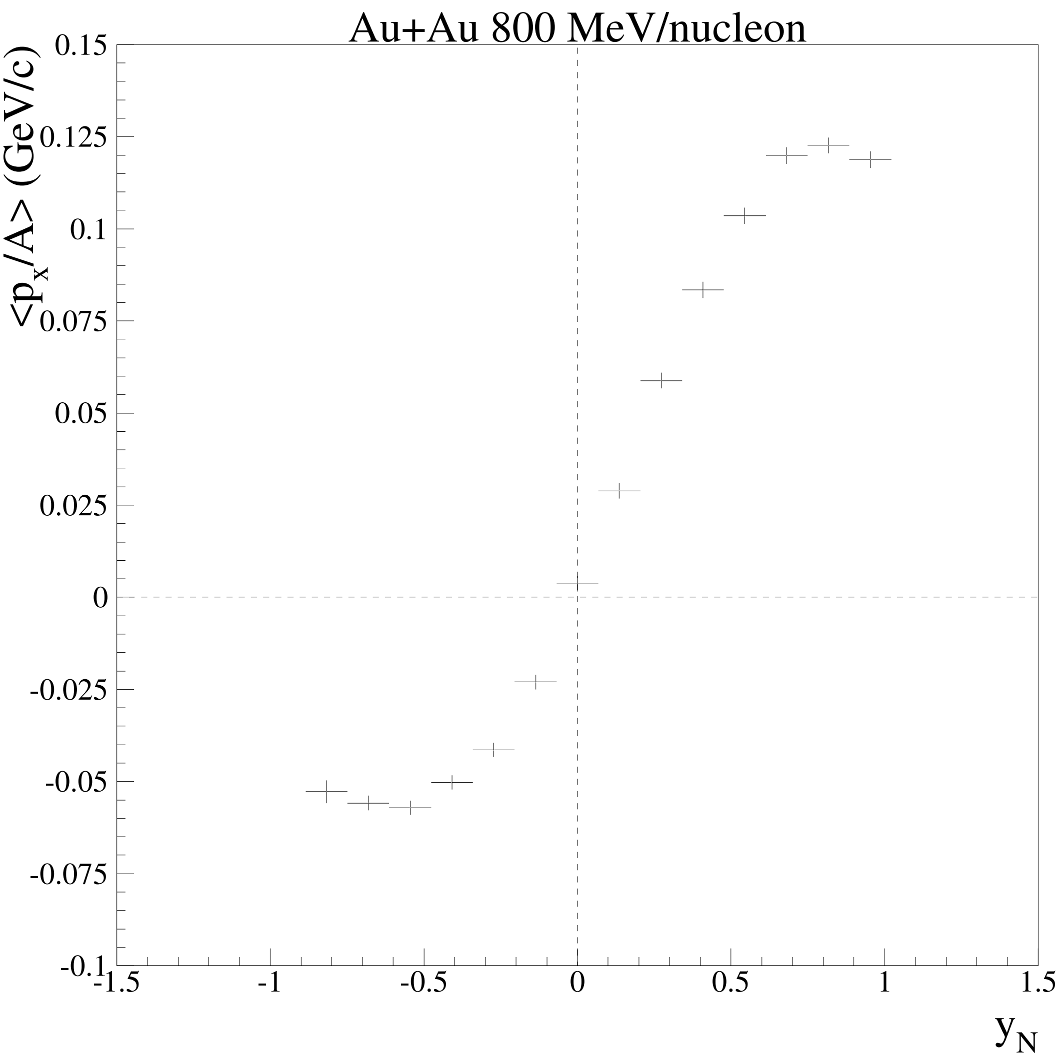

Figure 1.4: Transverse flow measurement from the EOS experiment [Part95]. The vertical axis is the mean transverse momentum per particle along the reaction plane, and the horizontal axis is the normalized rapidity. The asymmetry between the forward and backward regions of rapidity is due to acceptance biases.

and LHC experiments plan to examine in detail. For contrast, it can be seen in figure 1.4 that transverse flow goes to zero at midrapidity.

The particles most often measured for flow signal are the participant protons, since they are directly experiencing the compression and expansion during the collision. Flow measurements of other particles also have interesting aspects, however. It was mentioned above that charged pion flow and squeeze-out has been examined at Bevalac energies. In addition, pion transverse and elliptical flow has been measured at the AGS [Hemm96, Barr97, Ahle98] and SPS [Appe98]. Another interesting result is the flow of neutral pions measured at the SPS experiment WA93 [Agga97]. Kaon flow is believed to be a probe of the kaon potential inside the nucleus [Li95], and further examination of this is planned at the AGS [Ogil98]. Antiprotons have been seen to "anti-flow" against the proton flow at the AGS [Brau93] and has been predicted for SPS energies [Jahn94]. Finally, it should be pointed out that a number of experiments have measured transverse flow of a variety of nuclear fragments as well [Gust88, West90, Part95].

Chapter 2

The NA49 Experiment

2.1 Overview

NA49 is a fixed-target experiment at the CERN Super Proton Synchrotron (SPS), and was designed specifically for the 158 GeV/nucleon Pb beam first made available in 1994. Pb+Pb interactions at these energies produce the highest energy density currently available to experiments.

Approximately 1500 charged particles are produced in a central Pb+Pb event, and the NA49 detectors were designed to maximize the number of these particles detected. Two time projection chambers (TPCs) are placed in large dipole magnets, the first with a field of 1.5 Tesla, and the second 1.1 Tesla, to measure charged particle momentum and search for neutral particle decays. Two larger TPCs are located downstream of the magnets and determine the trajectories of charged particles in the forward half of center-of-mass phase space ($y > 2.9$). Particle identification is done in these TPCs by energy loss measurements dE/dx and time-of-flight (TOF) detectors located behind them. A veto calorimeter was used to measure projectile spectators and determine impact parameter for triggering on selected events. In separate runs with the magnets turned off, a ring calorimeter was used to measure the transverse energy of the particles.

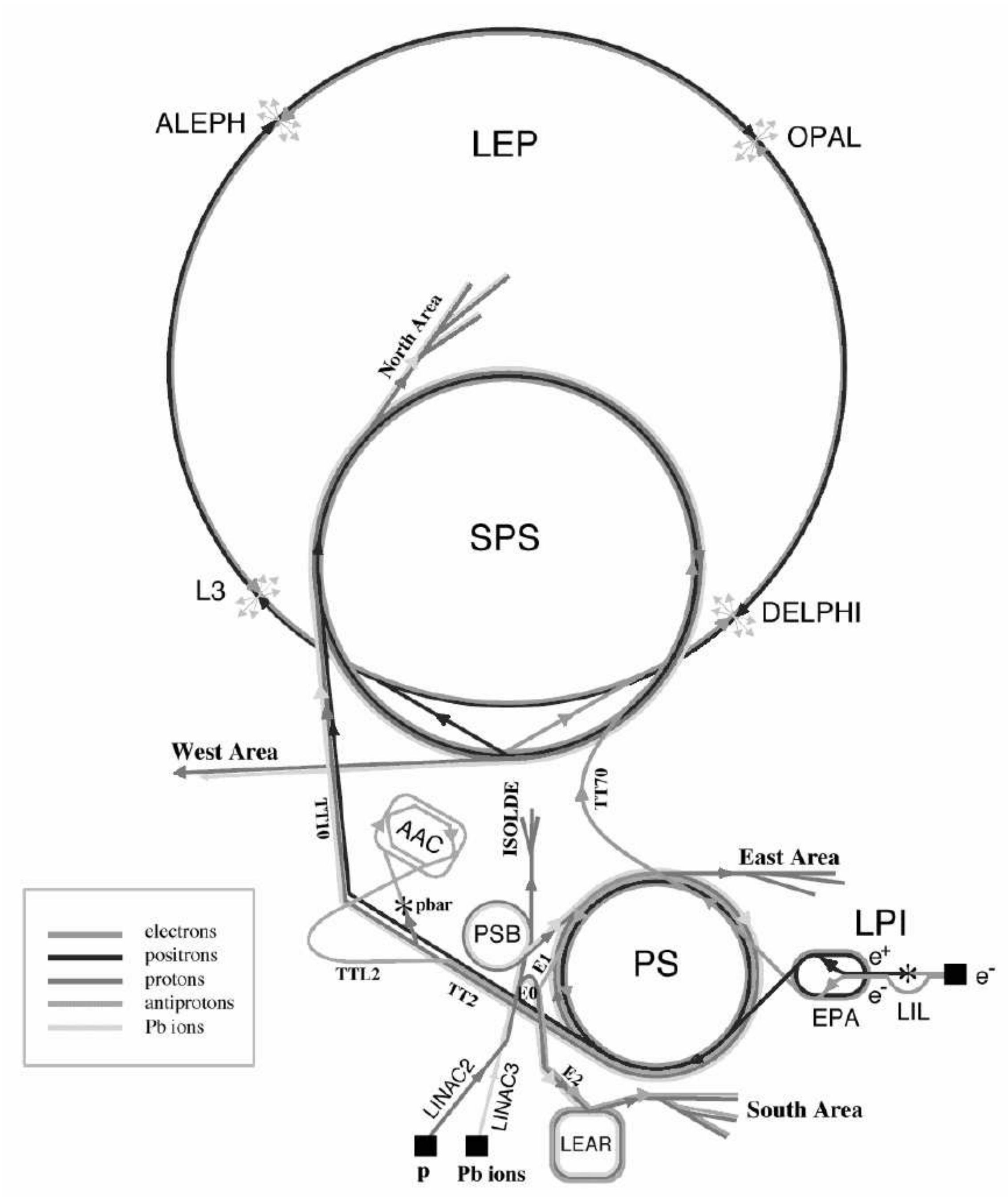

Figure 2.1: The CERN Accelerators (CERN image archive).

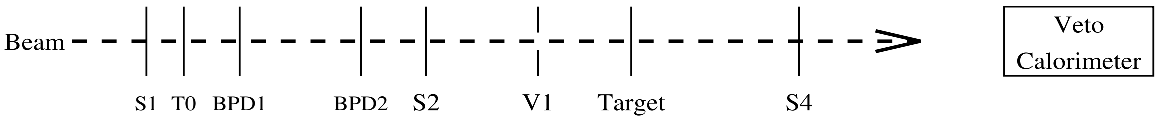

Figure 2.2: The NA49 trigger detectors (note that this figure is not to scale). S1, S2, and S4 are thin quartz Čerenkov counters, V0 and V1 are scintillator counters with 1 cm holes in the center, and BPD1 and BPD2 are beam position detectors.

2.2 The SPS Accelerator

The Pb ions used in NA49 are produced by a linear accelerator, injected into the Proton Synchrotron booster where they are accelerated to 95 A·MeV/c, then passed into the Proton Synchrotron (PS) and accelerated to 4.5 A·GeV/c. From there, they are injected into the Super Proton Synchrotron which accelerates them in its 26.7 km circumference tunnel (see figure 2.1). NA49 is located in the north experimental area of the SPS. The SPS is currently capable of accelerating Pb ions to momenta of 158 GeV/c per nucleon, lighter ions like sulphur up to about 200 GeV/c per nucleon, and protons up to 450 GeV/c.

2.3 Triggers and Targets

The NA49 experiment has now received Pb beams for about one month per year for three years, starting in 1994 (due to a fire at the SPS in 1997, NA49 had a proton run that year). The majority of data from these runs used a 197 μm thick Pb target and the "central" trigger, which selected events with an impact parameter of less than 3.3 fm by examining the energy deposited in the veto calorimeter. This corresponds to 5% of the total Pb+Pb cross section. Some data has been taken with a 758 μm target during each year as well, and has been used to determine detector placement.

A variety of detectors are used to determine the beam trigger (see figure 2.2):

- two thin quartz wafer Čerenkov counters, S1 and S2, upstream from the target,
- two scintillation counters, V0 and V1, with 1cm holes in the center,
- another quartz Čerenkov counter, S4, downstream of the target,

- a scintillator counter, T0, to start event timing, and

- two beam position detectors, BPD1 and BPD2.

Čerenkov counters S1 and S2 define the start signal, while V0 and V1 are used to detect particle "halos" around the beam that signify a reaction upstream from the target (i.e. a beam-gas interaction or interaction within S1 or S2). Another counter, S4, is placed behind the target to detect the signal from spectator fragments.

Clear beam signals in S1 and S2 show that no interaction occurred upstream from the experiment, while the lack of a signal in V0 shows that the beam has passed through the hole and no "halo" particles are present. The lack of a strong signal in S4 indicates that an interaction has taken place in the target. A valid beam event is thus defined by the coincidence of signals in S1 and S2 but no signals in V0 and S4.

During the 1995 run, approximately 59,000 events were taken with a "medium-bias" trigger, which selected events in which the energy deposited in the veto calorimeter was 45-60% of the beam energy. This corresponds to impact parameters from 6.5-9.0 fm, with a mean of approximately 7.7 fm, or about 14% of the total cross section (for this calculation, see appendix B). The expected distribution of impact parameters is shown in figure 2.3. These medium-bias events were utilized for the transverse flow measurements in later chapters.

Minimum-bias data were taken during the 1996 run. These data would allow a selection of various impact parameters via particle multiplicity and veto calorimeter energy cuts; unfortunately, it has not yet been run through the production chain to produce data usable for analysis. More medium-bias data was planned to be taken in 1997, but an accident at CERN required a proton beam to be run instead. Luckily, it is possible to see a flow signal in the existing data, although more statistics would be helpful.

2.4 The Magnets

Two superconducting dipole magnets are placed directly behind the target, the first with a field of 1.5 Tesla and the second at 1.1 Tesla. This field allows determina-

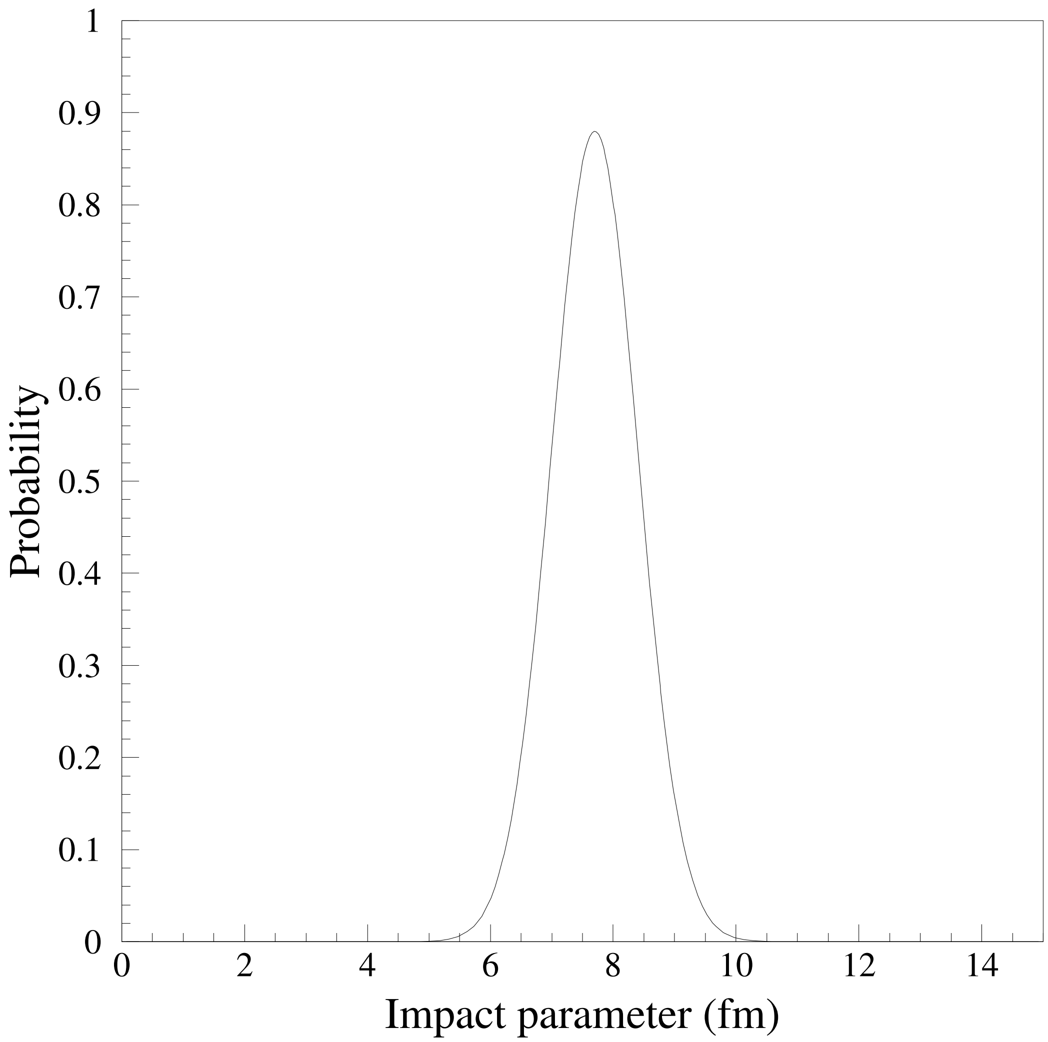

Figure 2.3: Expected distribution of impact parameter using the medium-bias trigger. The plot is normalized such that the probability on the vertical axis represents that chance that a medium-bias event will have that impact parameter [Huan96].

Trigger	b **(fm)**	**Fraction**
Central	< 3.3	5%
Medium-bias	$\sim 6.5 - 9.0$	14%

Table 2.1: Standard run triggers for NA49.

	VTPCs	MTPCs
Gas mix	91% Ne/9% CO_2	91% Ar/4.5% CH_4/4.5% CO_2
Size (m)	2.60 x 2.00 x 0.72	3.84 x 3.84 x 1.29
Number of Pads	27,648	63,360
Pad size	3.00 mm x 28 mm	High-res: 3.13 mm x 39 mm
		Standard: 4.95 mm x 39 mm

Table 2.2: Data on the NA49 time projection chambers [Beis96].

tion of momentum in the detectors placed within the magnets, but also help "sweep" low-momentum pions outwards from the beam path, reducing the track density in the main TPCs.

2.5 The Time Projection Chambers

The many detectors in NA49 (see figure 2.4) were selected and positioned to maximize the number of charged particles tracked and identified. To this end, four large TPCs were installed, a "vertex TPC" (VTPC) in the center of each dipole magnet, and a large "main TPC" (MTPC) on either side of the beampipe further downstream. A TPC provides three-dimensional tracking ability and particle identification over a large volume.

2.5.1 The NA49 TPCs

The NA49 TPCs consist of a large gas-filled drift volume, a multi-wire proportional section, and a readout pad plane. A field cage surrounds the active volume, generating an electric field that provides a constant drift upwards velocity for electrons in the volume. NA49 used an innovative design for the field cage. Because of the large size of the TPCs, the weight of a standard copper-strip field cage would present a problem. Instead, aluminized mylar strips were carefully wound around ceramic posts in the corners of the TPC to form a much lighter field cage (see figure 2.5). This also cuts down dramatically on the number of particle interactions in the field cage.

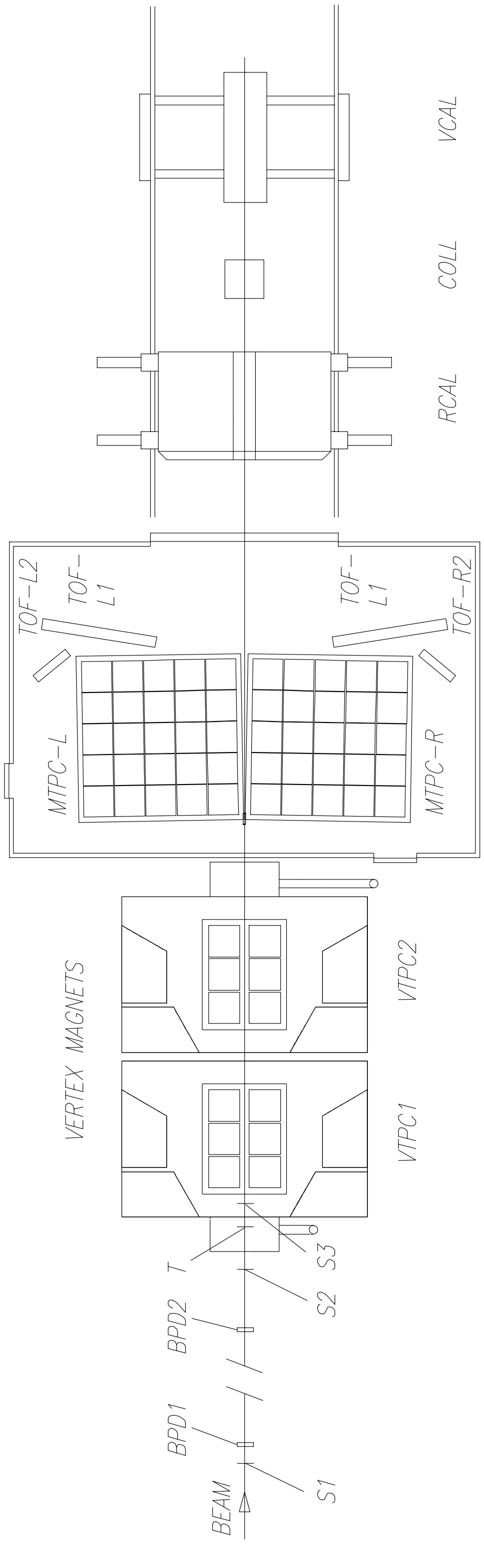

Figure 2.4: The NA49 experimental setup (NA49 image archive).

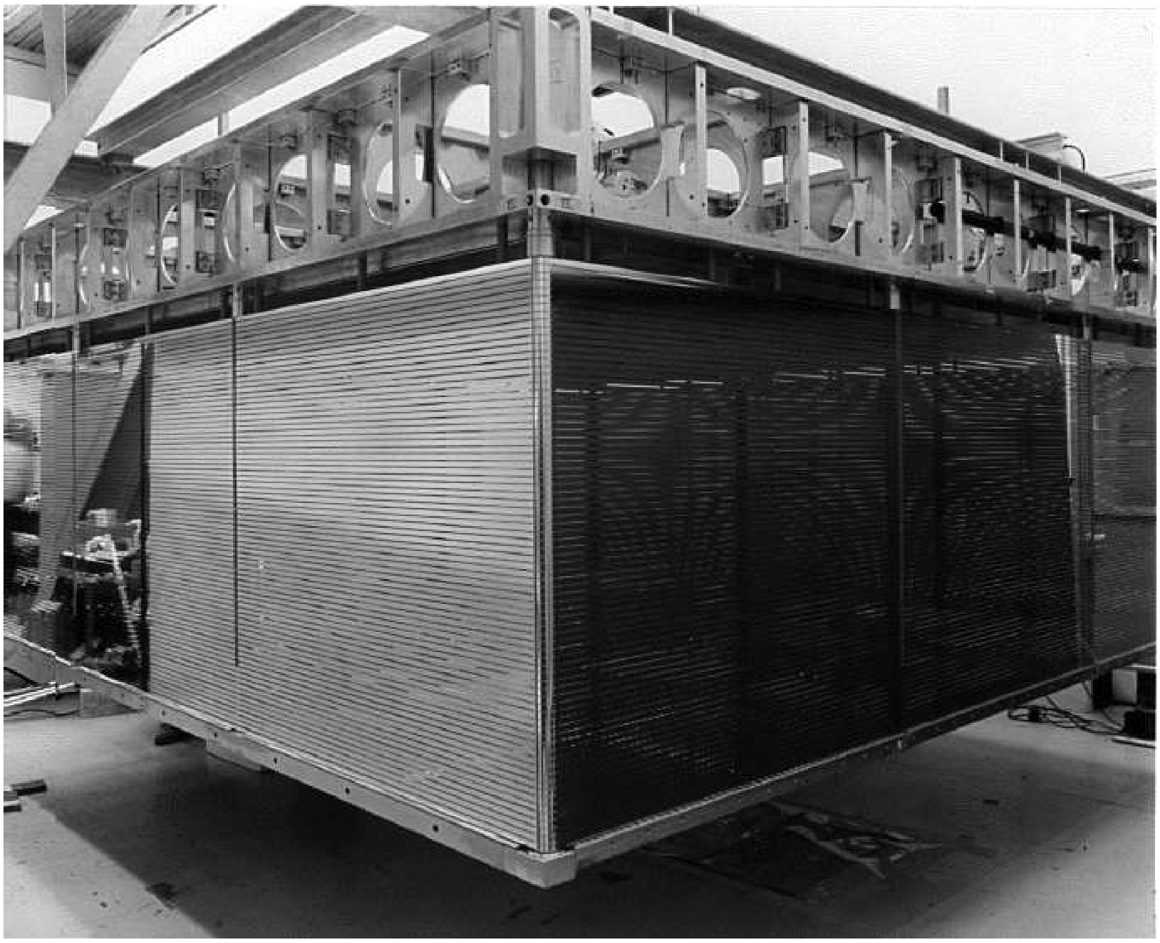

Figure 2.5: External view of one of the main TPCs. Note the mylar strips that form the fieldcage, minimizing both weight and material (NA49 image archive).

In the top few mm of the TPCs, several wire planes provide multiplication of the drifting electron signal. The pad plane consists of many small pads of various sizes (depending on the detector and track density expected) where the charge is collected and read out.

Both the VTPCs and the 20% of the MTPCs nearest the beampipe are considered "high-density" regions with high particle track densities, and have smaller pad widths than the rest of the MTPCs (3 mm vs. 5 mm). All pads in the MTPCs are also longer, to enable better samples of the energy loss (39 mm vs. 28 mm). In the VTPCs and the outer 60% of the MTPCs, the pads are angled to better align with the track trajectories.

When a charged particle travels through the TPC, it ionizes gas molecules along its path. These electrons drift upward at a constant velocity until they reach the first wire plane, which is grounded to shield the drift volume from the high voltages in the multiwire region. After the electrons pass through, they are rapidly accelerated towards the high-voltage "sense" wire plane until they also ionize the gas, providing an avalanche of electrons onto the sense wire. Meanwhile, an image charge from the ions created by this ionization is generated on the pad plane. This signal is read out for analysis. The third wire plane, known as the "gating" grid, is normally at ground, but after the avalanche on the sense grid its wires have alternating voltages placed on them. This prevents the large cloud of positive ions generated by the avalanche from drifting back into the active volume, where they would recombine with drifting electrons and reduce the signal.

The actual particle tracks are obtained from the pad information. Because the drifting electrons spread out with time, a "cluster" of charge forms and spreads over several pads. The centroid of this cloud can be found to determine the x position, while the z position (in the beam direction) is taken to be the center of the pad row. Finally, the y position can be found by measuring the amount of time it takes for the charge cloud to reach the pad plane (the drift velocity is constant in the NA49 TPCs).

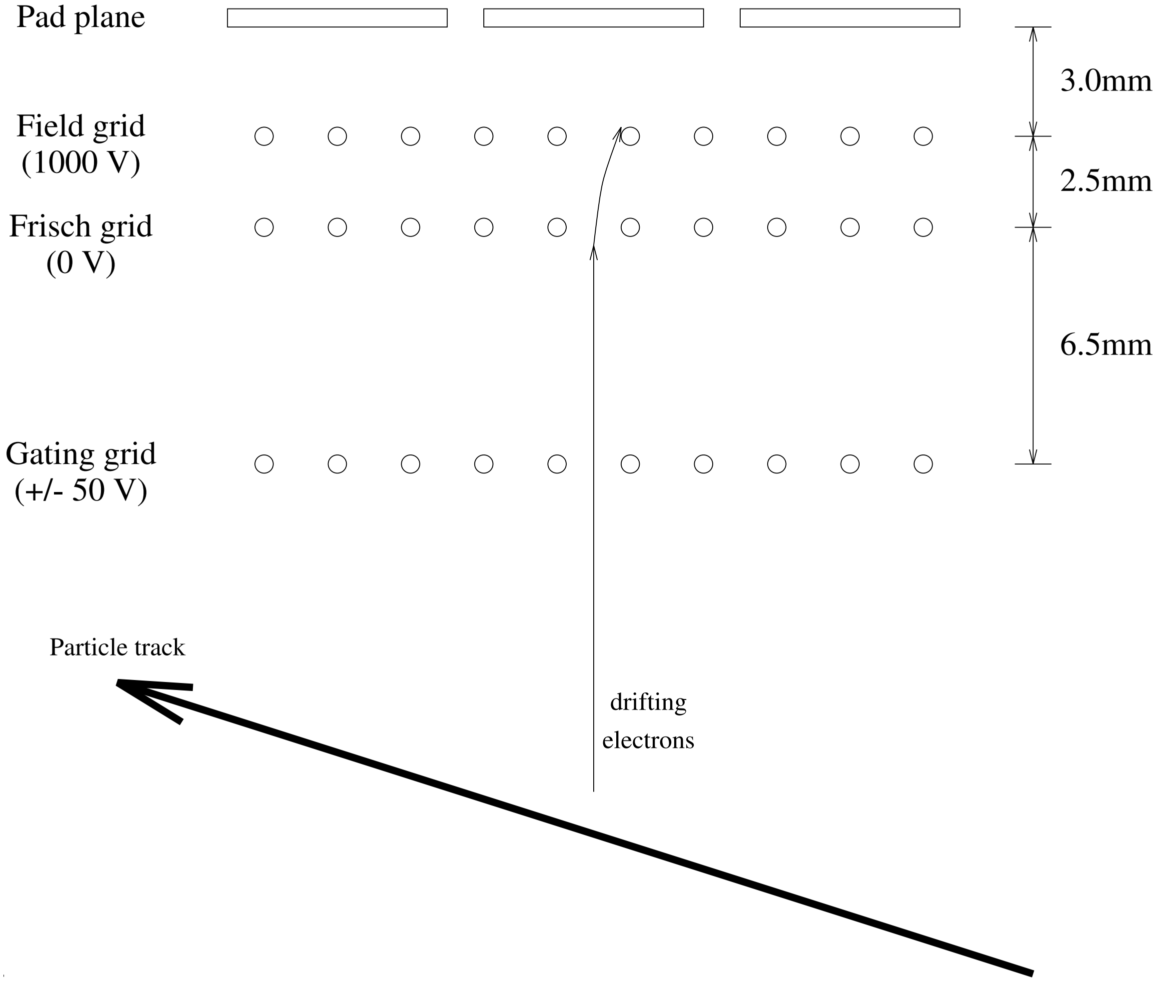

Figure 2.6: Schematic of the wire planes in the NA49 time projection chambers. Note that the spacing between the pad plane and the field grid is only 2 mm in the high-resolution sectors of the MTPCs.

2.5.2 TPC Gases

The TPC gas is chosen carefully. The drift velocity is affected by both the drift voltage and the gas density, but of more concern is the diffusion of electrons as they drift towards the pad plane. By adding molecular gases to the volume, the transverse velocity of the electrons can be reduced by absorption of the electrons' energy by the close-spaced spectra of rotational and vibrational modes in the molecular gases.

In most TPC designs, a mixture of argon and methane is used [Fern86]. In the main TPCs, the exact mixture chosen was 91% Ar/4.5% CH_4/4.5% CO_2, which provided adequate drift velocity and helped to reduce electron diffusion. In the vertex TPCs, where higher track densities cause problems, a more expensive 91% Ne/9% CO_2 mixture was used, which produced less diffusion and improved two-track resolution.

It should be pointed out that the ionization produced by a charged particle goes as Z^2, so the unfragmented beam passing through one of the TPCs would produce ~ 6700 times the ionization of a singly-charged particle and saturate the electronics. To prevent this, the vertex TPCs have the 20 cm wide central region of each TPC where the beam passes through isolated from the sensitive regions of the TPC, while for the main TPCs the beam passes through a gap between them.

2.5.3 TPC Electronics

Due to the large data requirements of this experiment (182,016 pads $\times$ 512 time buckets per pad $\times$ 1 byte per time bucket = 89 MB of data per event). To make matters worse, approximately 12 events per spill is expected, making the total beam spill data size slightly more than one gigabyte. Luckily, the SPS spill cycle provides beam for five seconds out of every twenty. The NA49 electronics stores the information during those five seconds and then writes it out during the remaining fifteen seconds. Also, data-compression is used before the events are stored in memory, which can successfully reduce event size by a factor of 10 [Rauc94].

Groups of 32 pads are connected to front-end (FE) cards, located directly above the pad plane. These cards amplify the signal from each pad, then run it through a shaping amplifier to convert it into a shape of defined width. These signals are

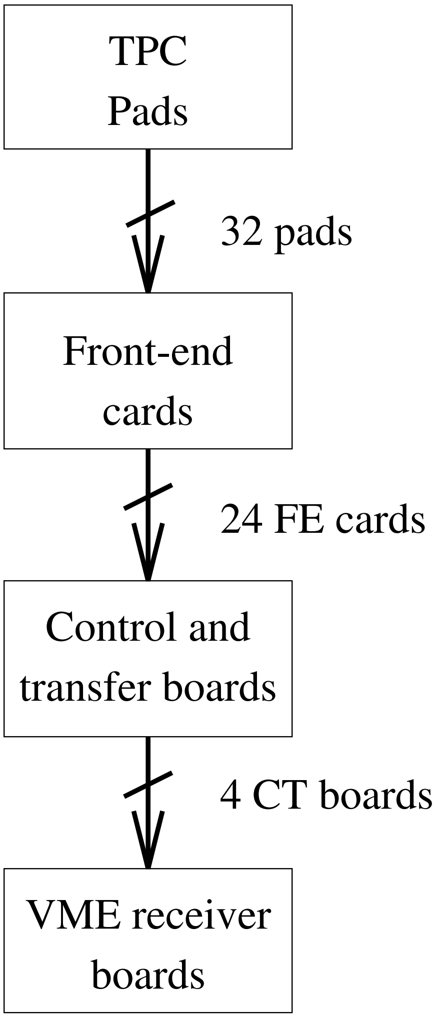

Figure 2.7: Electronics chain for the NA49 time-projection chambers.

then stored in a switched capacitor array, which stores 512 analog signals for each pad. This provides the time-dependence information that generates the y position of the track. Finally, this array is emptied through an ADC to the control and transfer (CT) board. Each CT board receives data from 24 FE cards, or 768 pads. This board collects data from the FE cards, provides signals and power to them, and sends the signals via a fiber-optic link to the receiver boards located in the counting house. Each receiver board collects data from 4 CT boards. The data from multiple events is zero-suppressed and stored in the 144 MB memory located on each board, then written out to tape during the time between beam spills [Beis96].

2.6 The Time-of-Flight Walls

At the time of the 1995 run, only two of the currently existing TOF walls were in place, TOF-R1 and TOF-L1. The time-of-flight measurements made possible by these detectors allows particle identification in the region where the proton and kaon dE/dx curves cross over and particle identification through dE/dx in the TPC is not possible. These detectors each consist of 891 simple scintillator cells read out by photomultiplier tubes. The timing is started by the T0 Čerenkov counter and ended by the signal from the photomultiplier. The resolution was calculated to be 75 picoseconds.

Later increases in funding allowed the addition of the "Grid-TOF" walls, TOF-R2 and TOF-L2. The design of these walls was more complicated than the original walls: 45 vertical scintillator slats and 48 vertical slats are read out by photomultiplier tubes, providing adequate coverage at a lower cost.

2.7 The Calorimeters

The NA49 experiment contains two calorimeters, known as the ring calorimeter and the veto calorimeter. Both have been used in many CERN experiments, starting with NA5. The veto calorimeter is used for selecting event centrality in all runs, and the ring calorimeter was used to measure transverse energy [Wein96, Huan97].

2.7.1 The Ring Calorimeter

The ring calorimeter consists of a 2.3 meter long cylinder with an outer radius of 149 cm and an inner radius of 28 cm [DeMa83]. It is subdivided in azimuth into 24 separate sectors and two active regions, a electromagnetic calorimeter in the front 20% and a hadronic calorimeter in the remaining portion. The electromagnetic portion is a lead-plastic sandwich configuration providing 16 radiation lengths and one interaction length of material. The hadronic portion provides 6 interaction lengths of material with an iron-plastic sandwich.

During the 1994 run, a target was placed behind the main TPCs to allow the calorimeter to cover the midrapidity region (the ring calorimeter cannot identify particle type, so in reality it must be described as covering the pseudorapidity region $2.1 < \eta < 3.4$). This allowed measurements of transverse energy with respect to azimuthal angle and pseudorapidity to be made, and provided evidence of second-order (or elliptical) transverse flow [Wein96, Huan97].

2.7.2 The Veto Calorimeter

The veto calorimeter consists of a rectangular lead-plastic calorimeter providing 17 radiation lengths and 9 interaction lengths of material for the projectile spectators that survive the collision. An iron collimator between the ring calorimeter and veto calorimeter accepts only these spectators, allowing an estimate of the event's impact parameter to be made.

Chapter 3

Particle Identification via dE/dx

3.1 Overview

Particle identification is critical to the NA49 experiment. Without it, there is no method of determining whether a particle is a proton from the initial projectile (or target) or a pion produced in the collision. Since many observables, such as temperature and transverse flow, have different values for different particle types, not having particle identification limits the possible physics results.

A primary advantage a time projection chamber has over multiwire proportional chambers is the ability to identify particle type from energy loss. As a charged particle travels through the gas-filled interior of a time projection chamber, it ionizes gas molecules, creating free electrons in the detector. The number of electrons released along the particle's path is directly related to the momentum and mass of the particle by a well-known relation, known as the Bethe-Bloch equation. If the momentum of the particle can be independently determined and the energy loss per distance traveled measured, the mass of the particle can be found.

3.2 The Bethe-Bloch Equation

In the 1930's, Hans Bethe and Felix Bloch took Bohr's 1915 semiclassical formula for the energy loss of a charged particle traveling through matter and applied quantum mechanical effects, resulting in what now is called the Bethe-Bloch equation. Enrico Fermi later developed an ultrarelativistic term, $\delta(\gamma)$, to correct for the dielectric screening effect caused by the relativistic concentration of the particle's electric field [Ferm40] at high values of $\beta\gamma$. The final energy loss equation is

$$\frac{dE}{dx} = D_e(\frac{Z}{\beta})^2 n_e \left(\ln \frac{2m_e c^2 \beta^2 \gamma^2}{I} - \beta^2 - \frac{\delta(\gamma)}{2} \right), \tag{3.1}$$

where

$$D_e = 4\pi r_e^2 m_e c^2,$$

m_e is the electron mass, $r_e = e^2/mc^2$ is the classical electron radius, Z is the charge of the particle, n_e is the electron density of the material the particle is traveling through, and I is an experimentally-derived parameter that represents the average excitation and/or ionization potential of the material. The mass dependence of the Bethe-Bloch equation becomes apparent when the relation

$$\beta\gamma = \frac{p}{mc}$$

is substituted into the log term.

At low values of $\beta\gamma$ ($\beta\gamma < 2$), the Bethe-Bloch equation is dominated by the $1/\beta^2$ dependence (see figure 3.1). In this region, different particles' dE/dx values are widely separated in ionization. Particle identification in this region has often been used in low-energy experiments [Rai90]. In the region from $\beta\gamma = 4 - 300$, the energy loss is dominated by the $\log \beta\gamma$ term, and the particle separation is smaller. This is the region used by NA49 particle identification. At large values of $\beta\gamma$ ($\beta\gamma > 300$), the δ term decreases the energy loss value for all particle types to a constant, and particle identification cannot be done by energy loss.

Most particles in the NA49 experiment fall in the central region where the particle identification is more difficult than at low $\beta\gamma$ but still possible, unlike the ultrarelativistic region. Making particle identification more difficult is the fact that the energy loss curves for different particles (i.e. protons and kaons) cross over at low momenta, making separation between those two particle types impossible in the time projection chambers – the TOF walls are included in the experiment to provide particle identification in this kinematic region.

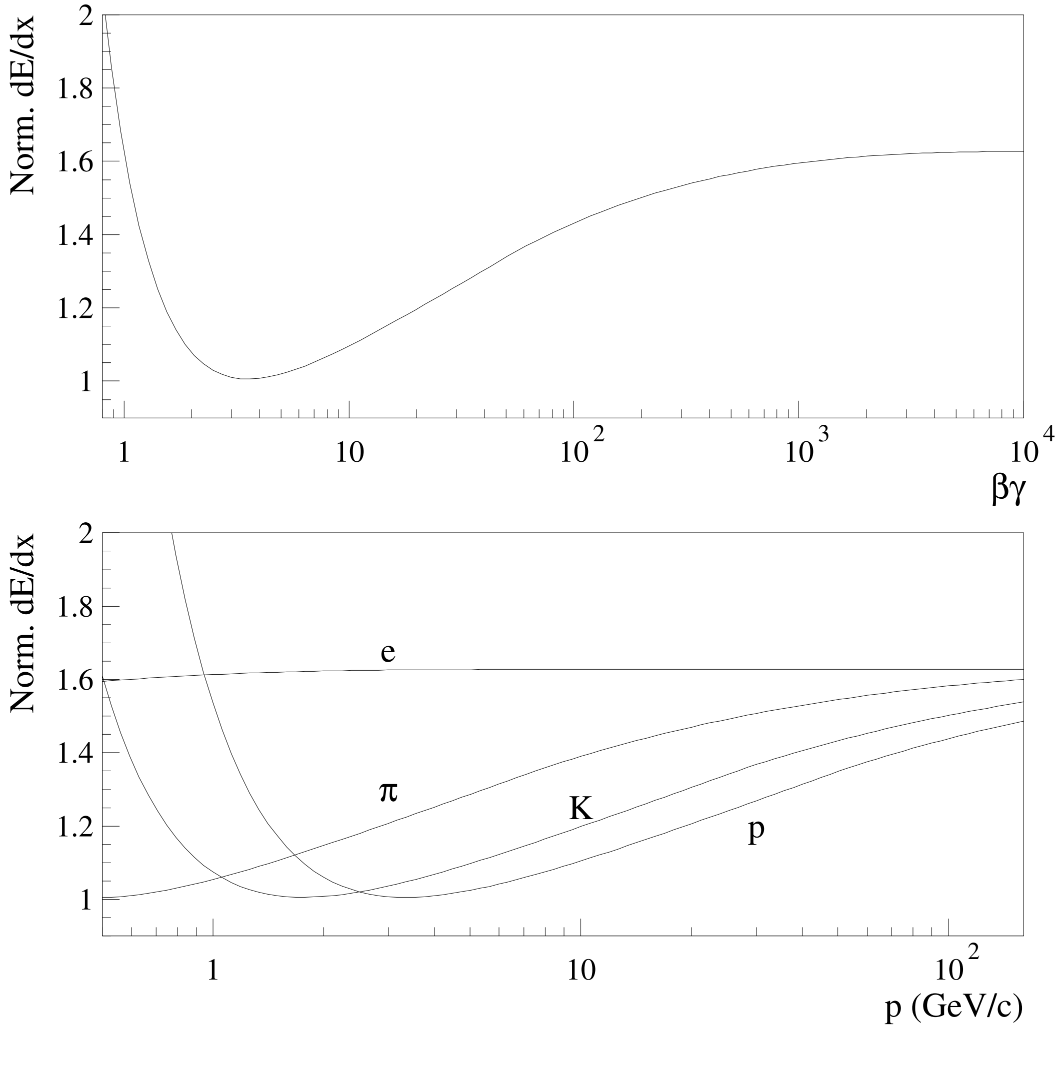

Figure 3.1: A typical Bethe-Bloch curve with respect to $\beta\gamma$ (top) and momentum (bottom). The vertical axis is dE/dx normalized to minimum ionization. The mass dependence is not seen when the Bethe-Bloch equation is plotted versus $\beta\gamma$.

3.3 Corrections For Detector Effects

Before any comparison can be made between the experimental results and the theoretical energy loss predictions, detector effects need to be determined and corrected for. The primary corrections include:

- pad crossing angle,
- electronics effects,
- gas gain,
- attenuation along the drift distance,
- sector-dependent effects, and
- time-dependent effects.

3.3.1 Pad Crossing Angle

Since a track may pass over a pad at any nearly any angle, across it or along vertically above it, the ionization measured by the pad needs to be corrected for the extra travel distance of the track. This can be accomplished, once tracking has been done, by

$$\frac{dE}{dx}_{corr} = \frac{dE}{dx}_{raw} \cdot \cos(\lambda) \cdot \cos(\theta),$$

where λ and θ are horizontal and vertical angles of the particle track crossing the pads as seen in figure 3.2.

In addition, the different pad sizes in the high resolution and standard resolution sections of the MTPCs require the dE/dx values to be scaled accordingly.

3.3.2 Electronics Corrections

The overall response of each pad can vary slightly due to variations in the electronics and pad size. To correct for this, a pulser calibration was run: the field wires were pulsed with a known wavefunction, producing a constant charge per unit area

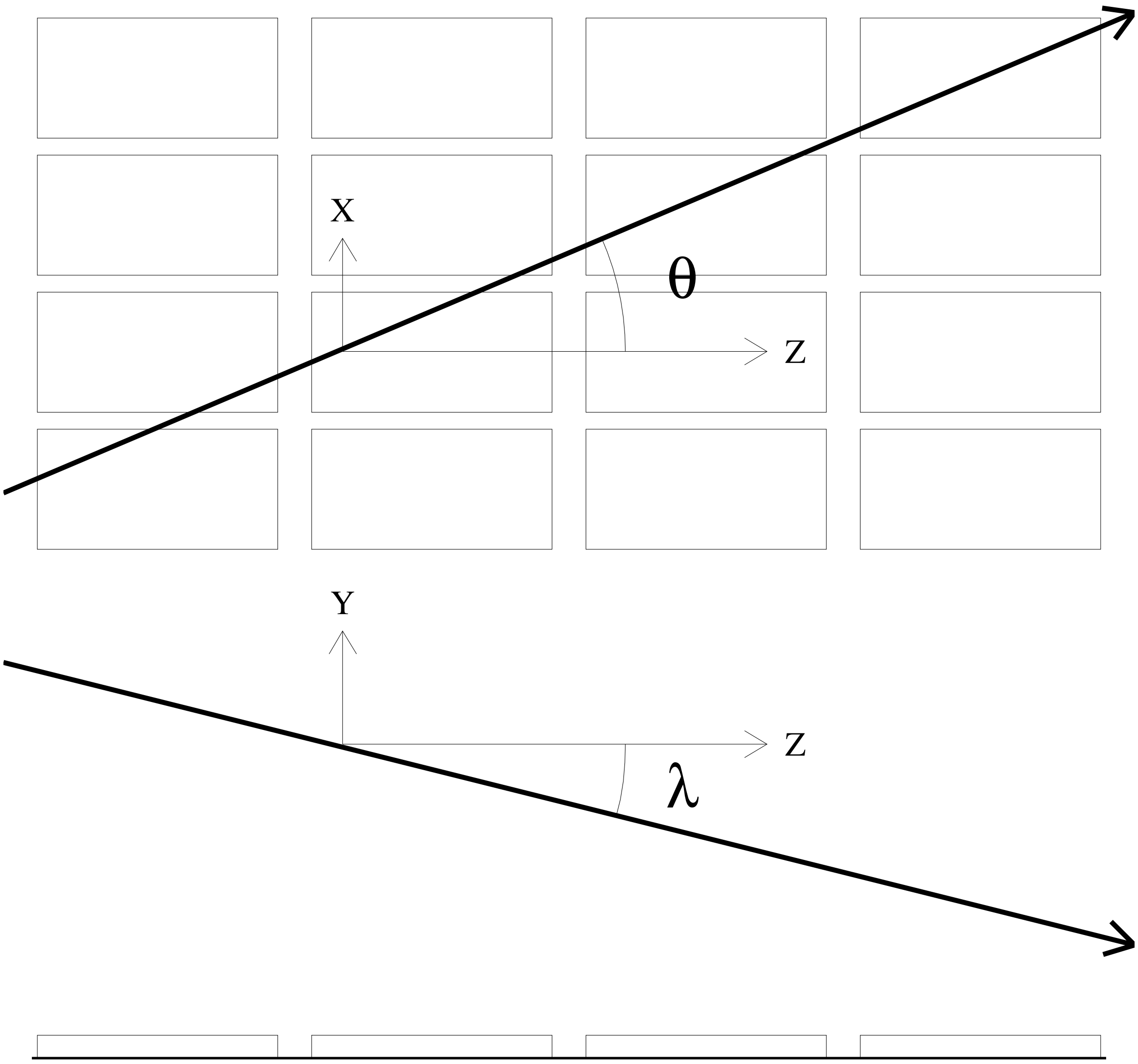

Figure 3.2: Pad crossing angles in a TPC. The top diagram is the top view, and the bottom diagram is the side view. The z axis is along the beam, the x axis is in the horizonal lab plane, and the y axis is vertical in the lab plane. Any raw dE/dx signals must be corrected for these crossing angles.

on each pad. These values were then read out and a correction factor determined for each pad to produce the same apparent average charge per unit area on each pad. Note that the pad size differences between the standard resolution sectors and the high resolution sectors in the MTPCs were also necessary to take into account.

3.3.3 Gas Gain

Fluctuations in the pad-by-pad response can also be affected by defects in the materials used to build the TPCs, effects due to a pad being on the edge of a sector (there is a small gap between sectors), and other geometric factors. To correct for these, immediately following each year's run a pad-by-pad calibration was obtained by releasing krypton gas into the TPCs. The excited state ^{83m}Kr, produced by decay of ^{83}Br, undergoes an isomeric decay, producing a gamma ray that knocks free a 41 keV electron from the same atom with a half life of $\tau = 1.83$ hours [Fire96]. These electrons were continuously collected on the pads. Since each pad received an equal flux of β particles and the decay charge spectrum for this isotope is well-known, an accurate calibration can be made on a pad-by-pad basis using this data.

The results of the krypton corrections [Ferg95] showed fluctuations in detector response from pad to pad, and corrections for this were applied. This correction brought the charge per cluster in the krypton runs to within 0.75% everywhere in the TPCs.

3.3.4 Drift Attenuation

There are several sources that absorb electrons as they are drifting towards the detection area of the TPC: a small fraction of them recombine with the gas ions, reforming neutral gas atoms; electons can be absorbed at the walls of the TPC; and contaminants in the detector gas such as oxygen aggressively absorb electrons.

By looking at a superset of many events, the variation in measured energy loss with respect to drift distance can be measured. A plot of mean charge against y-position in the TPC shows a simple linear dependence on drift distance that can be corrected for. Figure 3.3 shows this plot for the 1994 data [Dunn97].

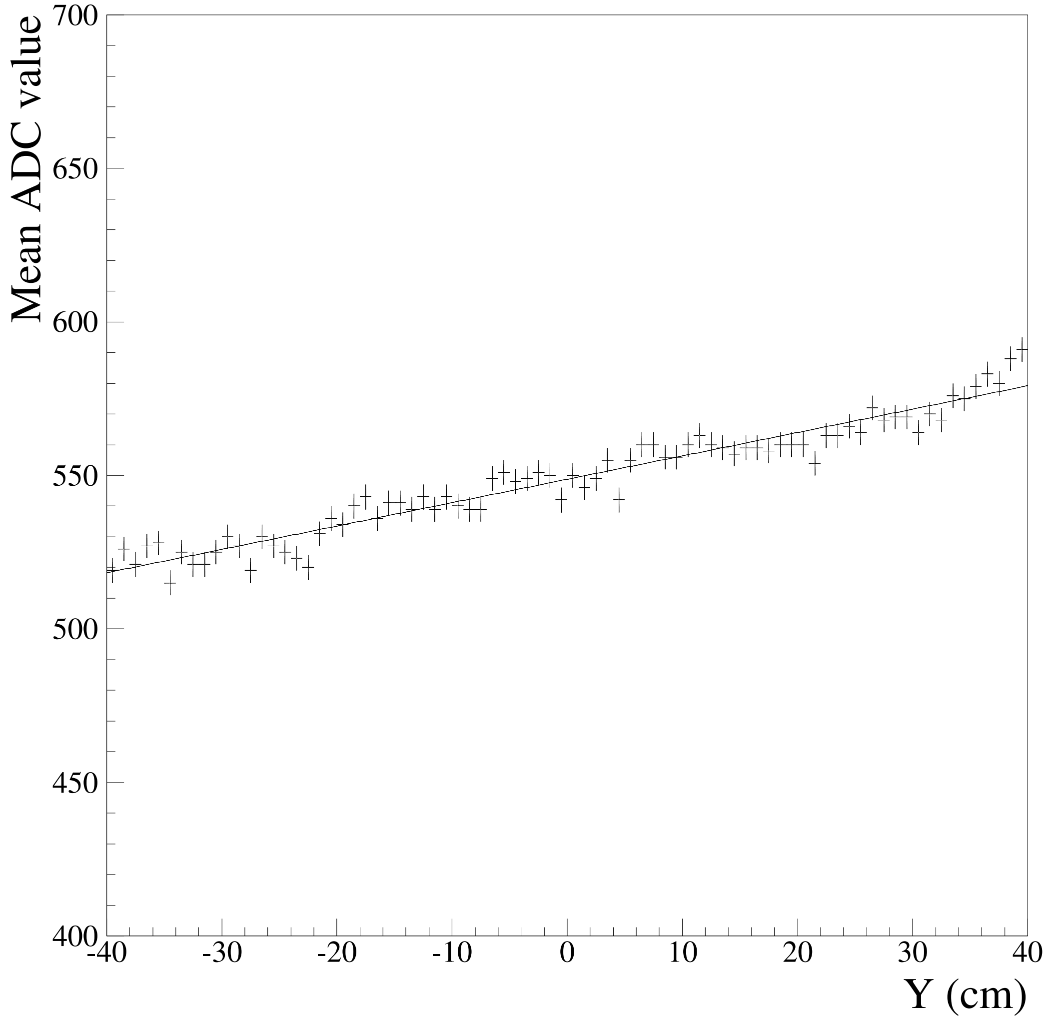

Figure 3.3: Drift attenuation effect for MTPCR, 1994 run. The linear dependence of the mean ADC value with respect to vertical position in the TPC is clearly seen [Dunn97].

3.3.5 Sector Corrections

The time projection chambers in NA49 were divided into sectors of pads and electronics, with 25 (5×5) in the MTPCs and 6 (3×2) in the VTPCs (see figure 2.4). Since each sector was a separately machined pad plane and the electronics were common within a sector, variations in ionization could occur between sectors. By measuring total ionization within each sector over many events, the differences in sector response could be identified. These could then be corrected to yield the same average total ionization in all sectors, by

$$\frac{dE}{dx}_{corr} = \frac{dE}{dx}_{raw} \cdot C_i,$$

where $i = 1, 2, ..., 25$ is the sector number. Figure 3.4 shows the sector corrections for the 1994 data.

3.3.6 Time-Dependent Corrections

Since a TPC is a gas-filled detector, changes in the environment such as temperature and air pressure affect the detector response. In addition, any fluctuations in gas quality or mixture can have a marked effect. These effects are more gradual, only appearing when different data sets are compared. To correct for these effects, the data must simply be renormalized to a chosen value of mean dE/dx. Table 3.1 shows renormalization values for the 1995 medium-bias data, which were calculated using the found dE/dx values for pions with $p = 5.0 - 5.5$ GeV/c and $p_T = 0.0 - 0.2$ GeV/c. Examining these values also shows a difference in dE/dx between the right and left MTPCs of about 1%, which is also corrected for. These data sets were all taken within a 24-hour period; figure 3.5 shows the values plotted against time.

3.4 Track dE/dx Calculation

Once the dE/dx values of the found clusters have been corrected, the clusters on each track are collected and analyzed to find the mean dE/dx value for a each track. The values of these measurements for a given track fluctuate a great deal since what

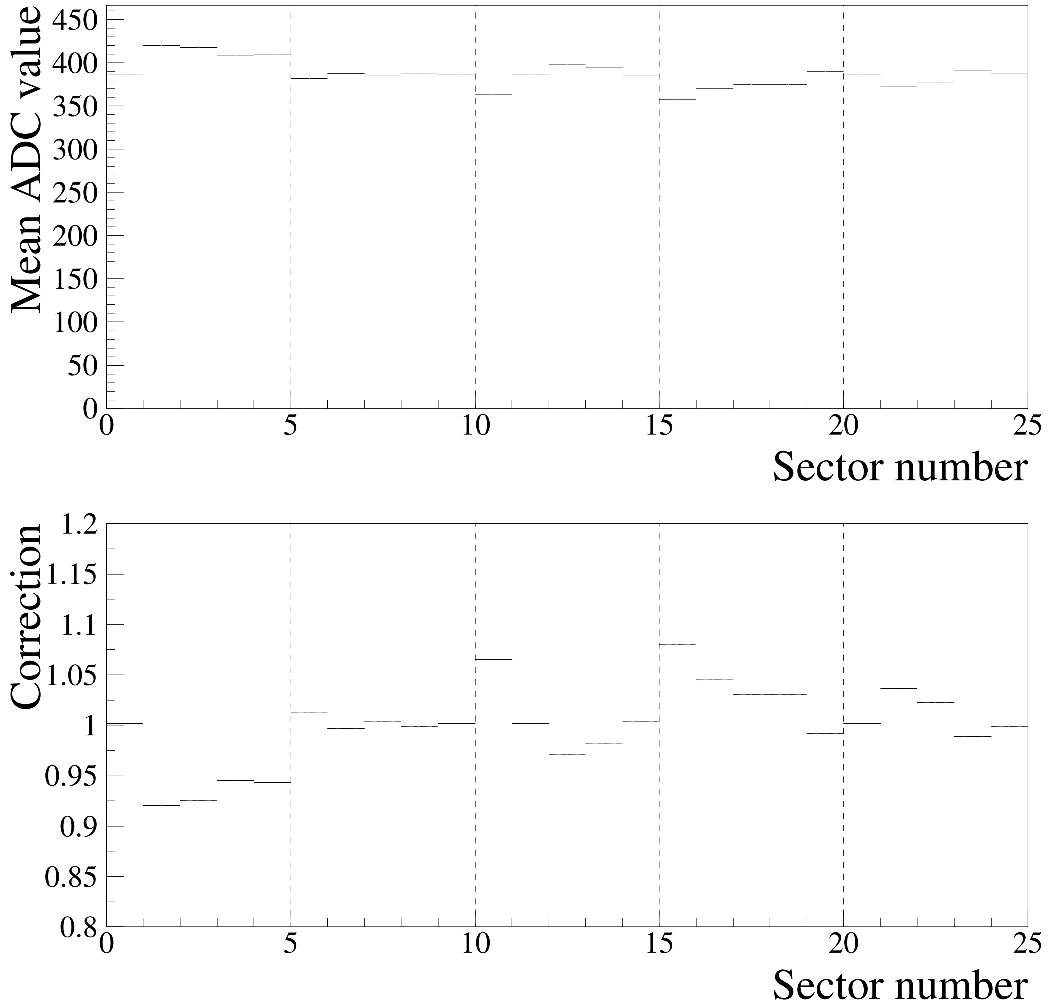

Figure 3.4: Sector corrections for MTPCR, 1994 run. The actual configuration is a 5×5 array of sectors (see figure 2.4) – the dotted lines in the figure above separate each continuous row of numbering. Sectors 1-5 are the row nearest the beampipe for MTPCR (sectors 21-25 are nearest for MTPCL). The top plot shows the actual mean ADC values for each sector (arbitrary units), while the bottom plot shows the correction factors applied to produce the same mean correction value in each sector [Dunn97].

Data Set	Correction	Data Set	Correction
853	0.9825	859	1.0061
854	0.9860	860	1.0110
855	0.9897	862	1.0121
858	1.0048	863	1.0113

Table 3.1: Overall correction values for 1995 medium-bias data sets.

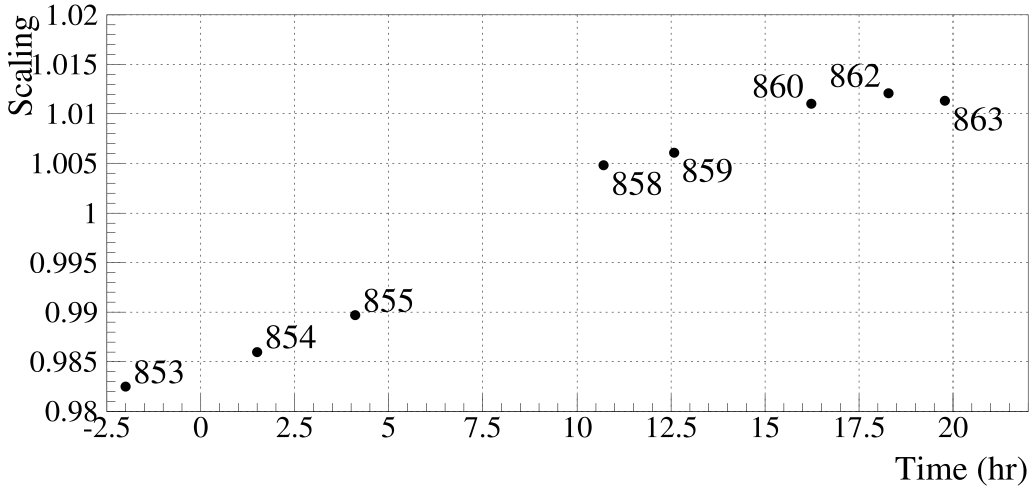

Figure 3.5: dE/dx correction factors over time for medium-bias sets. A general trend is clearly seen. Sets 856 and 857 were laser calibration runs, and set 861 failed immediately after it was started.

is actually being measured is not precisely the energy lost by the particle, but rather the energy loss inferred from collecting the electrons freed from the gas atoms.

Several possible types of collisions between the particle and atomic electrons are possible. Excitation collisions will excite the electrons, but not free them from the gas atom. The energy that goes into these collisions is not detected. "Soft" collisions are those that free electrons, and "hard" ones are where the electron gains a significant fraction of the particle's momentum, turning it into a δ electron that can ionize the gas itself and create its' own track in the detector.

The distribution of these dE/dx values deviates from a Gaussian because of the high-energy collisions, creating a "Landau tail" at higher dE/dx values. To quickly and easily find the most probable dE/dx value for a given track, cutoff values are typically used. This entails removing some top fraction of the total number of clusters, effectively cutting off the Landau tail. Similar cutoffs can be made for the lower edge as well, and were in the NA49 analysis. In this analysis, the lower 10% and the upper 35% of hits were removed from the mean dE/dx value calculation.

3.5 The JADE dE/dx Parameterization

Experimental dE/dx values will differ from the Bethe-Bloch equation for several reasons, including different scaling of the actual dE/dx value, uncertainties and statistical errors in the measurements, and the dependences of the $\delta(\gamma)$ term on the gas composition. For these reasons, it is preferable to fit the data with a parameterization of the Bethe-Bloch equation rather than the equation itself. The equation used in the NA49 dE/dx analysis was the same one used by the JADE collaboration at DESY in 1979-84. This method was also used by the NA35 collaboration, the precursor to NA49 [Gunt94]. The density correction $\delta(\gamma)$ parameterization was taken from work by Sternheimer and Peierls [Ster71].

To fit to this parameterization, plots of dE/dx against momentum are needed for separate particle types. The following section will examine the methods used for this first step. Once those values are found, the parameterization can be fit to them and compared to the theoretical Bethe-Bloch curve.

3.5.1 Fitting the Data

The dE/dx data for 3300 events in the 1995 medium-bias data can be seen in figures 3.6 and 3.7 – the NA49 spectrometer magnet setup places negative particles and positive particles in separate detectors[1]. The dE/dx units (ADC) represent arbitrary analog-to-digital converter counts and are directly proportional to the charge measured. The rigidity of the tracks is measured by tracing them back through the magnetic field. Since fragment production is rare at these enegies the charge of each particle is assumed to be ± 1, this values is assumed to be the momentum. At the low-momentum end, the peaks for electons/positrons ($ADC \simeq 525$) and pions ($ADC \simeq 400$) can be clearly seen. The rise just below the pion peak contains kaons in the negative data, and kaons plus protons in the positive data. The kaon and proton peaks are obviously not clearly separable from one another, and in most cases their gaussians are not fully separable from the pion gaussian either.

It can also be seen from these figures that at lower momenta pion production dominates the total yield. This drops off at high momenta, where protons should be the dominant particle type. Electron production is strongest at very low momenta, but dies off quickly as the momentum increases.

This data can be divided into $\log(p)$ slices, as seen in figure 3.8. The slices are made in $\log(p)$ instead of p because the Bethe-Bloch equation goes as $\log(p)$ in NA49's region of interest. In this slice, the proton/kaon peak region is clearly visible, and when compared to the negative particles in figure 3.9, the absence of protons (and the low production rate of antiprotons) is clear.

Once these plots have been made, they can be fit with gaussians to accurately find the means for each particle type. To do this, a ten-parameter fit of the sum of four gaussians is used:

$$\begin{aligned} f(x) &= h_p \exp(-(x-\mu_p)^2/(2\mu_p w_h)) \\ &\quad + h_\pi \exp(-(x-\mu_\pi)^2/(2\mu_\pi w_h)) \end{aligned}$$

[1] A few extreme backward-rapidity particles are emitted such that the magnets sweep them into the "incorrect" MTPC for their charge, but they can be easily identified by their distinct track angles.

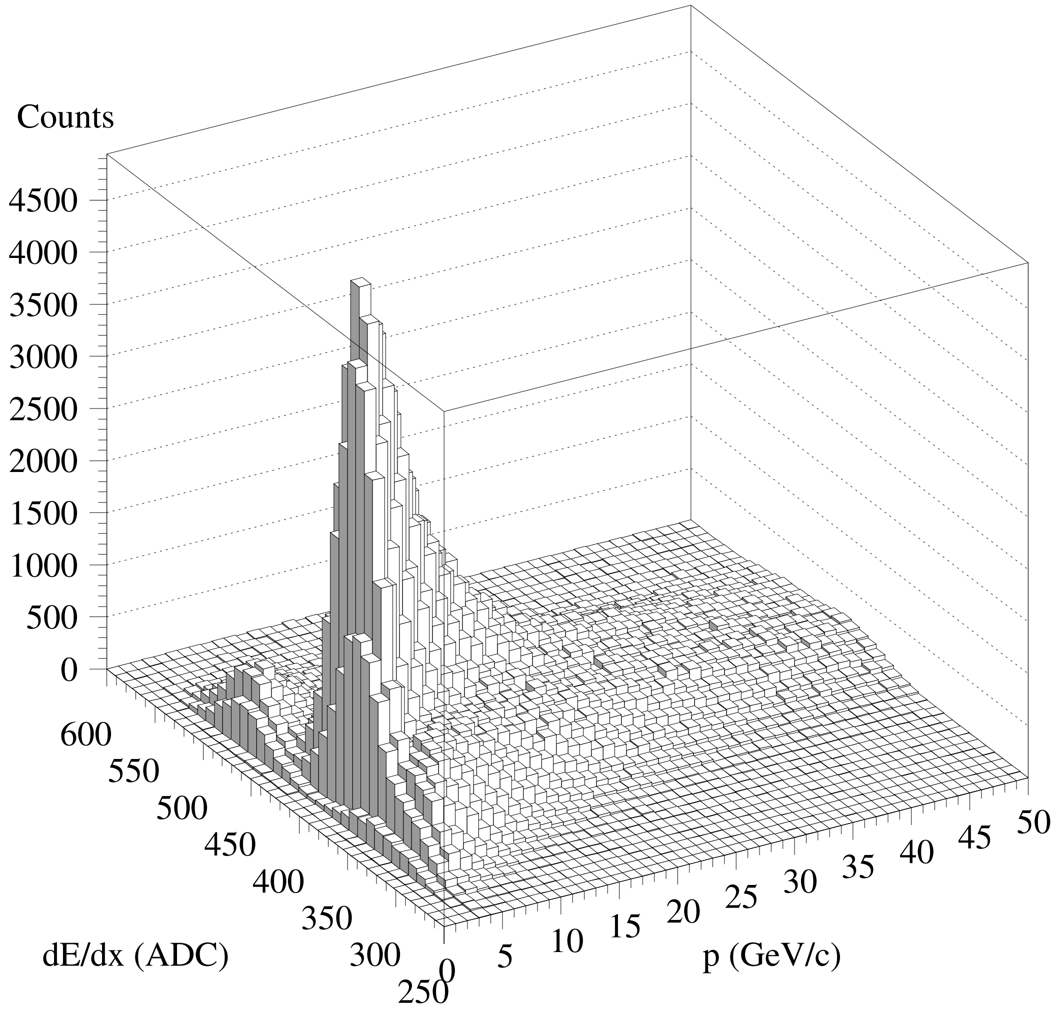

Figure 3.6: Total dE/dx data for 3300 events from the medium-bias 1995 data. This figure contains only positive particles. The peak at highest dE/dx is the positrons, the large peak is the pions, and the kaons and protons form the shoulder on the low side of the pion peak.

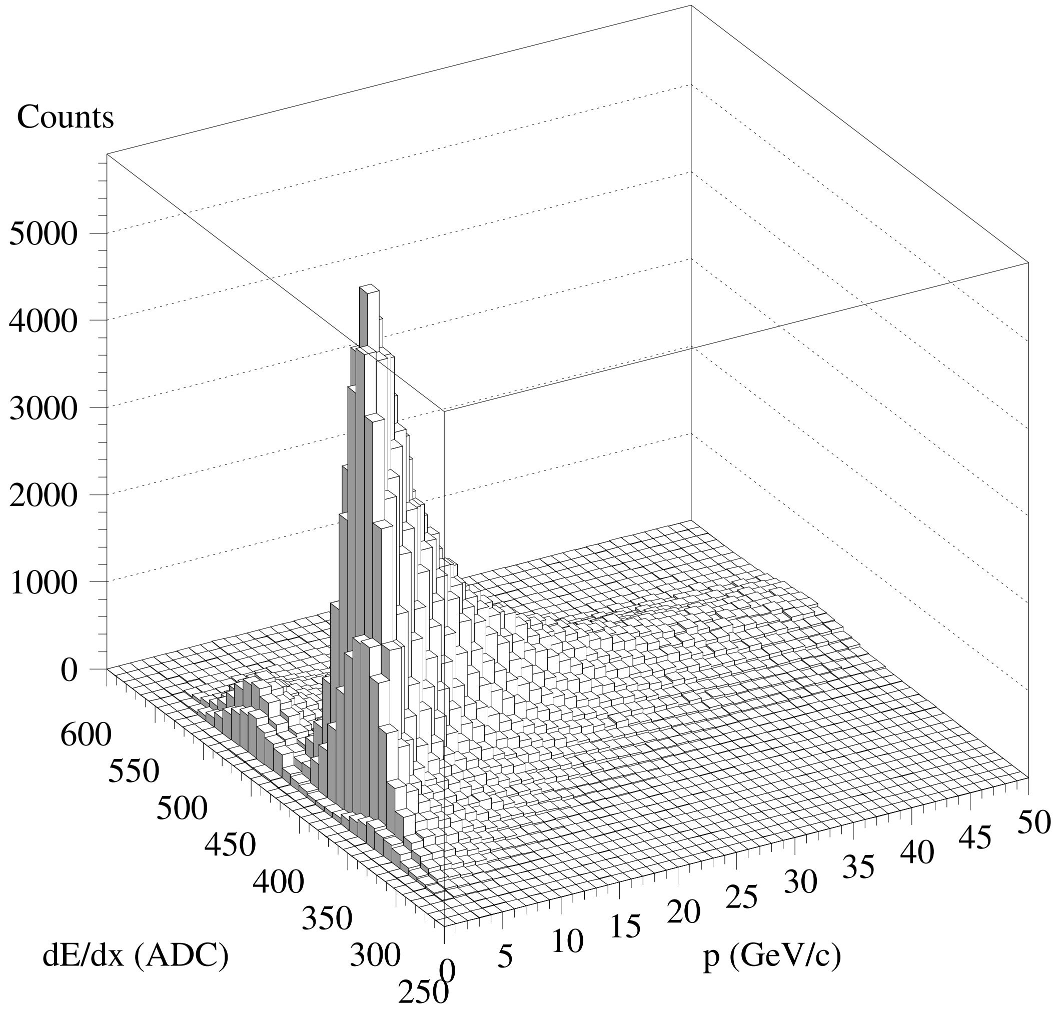

Figure 3.7: Total dE/dx data for 3300 events from the medium-bias 1995 data. This figure contains only negative particles. The peak at highest dE/dx is the electrons, the large peak is the pions, and the kaons and antiprotons form the shoulder on the low side of the pion peak.

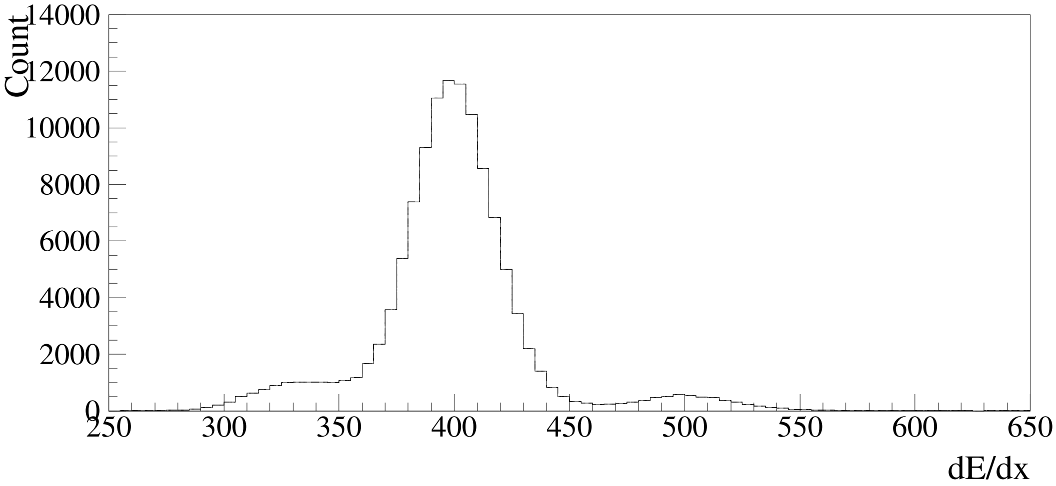

Figure 3.8: dE/dx for particles with $p = 5.0 - 5.5$ GeV/c and $p_T < 0.2$ GeV/c from the 1995 medium-bias data. This figure contains only positive particles from the right MTPC.

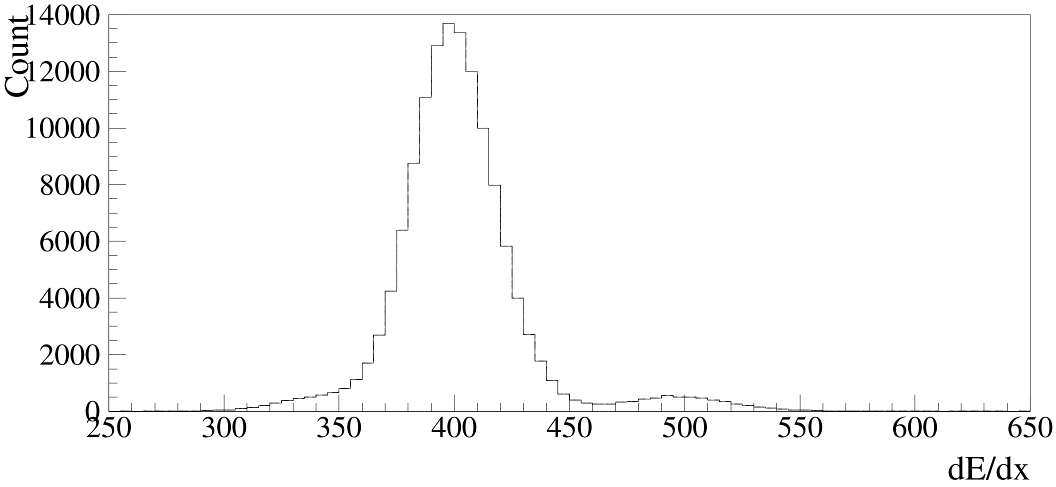

Figure 3.9: dE/dx for particles with $p = 5.0 - 5.5$ GeV/c and $p_T < 0.2$ GeV/c from the 1995 medium-bias data. This figure contains only negative particles from the left MTPC.

Parameter	Value
h_e, μ_e	Height and mean of electron/positron gaussian.
h_π, μ_π	Height and mean of pion gaussian.
h_K, μ_K	Height and mean of kaon gaussian.
h_p, μ_p	Height and mean of proton/antiproton gaussian.
w_h	Percentage width of all hadrons (σ/μ).
w_e	Percentage width for $e^\pm$.

Table 3.2: Parameters for gaussian fit of data.

$$+ h_K \exp(-(x-\mu_K)^2/(2\mu_K w_h))$$
$$+ h_e \exp(-(x-\mu_e)^2/(2\mu_e w_e))$$

The parameters of the fit consist of a mean and height for each particle type, a common percentage width for all hadrons, and a percentage width for the electrons/positrons. The percentage widths represent the detector resolution of the dE/dx values (see table 3.2). Example fits are shown in figures 3.10 and 3.11.

The values of σ for the electron gaussians were consistently wider than the other particles. At NA49 energies, all singly-charged particles lose energy through collisions at approximately the same rate, but since the masses of electrons and positrons are so small, their path through matter is much more irregular than the paths of heavier particles, thus producing a greater range of dE/dx values and a greater value of σ [Fern86].

The lack of antiprotons in the negative particle plots allows this fit method to be simplified (provided you are not looking for antiprotons). By assuming that there are *no* antiprotons, then the variables for the proton mean and height can be ignored, turning the nine-parameter fit into a seven-parameter fit. Also, as can be seen in figure 3.10, the proton and kaon gaussians overlap one another to a great degree. This will cause the fit of these two gaussians to be very dependent on one another. In the case of the negatives, the kaon fit is more robust since there is no dependence on the fit of the protons.

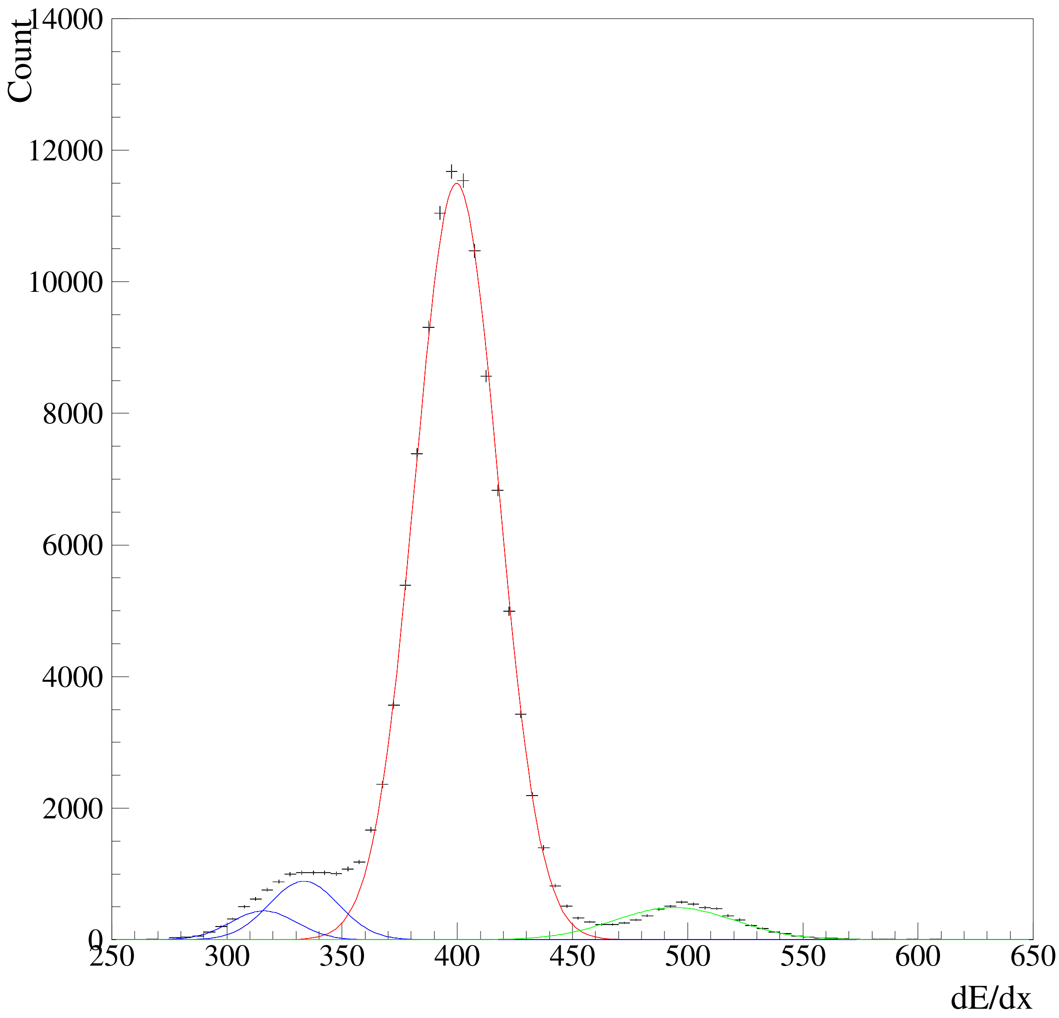

Figure 3.10: Gaussian fits of dE/dx for particles with $p = 5.0 - 5.5$ GeV/c and $p_T < 0.2$ GeV/c from the 1995 medium-bias data. This figure contains only positive particles from the right MTPC. The axis along the right is momentum in GeV/c, the axis along the left is dE/dx in ADC counts, and the vertical axis is particle count.

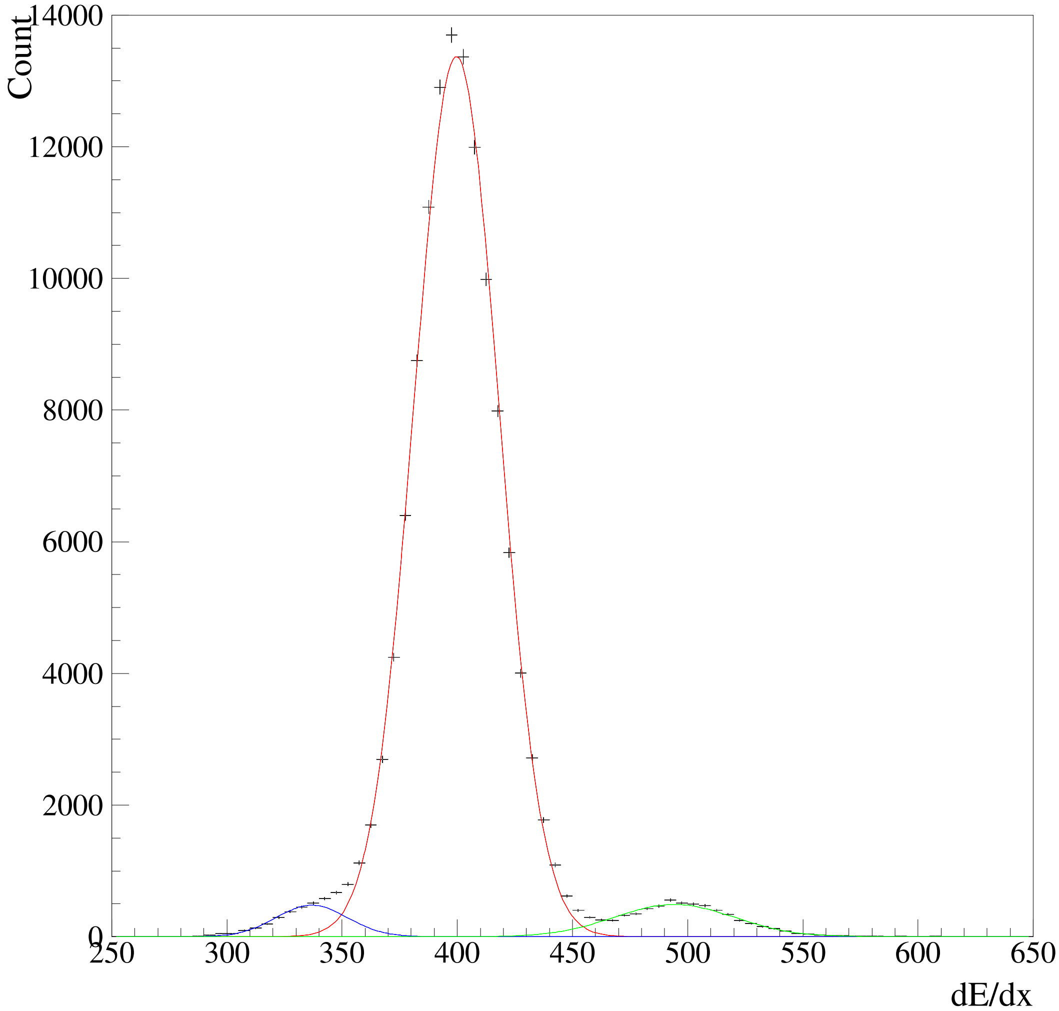

Figure 3.11: Gaussian fits of dE/dx for particles with $p = 5.0 - 5.5$ GeV/c and $p_T < 0.2$ GeV/c from the 1995 medium-bias data. This figure contains only negative particles from the left MTPC. The axis along the right is momentum in GeV/c, the axis along the left is dE/dx in ADC counts, and the vertical axis is particle count.

3.5.2 The Parameterization

The parameterization of the energy loss, ϵ, has the form

$$\epsilon = \zeta \cdot \frac{Q^2}{\beta^2} \cdot \left(K + \ln \beta^2 + \ln \gamma^2 - \beta^2 - \delta(\beta)\right),$$

where ζ, K, and $\delta(\beta)$ are free parameters, and Q is the particle's charge. K determines the minimum of the function, and ζ is a factor that describes the target density and acts as a scaling factor. The function $\delta(\beta)$ is more complicated, and has the form

$$\delta = \begin{cases} 0 & \text{for } X < X_0 \\ 2\ln 10 \cdot (X - X_A) + a \cdot (X_1 - X)^m & X_0 < X \leq X_1 \\ 2\ln 10 \cdot (X - X_A) & X_1 < X \end{cases}$$

where $X = \log \beta\gamma$, and X_0 and X_1 are parameters that determine the region affected by $\delta(\beta)$. They are defined by

$$X_1 - X_0 = \left(\frac{2\ln 10}{ma}\right)^{\frac{1}{m-1}}$$

and

$$X_0 = X_A - a \cdot \left(\frac{X_1 - X_0}{2\ln 10}\right)^m .$$

For our detector setup, m should have the value $m = 3$ [Ster71]. Also, from the NA35 report [Gunt94] on their use of this parameterization X_0 should be 1.7711 and X_1 should be 4.2009. The free parameters in this part of the parameterization are X_A and a: X_A represents the height of the Fermi plateau, and a controls the shape of the curve.

3.5.3 Fitting to the Parameterization

To properly fit the data with this parameterization, one needs to plot the mean dE/dx values of all particles (as determined from the gaussian fits) vs. $\beta\gamma$. Since the NA49 MTPCs cover a fixed region in momentum, the corresponding values of $\beta\gamma$ for the different particles detected cover different regions of the parameterization.

Parameter	Value
ζ	24.108
K	10.104
X_A	2.4935
a	0.23265

Table 3.3: dE/dx parameterization fit values from 1994 central events [Dunn97].

This provides a much better parameterization fit than if each particle type were fit separately. Specifically, the electrons fall on the Fermi plateau, while the pions fall in the relativistic rise region and the protons and kaons near the minimum ionization regon. Particles with momentum below 3 GeV fall outside the main TPCs, so no data is available to be fit below minimum ionization.

This parameterization was performed for 1994 and 1995 central Pb+Pb data by Jason Dunn and myself. The parameter values from this fit are in table 3.3, and a plot of the parameterization with the data is shown in figure 3.12. The range of of momentum ($3 - 15$ GeV for kaons, and $3 - 22$ GeV for pions) was limited to ensure particles were correctly identified.

Closer inspection of the pions in figure 3.12 show a significant deviation from the parameterization, as well as a separation from the trend in other particle types. This was investigated and found to be due to gain fluctuations in the different pad plane regions of the TPC: a change in gain between the high-resolution sectors and standard-resolution sectors caused the dE/dx of each particle type to vary with momentum. This caused the trend for each particle type to leave the parameterization curve at a different value of $\beta\gamma = p/m$, making successful fitting difficult. It was believed that the krypton and sector corrections would have corrected for this effect, but they did not fully remove the effect in the 1995 data. Since this deviation is caused by the physical layout of the detector, the same problem exists in the 1995 medium-bias data.

A further complication is the dE/dx resolution of the detectors. As mentioned above, a limited range of momentum was used to ensure clear particle identification.

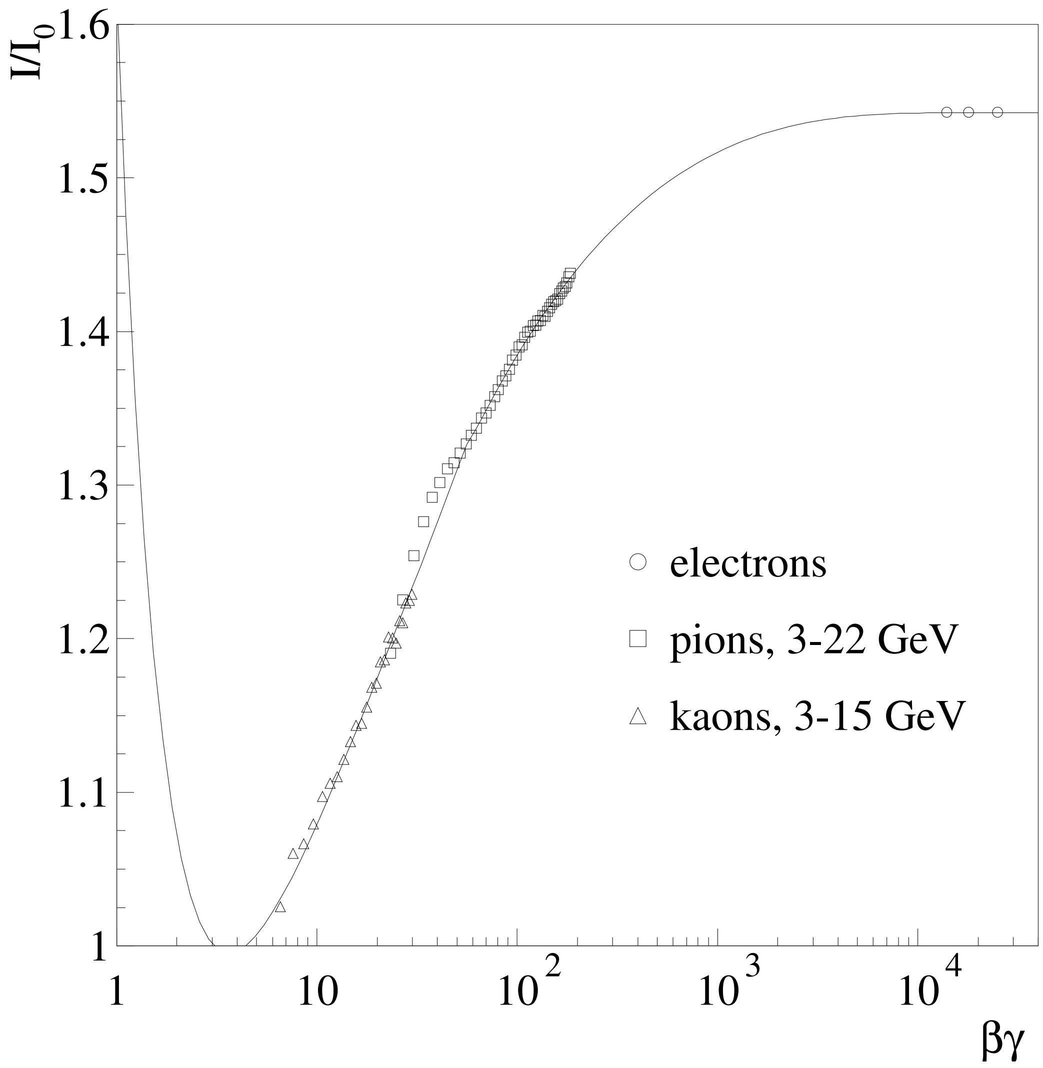

Figure 3.12: Parameterization fit for 1994 central collision data [Dunn97]. This plot is negative particles only. The vertical scale is dE/dx rescaled so that minimum ionization is approximately 1. Note the deviation of particles from the parameterization.

These limits were caused by the limited resolution of the main TPCs.

dE/dx resolution is defined as the w_h parameter from table 3.2. The predicted resolution limit was 4.5%, calculated using the standard Allison and Cobb formula [Alli80]. Typical fluctuations of actual detectors from calculated values are on the order of $\pm 0.5\%$. The actual resolutions, plotted versus momentum, can be seen in figure 3.13. At the lowest momentum values, the resolution is around 4.9%, but it rises to 5.6% at 20 GeV/c. This increase in resolution makes the fitting of gaussians to the distribution (as described in section 3.5.1) difficult as the gaussians get closer together with increasing momentum, where the width increases.

This increase in the width of dE/dx gaussians is most likely due to merging of charge clusters on tracks in the high-resolution sectors. The charged-particle density increases with momentum as the track gets closer to the beamline, and the NA49 cluster-finding and tracking program is unable to effectively separate charge clusters on nearby tracks. When clusters that appear to be merged are found, the program attempts to separate them by finding a dip in charge in either the space or time direction and simply dividing it there. This is not an ideal method, and is the most likely reason for the increase in dE/dx widths, but it is quite fast in comparison to more detailed cluster-fitting methods. These methods are currently being investigated for use in NA49 and other experiments, but currently they add substantially to the processing time for each event.

More recent analysis of NA49 central data has included global track matching, where tracks have been successfully matched between the main TPCs and the vertex TPCs [Lasi97]. This provides two independent dE/dx measurements, which brings the overall dE/dx resolution of the NA49 experiment near the predicted value of 4.5%. This is done by plotting the dE/dx from the main TPCs versus the dE/dx from the vertex TPCs (see figure 3.14). This has the effect of increasing the distance between the center of each particle type's gaussian (now a two-dimensional function), which enhances particle separation. Unfortunately, this track matching was not done for the 1995 medium-bias data.

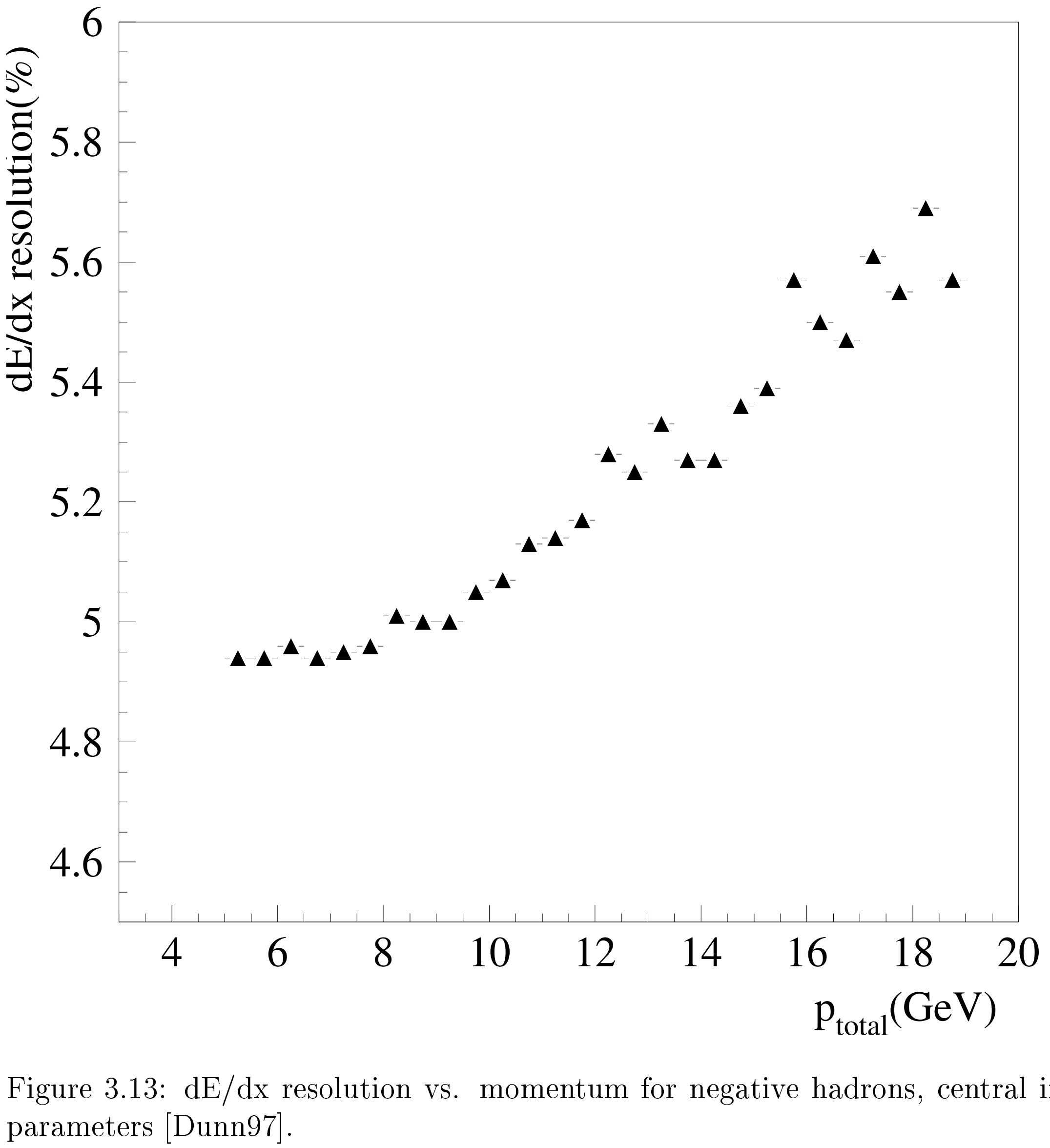

Figure 3.13: dE/dx resolution vs. momentum for negative hadrons, central impact parameters [Dunn97].

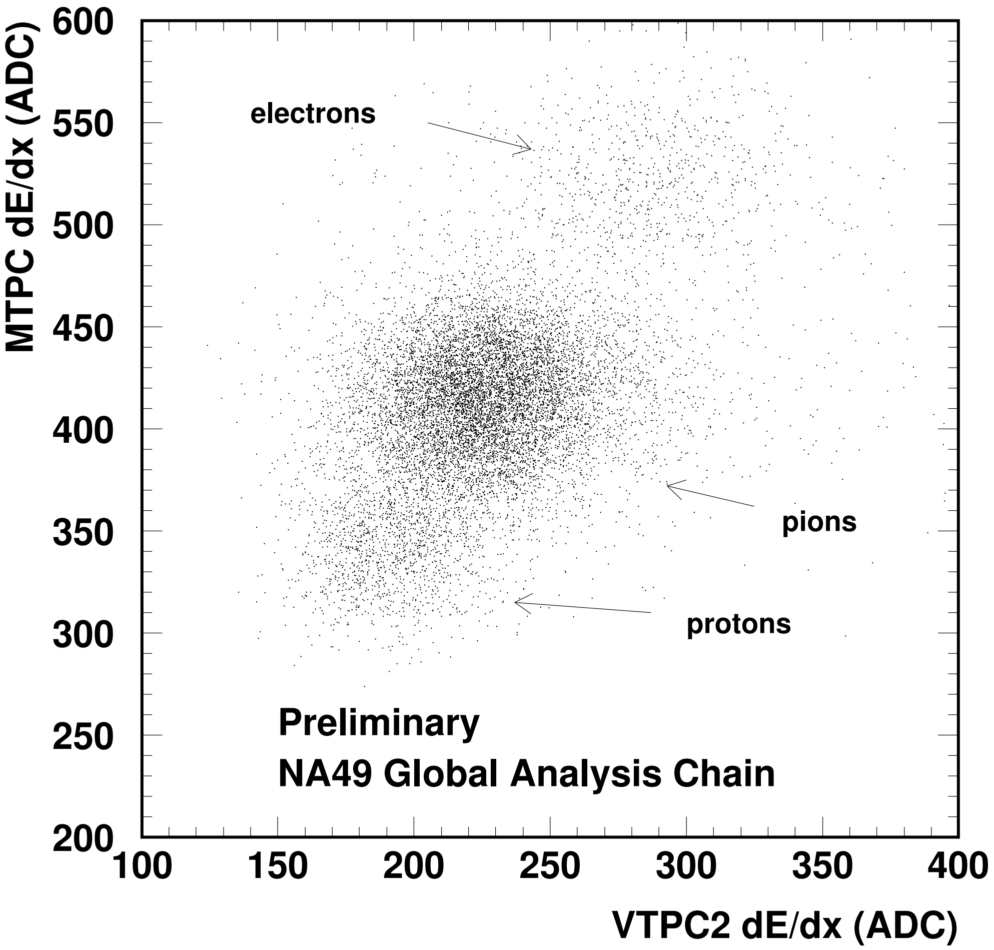

Figure 3.14: dE/dx in MTPCs vs. dE/dx in VTPC2 [Lasi97]. Global tracking of particles between TPCs allows two independent measurements of dE/dx, providing greater separation between proton and pions.

3.6 +/- Comparison Method of PID

These limitations in the NA49 dE/dx capabilities made using the JADE parameterization undesireable for the transverse flow analysis. A solution to this problem was found by giving up the requirements of successfully identifying kaons. By accepting this loss, it would be possible to create cuts to cleanly separate protons from pions, although some kaon contamination may be present in both selections. To visualize these cuts, look at figure 3.10 and imagine cuts that removed the central part of the kaon gaussian. These cuts would also remove a few pions and a larger number of protons, but the particles below the lower cut would be mostly protons, and above the upper cut the particles would be mostly pions. More importantly, there would be very few protons misidentified as pions or vice-versa.

Unfortunately, where this cut should go is not clear at higher rapidities. At low momenta, such as the $p = 5.0-5.5$ GeV/c region shown in figure 3.10, the individiual particle gaussians are fairly cleanly separated. The separation between these gaussians shrinks as the particles' momentum increases, as can be seen from figure 3.1. In addition, the widths of the gaussians increase with the mean dE/dx value.

To find a reasonable cut location, comparisons were made of dE/dx curves for various momenta in the left and right TPCs, i.e. comparing dE/dx for positive particles to dE/dx for negative particles. An example of this can be seen in figure 3.15a. Note the protons, visible as a positive bump at low dE/dx, and the excess of negative pions over positive pions, seen as the negative dip at mid-dE/dx values.

Next, this difference between TPCs is divided by the original distribution for the positive particles, producing a plot that has the value +1 for a region of dE/dx where all particles come from the MTPC containing positive particles, and -1 for regions where all particles come from the negative MTPC. An example of this can be seen in figure 3.15b.

A line is then drawn at $(N_{pos} - N_{neg})/N_{pos} = 0.5$, where the positive particle production is twice that of the negative particle production. The dE/dx value that corresponds to the proton/kaon interface (the downward curve of the proton bump in figure 3.15a) is then recorded as a cut value. This is demonstrated in figure 3.15b.

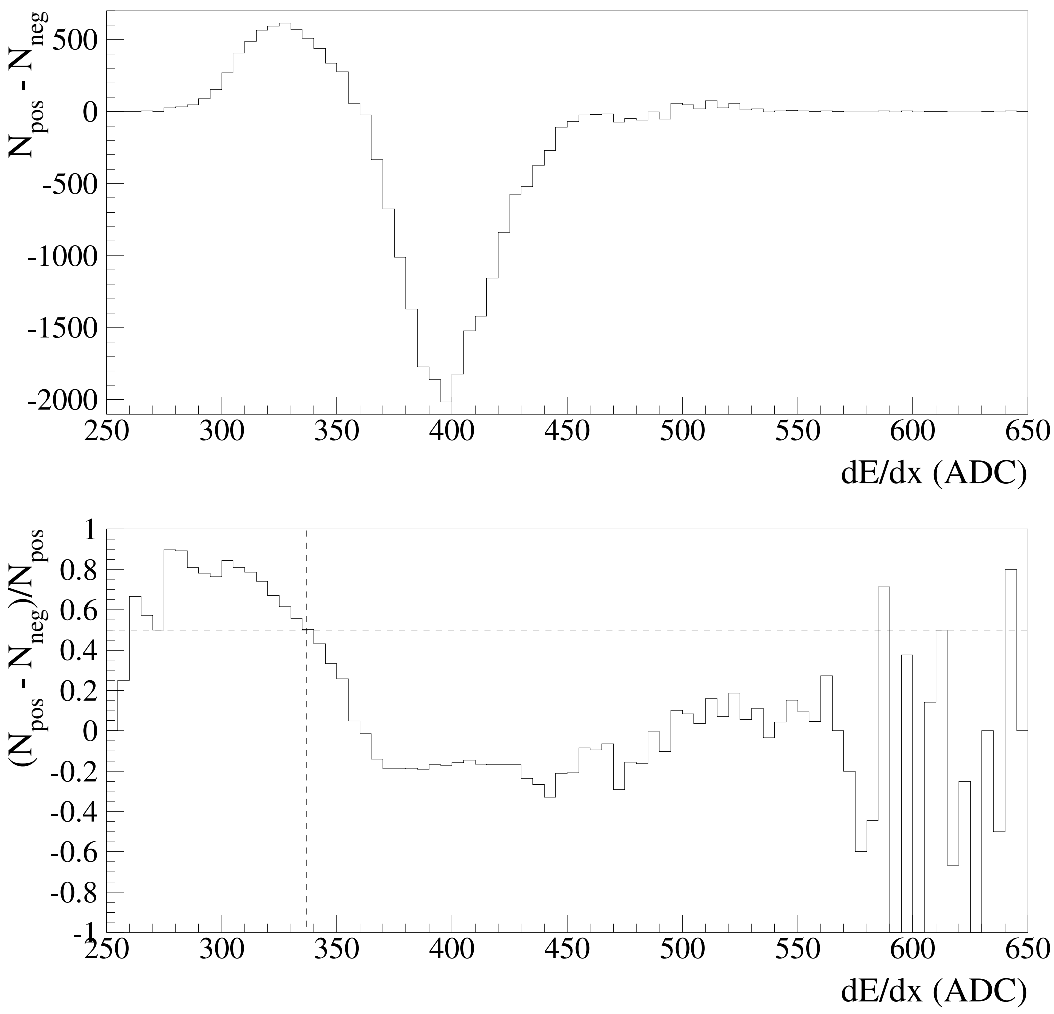

Figure 3.15: +/- comparison method of PID for $p = 5.0 - 5.5$ GeV/c, $p_T = 0.0 - 0.2$ GeV/c. The top plot shows the difference of dE/dx for positive particles - negative particles. The bottom plot is the top plot divided by the dE/dx distribution for positive particles. This creates a value of +1 for regions of dE/dx where all particles seen came from the MTPC containing positive particles, and a -1 for regions where all particles came from the negative MTPC. The positive bump representing protons is clearly visible at low dE/dx values.

In reality, this cut line does not clearly separate protons and pions – there is still overlap both above and below the line. Furthermore, kaons are present in both regions as well, although since they have been seen to have minimal transverse flow [Ritm95] they are not expected to have any real effect on the transverse flow measurements. To minimize these contaminations, the cut line was moved up in dE/dx for pions and down for protons, creating a "no-man's land" in which all particles are ignored. In figure 3.16, these two lines (as well as a simple cut to remove electrons from the pion sample) are plotted on a background of positive particles from about ten events. Anything below the proton line is considered to be a proton, and anything above it (but below the electron cut) is considered a pion. These cuts work well in both main TPCs (once the 1% difference in dE/dx values between the two is corrected for).

This method was tested using the kinematic region in which the TOF wall data was available, $p = 4 - 8$ GeV/c. By comparing to the TOF-identified particles in that region (see figure 3.17), reasonable PID was obtained: almost everything identified as a proton was indeed a proton, and most of what was identified as pion was a pion, with some kaon contamination that should not affect the transverse flow measurements.

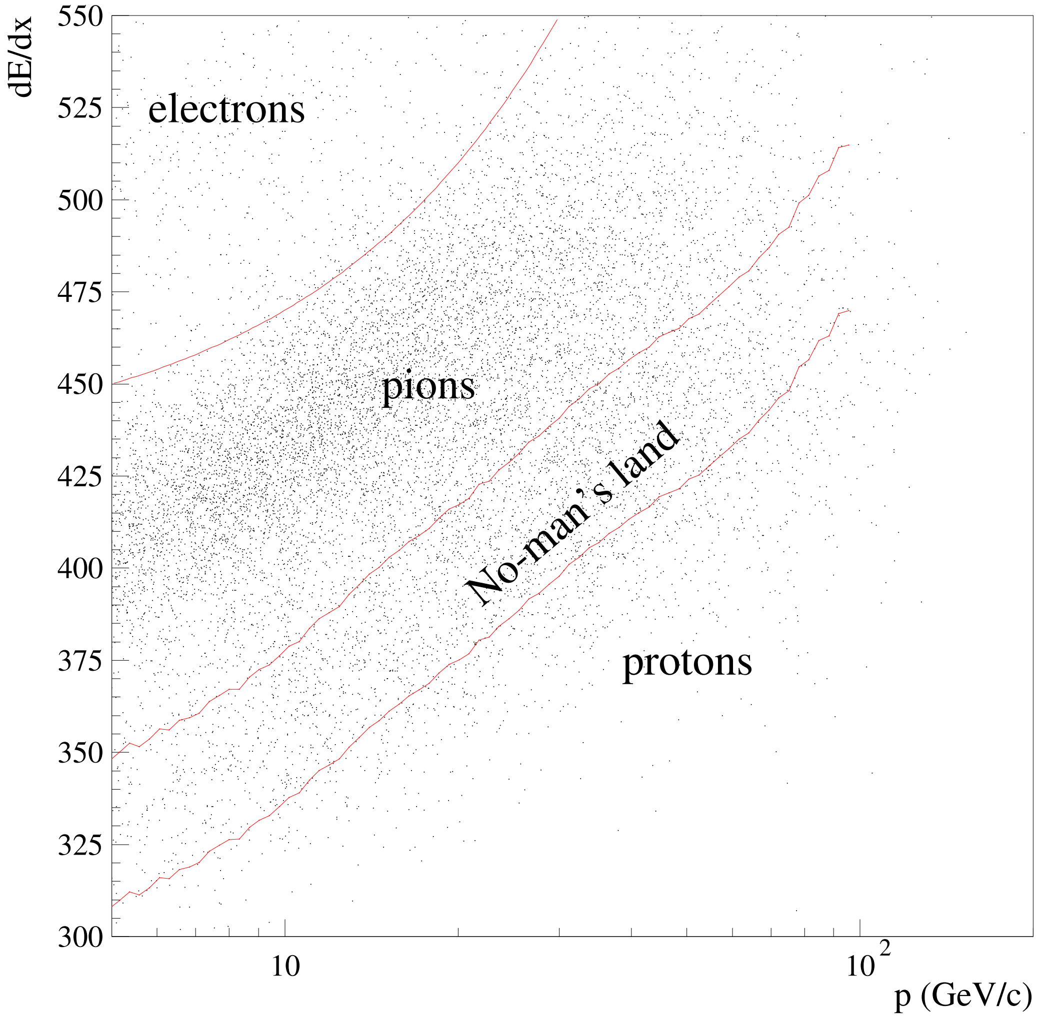

Figure 3.16: dE/dx cuts for proton and pion identification, superimposed on positive particles from about 6 medium-bias events.

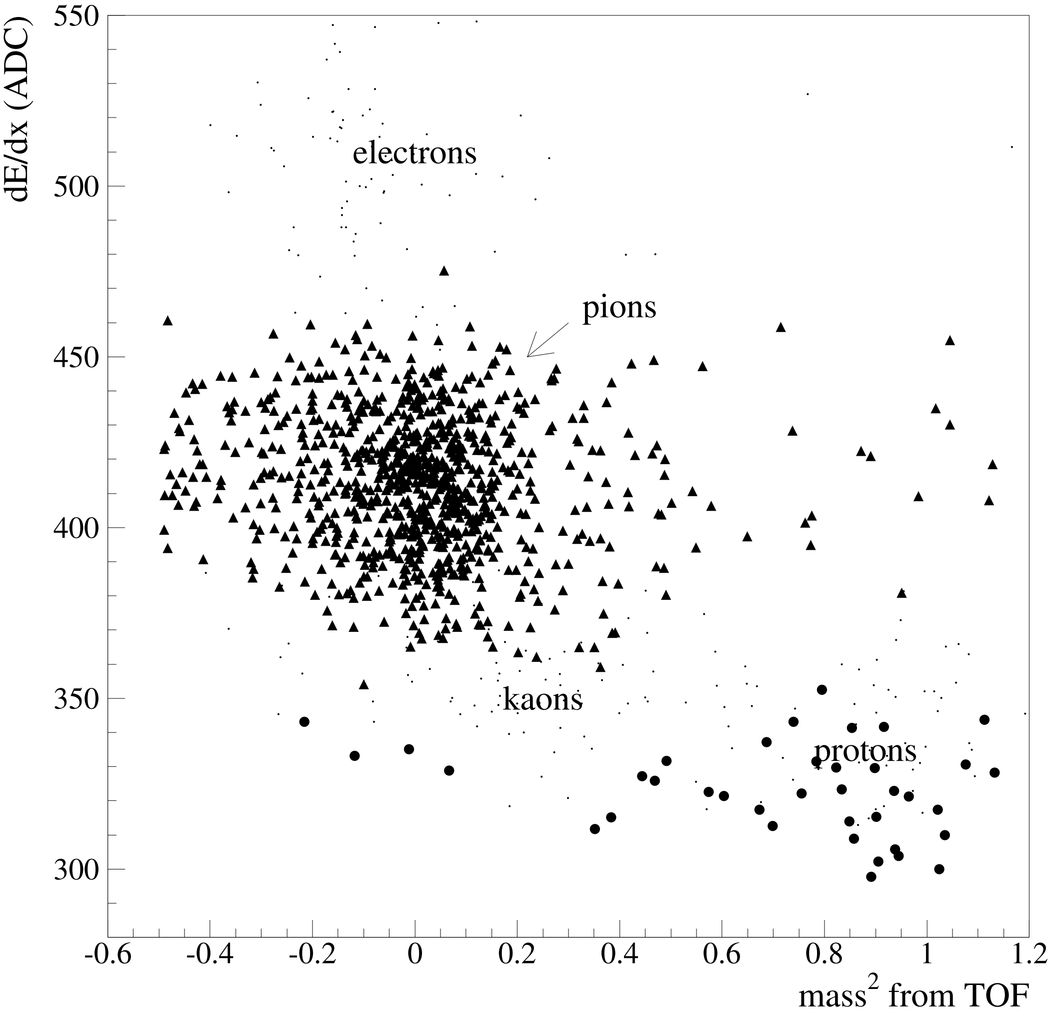

Figure 3.17: Test of particle identification with the TOF data for about six events. The large circles are identified protons, the triangles are identified pions, and the small spots are unidentified particles.

Chapter 4

Transverse Flow in Nuclear Collisions

4.1 Overview

Although some evidence was first found of transverse flow in two-particle correlations [Cser82] and sphericity analysis [Renf84, Gust84], statistical fluctuations hampered the extraction of the flow measurements. This was overcome by what is now the most commonly used method of measuring transverse flow, introduced by Danielewicz and Odyniec in [Dani85]. The measured flow value for the same data can differ greatly depending on the variables and method used, so using a common system between experiments allows direct comparison. This method, as well as some more recent adaptations of it, will be discussed in the first section.

Recent work with calorimeters in measuring transverse energy flow has necessitated the need for a more generic measure of flow. The emerging preferred method has been well-developed theoretically [Olli92, Olli95, Olli97, Posk98] and experimental data has been appearing using this method [Barr94, Hemm96]. It will be discussed in the second section.

4.2 Danielewicz and Odyniec Method

Danielewicz and Odyniec's method was first successfully used to find flow in data that did not show any clear flow signal by other methods [Dani85]. It enables one to find the event plane, measure the flow of particles within that event plane, and also correct for two things: the uncertainly of the event plane determination (section 4.2.3) and the so-called "autocorrelation" effect (section 4.2.4).

4.2.1 Event Plane Determination

In this method, the event plane of each individual collision is determined by measuring the vector direction of the net transverse momentum, i.e.

$$\overrightarrow{Q} = \sum_{i=1}^{N} \omega_i \, \overrightarrow{p_T}_i \tag{4.1}$$

where N is the number of particles in a single event, ω_i is a weighting factor that will be discussed next, and $\overrightarrow{Q}$ is the resulting event plane vector.

The weighting factor ω_i is often taken as

$$\omega_i = \begin{cases} +1 & y > y_{CM} + \delta \\ 0 & y_{CM} - \delta < y < y_{CM} + \delta \\ -1 & y < y_{CM} - \delta \end{cases}$$

although other versions, such as $\omega_i = (y - y_{CM})$, have also been used [Fai87, Awes96] to give greater weight to particles at higher rapidity. The δ parameter is used to avoid including particles near midrapidity which have little event plane signal but would add random fluctuations to the calculation. The negative weighting of the below-midrapidity particles is required so that they do not cancel out the above-midrapidity signal – conservation of momentum of course requires that there be no *net* flow in momentum.

Protons are most commonly used in this calculation since they are expected to show the cleanest flow signal (see chapter 1). However, other produced particles can be used, especially pions because of their greater multiplicity at higher beam energies. For the NA49 flow measurements in this thesis, the pions were used to determine the event plane (see chapter 6).

4.2.2 Transverse Flow Calculation

Once the event plane has been determined, the degree to which each desired particle is aligned with that plane can be determined. In the Danielewicz and Odyniec method, the component of each particle's transverse momentum that lies along the event plane is summed:

$$<p_x> = \sum_{i=1}^{N} \overrightarrow{p_T}_i \cdot \frac{\overrightarrow{Q}}{\left|\overrightarrow{Q}\right|}$$

This has traditionally been done over all particles of a given particle type in the data set, but can also be done on an event by event basis (where N would be the multiplicity of each event). The amount of quark-gluon plasma produced at RHIC energies is expected to fluctuate from event to event, and so it is important to be able to measure flow event by event. Note that event by event measurements of flow will require correction for the detector acceptance – when mean flow is measured for all particle in an event, the acceptance biases average out. When it is measured event by event, however, any acceptance biases will have a definite effect on the flow measured. This is discussed in more detail in section 5.4.

Using all particles for this calculation will give you an overall flow value for the data set, but it is more informative to produce separate flow values for different rapidity regions, producing the "S-shaped" curve seen in figure 1.4. A convenient method of describing the magnitude of this flow is the parameter F, defined as the slope at $y = y_{CM}$ of the $<px>$ values plotted versus normalized rapidity $y_N = (y - y_{CM})/y_{CM}$. This parameter will be examined in the results section of this thesis.

4.2.3 Subevent Correlation

All of the flow measurements mentioned above are for a perfect event plane, i.e. when the event plane is found exactly. In reality, the event plane is only approximately known, and this has a known effect on the measured flow values. This can be corrected for by a correction value (greater than one) that is applied to all flow measurements.

The flow measured is effectively the centerpoint of a line drawn along the event plane direction across the circle in figure 4.1, which represents the distribution of

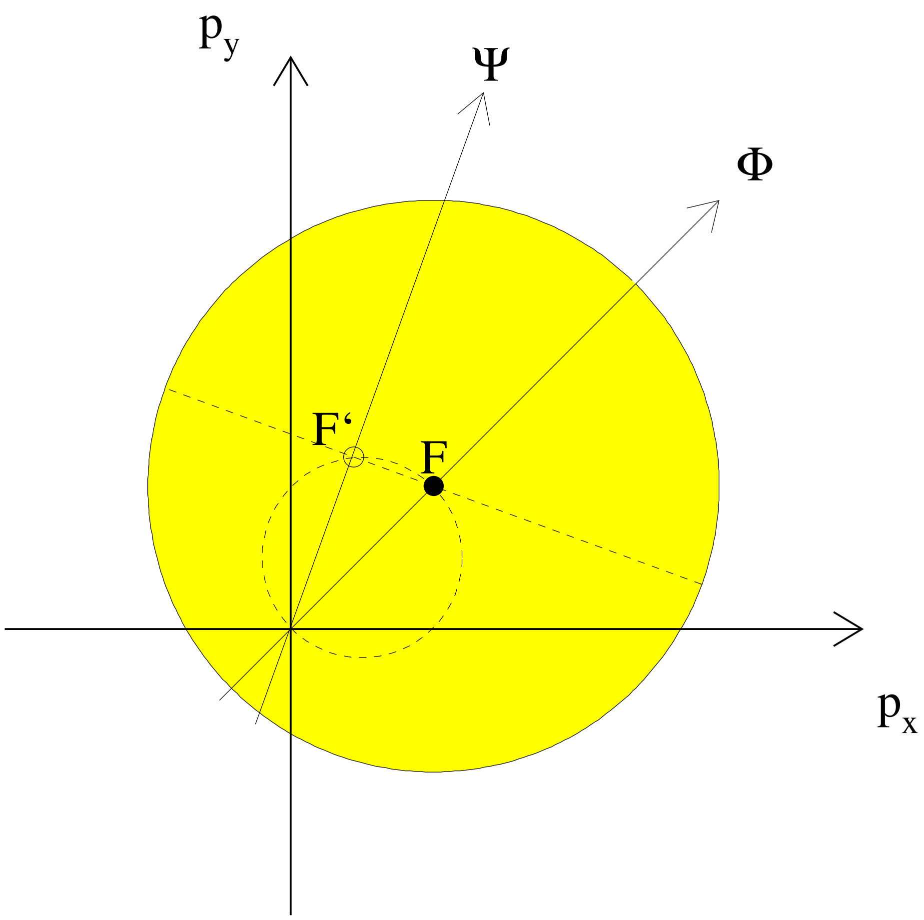

Figure 4.1: Illustration of deviation of flow values due to uncertainly in the event plane. The shaded area represents particles with $y > y_{CM}$ and a continuous distribution in p_T around the mean flow value F. Φ represents the true event plane, and Ψ an approximate found plane with measured flow value F'.

particles' p_T in the lab frame (only particles above midrapidity are shown here). This is represented in the figure by the vector ending at point F along event plane Φ. If the event plane is known perfectly, then the true flow value at point F is the value found. If the event plane found deviates from the true plane, however, the effective flow value is reduced. For example, if the incorrect event plane Ψ in figure 4.1 is used instead, then the midpoint of the line along the incorrect midpoint, F', is obtained instead. This point can be found geometrically in the figure by drawing a line perpendicular to the found event plane that evenly bisects the circle (and, by definition, crosses through the center of the circle which is simply the true flow value along the true event plane). After considering F' at several values of Ψ ($F' = 0$ at $(\Psi - \Phi) = \pm 90°$ and $-F$ at $180°$ – the point F' traces out a circle as Ψ goes from $0°$ to $360°$), it should be simple to see that the measured flow signal is related to the true one by

$$F' = F\cos(\Psi - \Phi)$$

If this is averaged over many events, we get

$$<F'> = <F><\cos\Delta\phi> \tag{4.2}$$

where $\Delta\phi = \Psi - \Phi$ is the error in the event plane calculation.

The central limit theorem requires that the fluctuations of the event plane vector $\overrightarrow{Q}$ about its average value $\overline{Q}$ form a gaussian distribution with width σ. Ollitrault shows [Olli97] that the $<\cos\Delta\phi>$ term can be written as the function of a single dimensionless parameter $\chi = \overline{Q}/\sigma$. From this, the $<\cos(\Delta\phi)>$ term in equation 4.2 can be written in terms of χ as

$$<\cos(n\Delta\phi)> = \frac{\sqrt{\pi}}{2}\chi e^{-\chi^2/2}\left[I_{\frac{n-1}{2}}(\frac{\chi^2}{2}) + I_{\frac{n+1}{2}}(\frac{\chi^2}{2})\right] \tag{4.3}$$

where I_k is the modified Bessel function of order k, and n represents the order of the cosine term looked at ($n = 1$ for this discussion, but see section 4.3 for higher-order terms). This function is plotted in figure 4.2 for $n = 1, 2$.

The most common method used to determine the accuracy of the event plane calculation is to divide the event into two random subevents containing half the

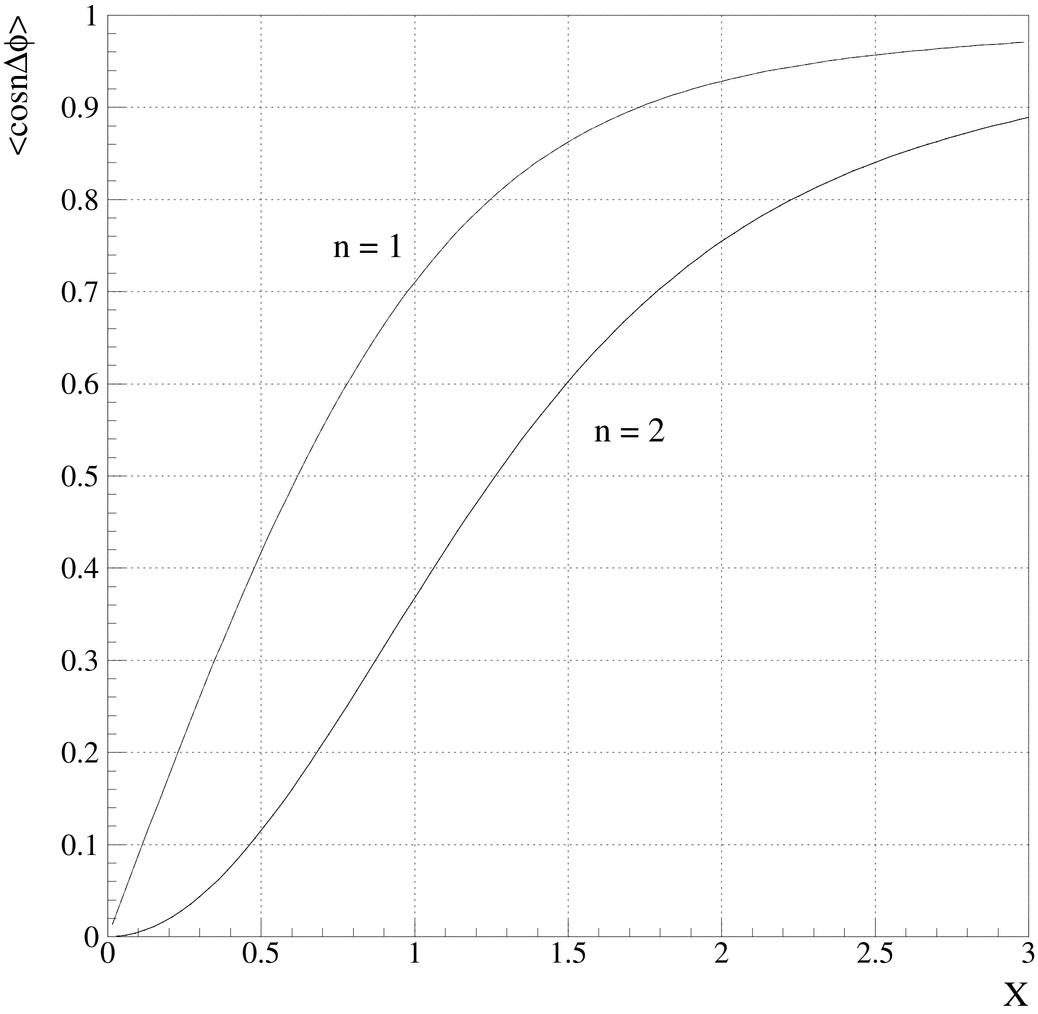

Figure 4.2: <$\cos(n\Delta\phi)$> for $n = 1, 2$, as defined in equation 4.3.

particles, calculate the event plane $\overrightarrow{Q}$ separately for each subevent, and examine the distribution of the difference between the two, $\Delta\Phi_{AB} = \Phi_A - \Phi_B$. This distribution can be used to determine the value of χ, which provides the correction factor for the flow measurements as in equation 4.3. Specifically, a convenient method uses the ratio of events with $|\Delta\Phi_{AB}| > 90°$, $N_{>90°}$, to the total events N_{tot} [Olli97]:

$$\frac{N_{>90^\circ}}{N_{tot}} = 0.5\, e^{-\chi^2/2} \tag{4.4}$$

A more accurate method when χ is large (the ratio in equation 4.4 is small for large values of χ and statistical fluctuations have a larger effect) involves measuring the mean value of $\cos\Delta\Phi_{AB}$ and using the following relation:

$$\begin{aligned} <\cos\Delta\Phi_{AB}> &= <\cos\Delta\phi_A><\cos\Delta\phi_B> \\ &= \frac{\pi}{8}\chi^2 e^{-\chi^2/2}\left[I_0(\frac{\chi^2}{4}) + I_1(\frac{\chi^2}{4})\right] \end{aligned}$$

where we have used equation 4.3 with $n = 1$ and replaced $\chi/\sqrt{2}$ for χ_A and χ_B to properly scale due to the subdivision of the event. In the case of this thesis, however, the values of χ are sufficiently small to allow use of equation 4.4.

4.2.4 Autocorrelation Correction

When collective motion of particles in nucleus-nucleus collisions was first being studied, it was discovered that finite multiplicity effects could affect the apparent flow signal to a surprising degree when the Danielewicz and Odyniec method was used [Dani83]. The effect is to the order of $O(1/\sqrt{M})$ and is greater for distributions of small flow angle (i.e. smaller transverse flow).

Simply put, this "autocorrelation" effect is due to comparing a particle to a distribution that contains that same particle. In the case of transverse flow, if the particle whose flow is being measured vs. the event plane was used in determining that event plane, the correlation between the particle and the event plane is higher than it would be for an infinite distribution. On the other hand, if the flow of a particle that was not used in the event plane determination was being measured, there would be no autocorrelation effect.

To avoid this autocorrelation, we can recalculate the reaction plane for each particle without using the particle in question, identified here with the index j:

$$<p'_x> = \sum_{i=1}^{N} \overrightarrow{p_T}_i \cdot \frac{\overrightarrow{Q'_i}}{\left|\overrightarrow{Q'_i}\right|} \tag{4.5}$$

where $\overrightarrow{Q'_i}$ is given by

$$\overrightarrow{Q'_i} = \sum_{j=1,\, j\neq i}^{N} \omega_j \, \overrightarrow{p_T}_j$$

The flow value produced using this method is approximately the true value. There will be a reduction in the measured flow magnitude due to the greater uncertainty of the event plane, but it is typically quite small.

To get a better feeling for autocorrelation, a simple simulation was run for various event configurations. 100,000 events containing a fixed number of particles and a fixed value of number flow (the method of adding number flow is described in appendix C) was analyzed for flow signals. Comparisons can then be made between events with differing numbers of particles and flow signal.

As can be seen in figure 4.3, there is a direct correlation between the number of particles used to determine the event plane and the magnitude of the correlation effect. It can also be seen, however, that using the method discussed here resolves the problem, providing flow values within a few percent of the actual ones. By comparing between plots in figure 4.3, the relation between the autocorrelation effect and flow magnitude can also be seen. As was stated earlier, it is clear the smaller flow signals increase the autocorrelation effect. Hence, autocorrelation should be a big effect at SPS energies since the flow is expected to be small, and correction for it is required.

4.2.5 Recent Adaptations

Recently, the Danielewicz and Odyniec method of transverse flow analysis has been used in slightly different ways. Several of these analysis methods are discussed briefly in the following paragraphs.

The E866 spectrometer experiment was able to determine the event plane using the E_T projectile spectator fragments in the forward hodoscope [Ahle98] instead of

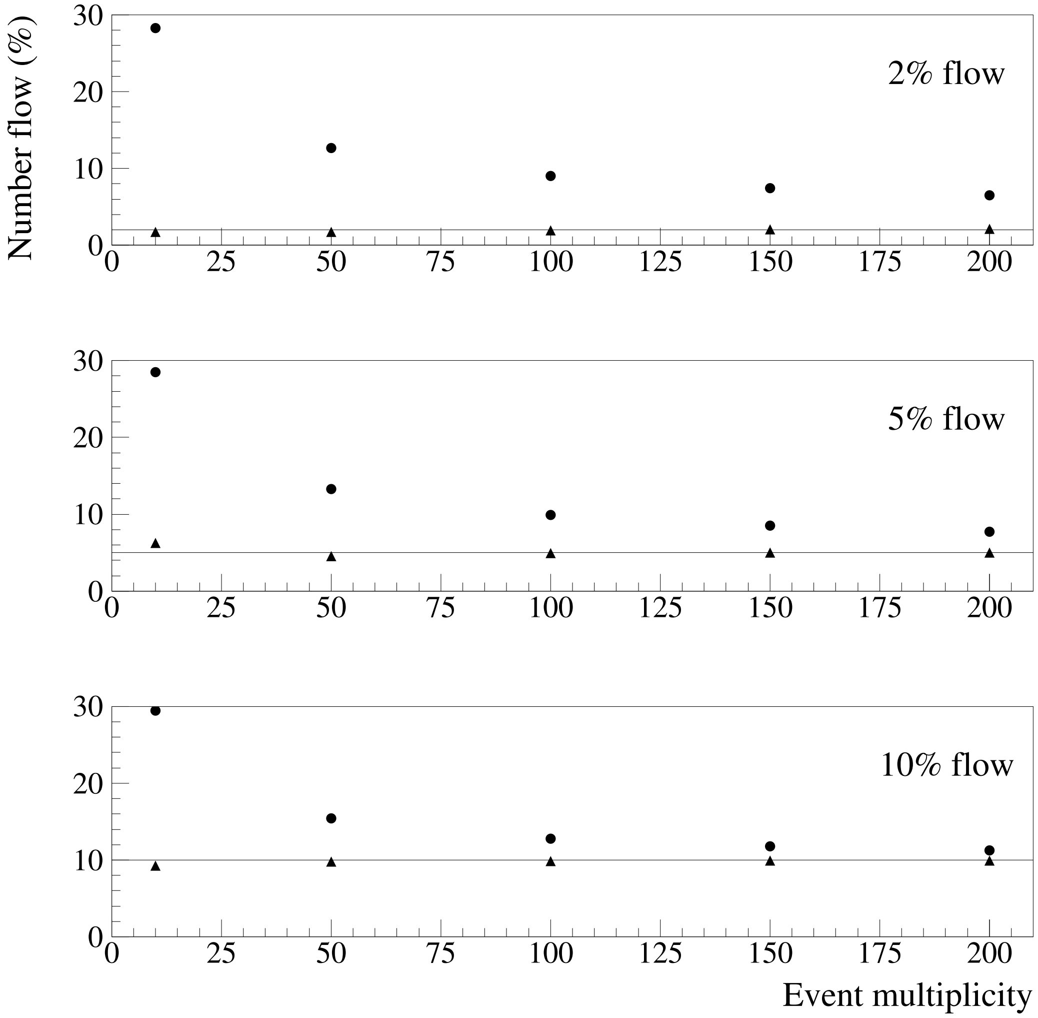

Figure 4.3: Variation of autocorrelation effects for various event sizes. Circles represent uncorrected flow measurements (number flow for all particles), and the triangles are flow values corrected for both autocorrelation and event plane resolution.

the p_T of the fragments. This allowed them to measure the flow signal of particles detected in the spectrometer arm (and avoided any autocorrelation effects).

Number flow has been increasingly looked at as a measure of transverse flow. By ignoring p_T, acceptance problems can be avoided and general event shapes can be examined more effectively – measurements like the squeezeout ratio R_{sq} (described in section 4.4) are less sensitive at small flow magnitudes. By leaving out the p_T term in equation 4.5, $<\cos\phi>$ is actually measured:

$$<\cos\phi> = \sum_{i=1}^{N} \hat{\phi}_i \cdot \frac{\overrightarrow{Q}}{\left|\overrightarrow{Q}\right|}$$

where $\hat{\phi}_i$ is the directional vector of the transverse momentum of particle i. However, it should be pointed out that, although number flow and the more traditional p_T flow are related, they are not identical and may have different implications. This will be examined in greater detail in chapter 6.

4.3 Azimuthal Correlations Method

A newer method of studying transverse flow effects is based on Fourier analysis of some characteristic of the event (p_T, E_T, etc.). This has been described in [Olli92, Olli93, Volo96], and successfully used in several AGS and SPS experiments, specifically E877 [Barr94, Hemm96, Barr97] and using the NA49 calorimeter [Wein96, Huan97]. It has the advantage of avoiding the autocorrelation effect since the flow value is not measured by comparing it to the event plane, but has the disadvantage of some built-in assumptions. As it was not used in this thesis, only a brief description of the method will be given here, but the relation between this method and the Danielewicz and Odyniec method discussed in the previous section will be pointed out.

4.3.1 Fourier Moments

This method simply separates the distribution of the variable of interest (written as $r(\phi)$ here) into separate Fourier components, i.e.

$$r(\phi) = \frac{x_0}{2\pi} + \frac{1}{\pi}\sum_{n=1}^{\infty}\left[x_n\cos(n\phi) + y_n\sin(n\phi)\right] \tag{4.6}$$

where ϕ is measured in the lab frame. From standard Fourier analysis, we know that [Arfk85]

$$x_n = \int_0^{2\pi} r(\phi)\cos(n\phi)d\phi$$
$$y_n = \int_0^{2\pi} r(\phi)\sin(n\phi)d\phi$$

Or, for a finite number of particles,

$$x_n = \sum_{\nu} r_\nu \cos(n\phi_\nu)$$
$$y_n = \sum_{\nu} r_\nu \sin(n\phi_\nu)$$

where ν identifies the particle of interest, r_ν and ϕ_ν represent the variable of interest and the azimuthal angle of particle ν, and we are measuring the nth Fourier term.

The laboratory event plane Ψ_n and flow measurement value v_n for the nth component can be determined from the x_n and y_n terms:

$$v_n = \sqrt{x_n^2 + y_n^2}$$
$$\Psi_n = \tan^{-1}(y_n/x_n)$$

From these, we can write the overall flow vector

$$\overrightarrow{v_n} = (v_n, \Psi_n)$$

4.3.2 Flow Calculation

Once these values have been determined, one can examine the distribution of v_n. If there is no flow present, the central limit theorem requires that a distribution of dN/dv_n^2 will form a gaussian centered on zero, i.e.

$$\frac{1}{N}\frac{dN}{v_n dv_n} = \frac{\exp\left(-\frac{v_n^2}{2\sigma^2}\right)}{\sigma^2} \tag{4.7}$$

However, the presence of flow will shift the centroid of this distribution by the amount $\tilde{v}_n$. The distribution is then described by [Volo96]

$$\frac{1}{N}\frac{dN}{v_n dv_n} = \frac{1}{\sigma^2}\exp\left(-\frac{\tilde{v}_n^2 + v_n^2}{2\sigma^2}\right) I_0\left(\frac{\tilde{v}_n v_n}{\sigma^2}\right) \tag{4.8}$$

where I_0 is the modified Bessel function of 0th order.

If the flow is large ($\tilde{v}_n > \sqrt{2}\sigma$), a minimum will appear at $v_n = 0$, providing an obvious flow signal. If this is not the case, a more detailed fit of the distribution using equation 4.8 is necessary. In [Barr94], the E877 collaboration simultaneously fit the distributions for the first four Fourier moments, with two restrictions: $\tilde{n}_3 = 0$ (for symmetric systems) and σ is a common value for all distributions. These fits provided definite flow measurements over a range of centralities. For more details, see [Volo96] and [Barr94].

Note that this method *assumes* that the degree of flow present from event to event only varies statistically. If this is not the case, then the flow values measured will be incorrect. The Danielewicz and Odyniec method averages the flow values from all events, but the azimuthal correlations method will produce a poor fit if the flow varies – the sum of two distributions of equation 4.8 with different values of $\tilde{v}_n$ does not produce another distribution that has the form of equation 4.8.

4.3.3 Relation to Danielewicz and Odyniec

The 1st-order Fourier term in this method is directly related to the "directed flow" as measured by the Danielewicz and Odyniec method in section 4.2. In fact, if $r_\nu \rightarrow p_{T\nu}$ in equation 4.6 and $\omega \rightarrow 1$ in equation 4.1, then the event plane calculation simply provides the flow vector for the entire event: $\overrightarrow{Q} = \overrightarrow{v_1}$.

The calculation of $<p_x>$ can also be directly related to this method. Again, if $r_v \equiv p_{Tv}$, then $\tilde{v}_n = <p'_x> N$, where N is the number of particles in the set being examined. Although autocorrelation correction is unnecessary when using this method, the correction for the event plane resolution as written in equation 4.3 is still necessary.

4.4 Elliptical Flow

Another transverse flow measurement of interest is the ellipsoidal shape of a distribution. This was first measured as "squeeze-out", or the emission of particles 90° from the event plane. The measurement made was the number squeeze-out ratio,

$$R_N = \frac{\frac{dN}{d\phi}(90^\circ) + \frac{dN}{d\phi}(-90^\circ)}{\frac{dN}{d\phi}(0^\circ) + \frac{dN}{d\phi}(180^\circ)}$$

i.e. the ratio of the number of out-of-plane particles to in-plane particles (where the event plane was found through the Danielewicz and Odyniec method) [Gutb90]. To determine this value more accurately, fits can be made of the particle distribution to the function

$$\frac{dN}{d\phi} = N\left[1 + S_1 \cos(\phi - \Phi) + S_2 \cos(2(\phi - \Phi))\right]$$

where Φ represents the event plane [Kint95]. The similarities between this function and equation 4.6 are obvious.

The NA49 ring calorimeter has been used to measure elliptical flow near midrapidity [Wein96, Huan97]. By using the azimuthal correlation method, the E_T flow magnitudes for the 1st and 2nd terms were determined. These results will be discussed in chapter 6.

Chapter 5

Correction for Detector Acceptance

5.1 Overview

The NA49 detector was designed to maximize particle detection in y and p_T, but azimuthal coverage was not considered a high priority. As an extreme example, the vertex TPCs are purposely designed with an insensitive region in the center so the beam can pass through without overwhelming the electronics. Although this greatly simplifies the detector design, it unfortunately destroys full azimuthal coverage.

The situation is not as bad in the main TPCs. For much of the kinematic region covered by the MTPCs, azimuthal coverage is at least partial for large ranges of p_T. However, the regions that fall along the TPC sides nearest and furthest from the beamline have larger problems (see figure 5.1 for an example, and Appendix A for all acceptance plots used in the correction). If acceptance were perfect, no dependence would seen in ϕ and the p_T distribution would be approximately a simple exponential dropoff. Simple inclusion of all particles detected cannot provide a true event plane due to the biases created by uneven acceptance.

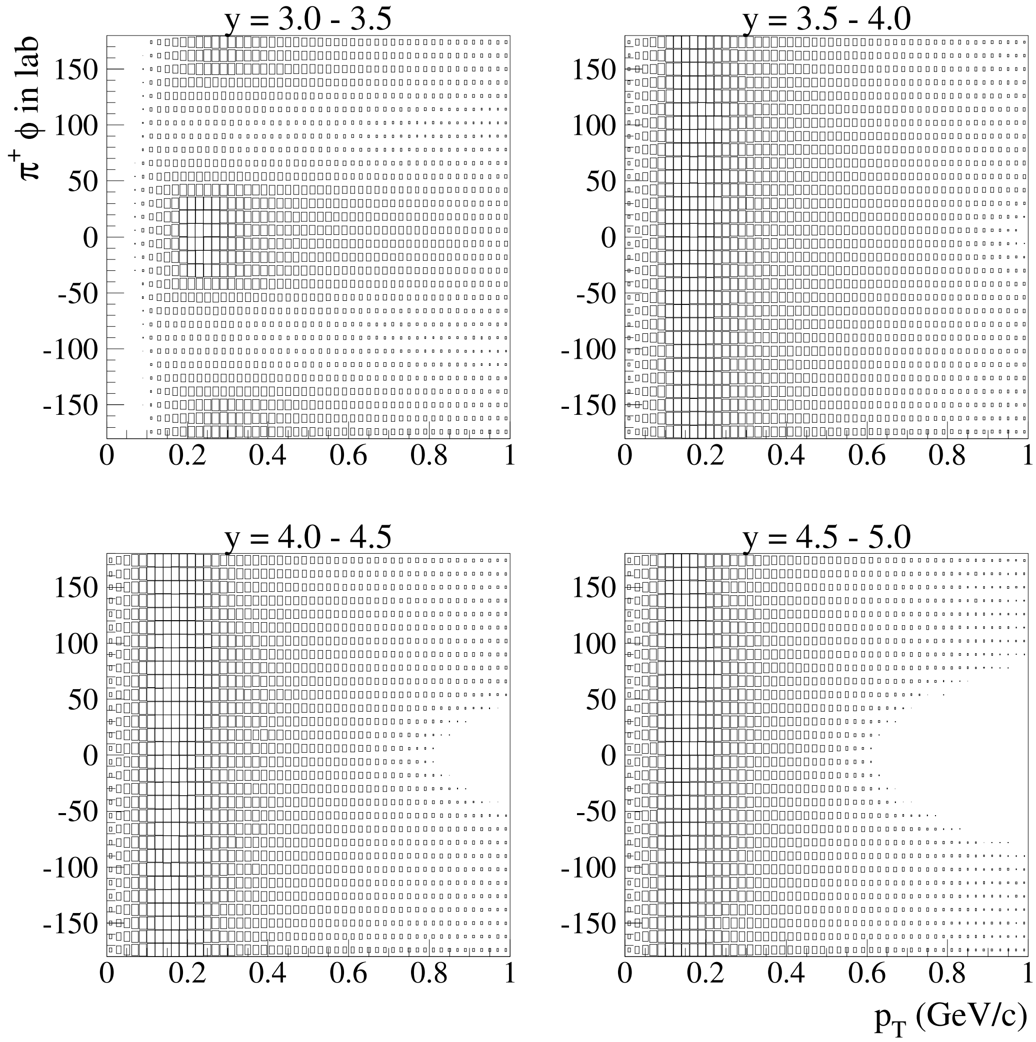

Figure 5.1: Positive pions accepted in the MTPCs for various rapidity ranges. These plots are histograms; the size of each box is proportional to the number of counts in that bin.

5.2 Acceptance Correction Calculation

In general, the simpler a detector is the easier it is to correct for the detector's acceptance. For example, in the WA93 experiment at CERN a simple bias is generated from the magnetic field present, but can be easily removed as well [Agga97]. Unfortunately, in NA49 acceptance of the main TPCs is much more complicated, as is seen in figure 5.1 and Appendix A – no obvious simple function will fit the acceptance distributions. To make an acceptance correction, a bin-by-bin acceptance correction is necessary.

The accepted particles are first divided into bins by

- rapidity (12 bins of width 0.5, $y = 0 - 6$)
- p_T (50 bins of width 0.05 GeV/c, $p_T = 0.0 - 1.0$ GeV/c)
- azimuthal angle ϕ (30 bins of width 12°, $\phi = -180° \ - \ 180°$)
- particle type (protons, π^-, and π^+)

The acceptance correction weight for a single particle type (proton, π^+, or π^-) is defined as $\omega(y, \phi, p_T)$, and is calculated as follows:

1. Tables of particle counts for all events, $\mu(y, \phi, p_T)$, are filled using the rapidity, ϕ, and p_T bins mentioned above. These tables are seen in thefigures in Appendix A),
2. For a given subset of bins with identical rapidity and p_T (a vertical row on any plot in appendix A), the bin with the maximum value is found and its value is defined as $\mu_{max}(y, p_T)$.
3. For each bin in the selected row, the value needed to scale it to that maximum value is calculated:

$$\omega(y, \phi, p_T) = \frac{\mu_{max}(y, p_T)}{\mu(y, \phi, p_T)}$$

These correction factors are then applied to particles with the corresponding indices for the event plane calculation, effectively increasing the number of particles in that bin by the scaling factor.

A simple test that the individual correction factors for each bin are correct can be made by checking the counts in the bins shown in figure 5.1 and Appendix A after each particle has been multiplied by the correct ω_x. If the acceptance correction is the proper one, then all bins in each row along ϕ should have equal contents. An example of this correction can be seen in figures 5.2 and 5.3.

It should be pointed out that, for the event plane calculation, the value that the bins are rescaled to does not matter – those values do not directly affect the event plane calculation. However, if these correction factors are to be applied to the flow values as well, these values become important. More will be said on this in section 5.4.

5.3 Acceptance Correction Results

To test this correction method, the event planes can be calculated without and with these correction factors and then a distribution of event planes can be plotted. In the ideal case, the corrected event planes' Φ should have a flat, uniform distribution since the event plane should have no correlation with the lab frame. The results of this test on uncorrected data are shown in figure 5.4. It is quite obvious that the detector acceptance puts a strong sinusoidal bias on the event plane distribution, and using this incorrect event plane would destroy our results due to the small size of the transverse flow at these energies.

The flatness of the corrected figure can be used as a figure of merit for the acceptance correction. In this work, the flatness was estimated by fitting

$$N = A + B_1 \cos(\mu_1 + \phi) + B_2 \cos(\mu_2 + 2\phi)$$

to the distribution (see figure 5.5), where μ_1 and μ_2 allow the cosine terms be centered anywhere in the distribution.

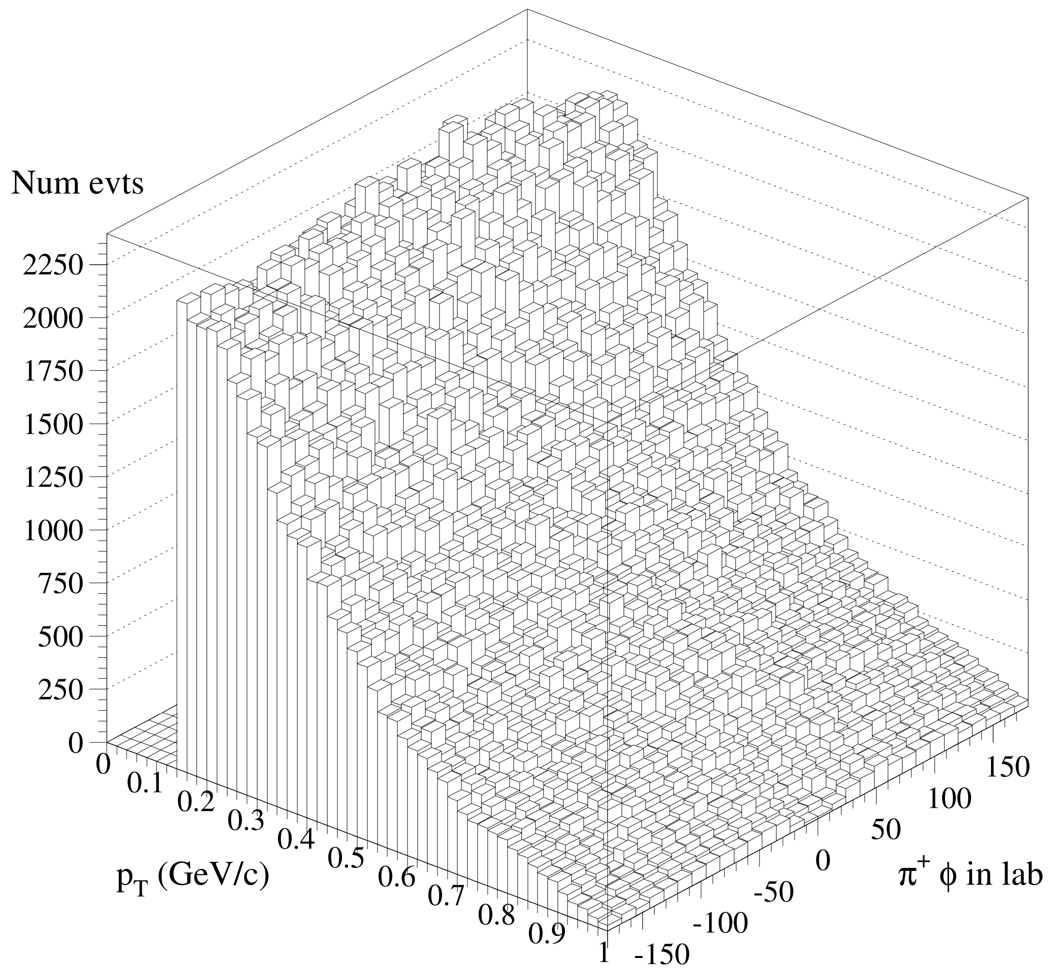

Figure 5.2: Positive pions accepted in the MTPCs, not corrected for acceptance, y = 3.5-4.0. Compare to the acceptance-corrected data in figure 5.3.

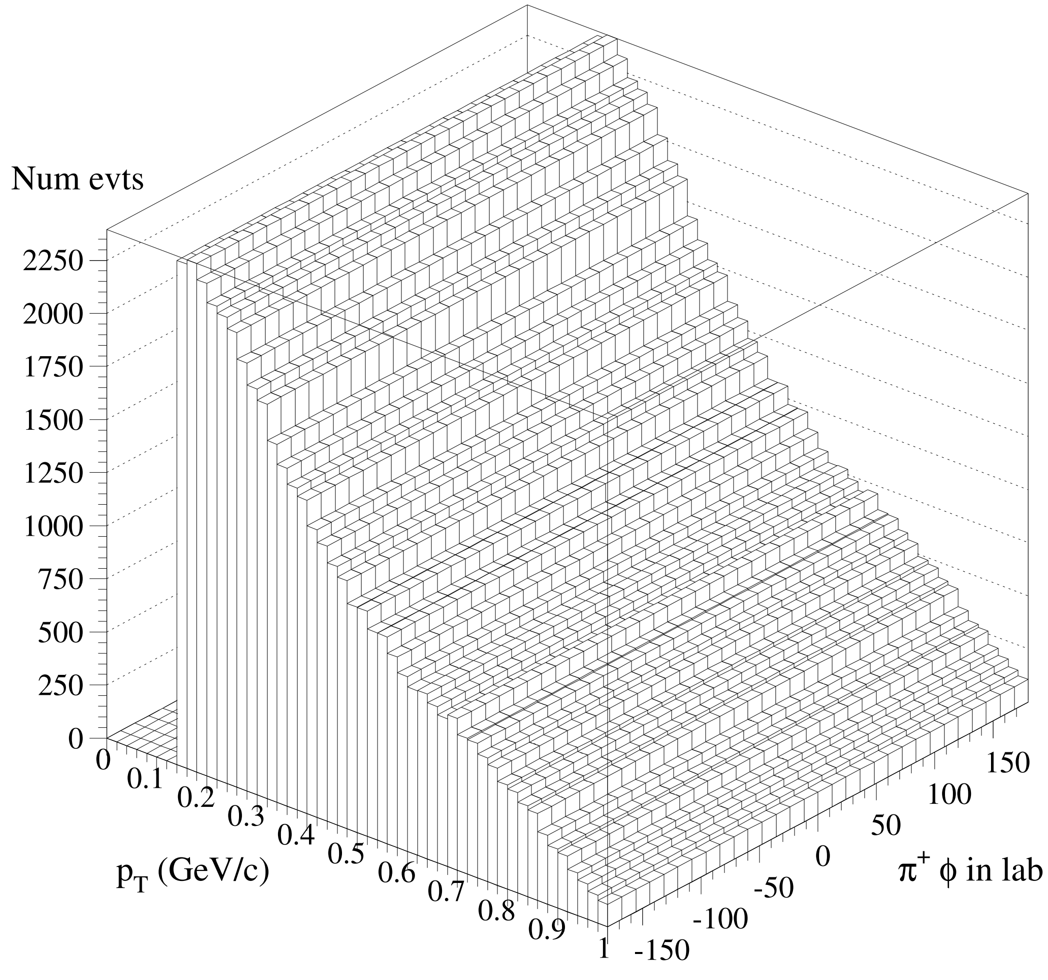

Figure 5.3: Positive pions accepted in the MTPCs and corrected for acceptance, y = 3.5-4.0. The correction should flatten the ϕ distribution for each slice in y and p_T, as can be seen here.

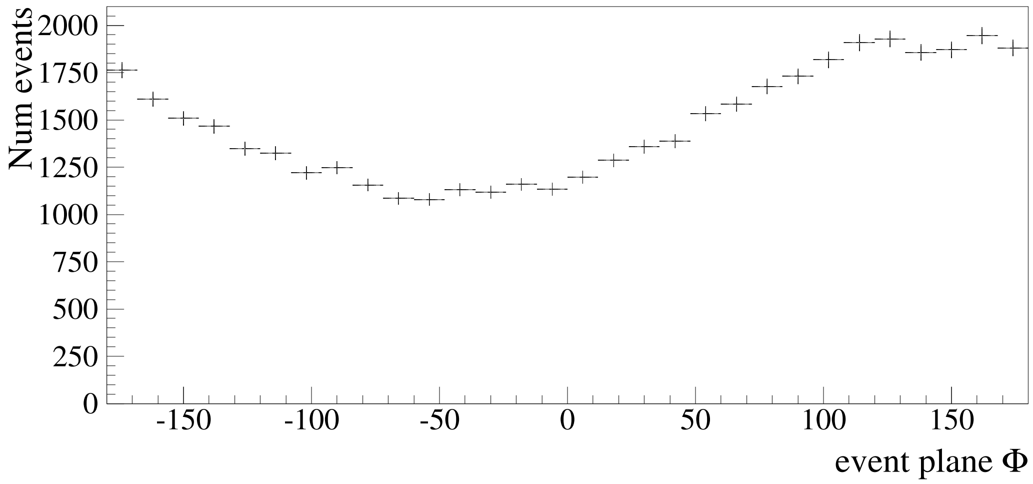

Figure 5.4: Event plane distribution calculated without acceptance correction.

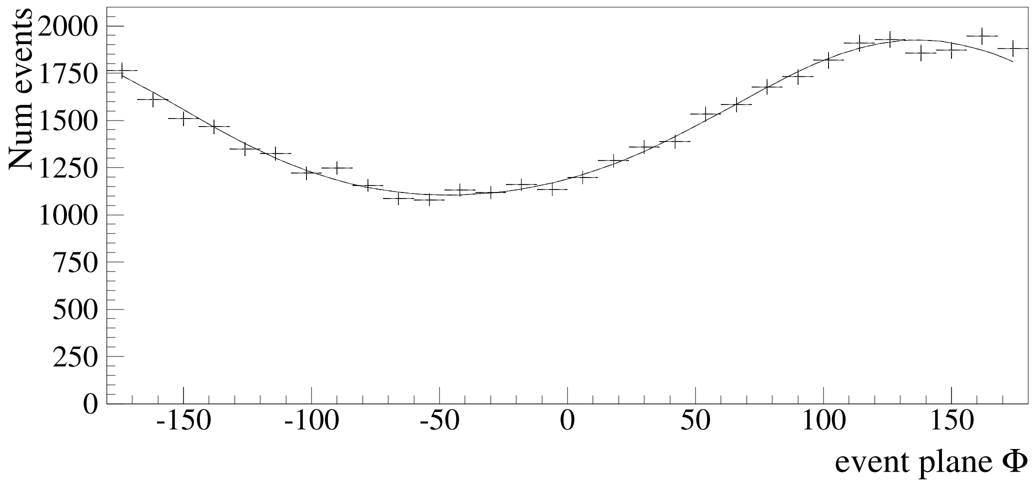

Figure 5.5: Uncorrected event plane distribution with fits. The $cos(\phi)$ term has a 13.88% magnitude, while the $cos(2\phi)$ term has a 1.33% magnitude.

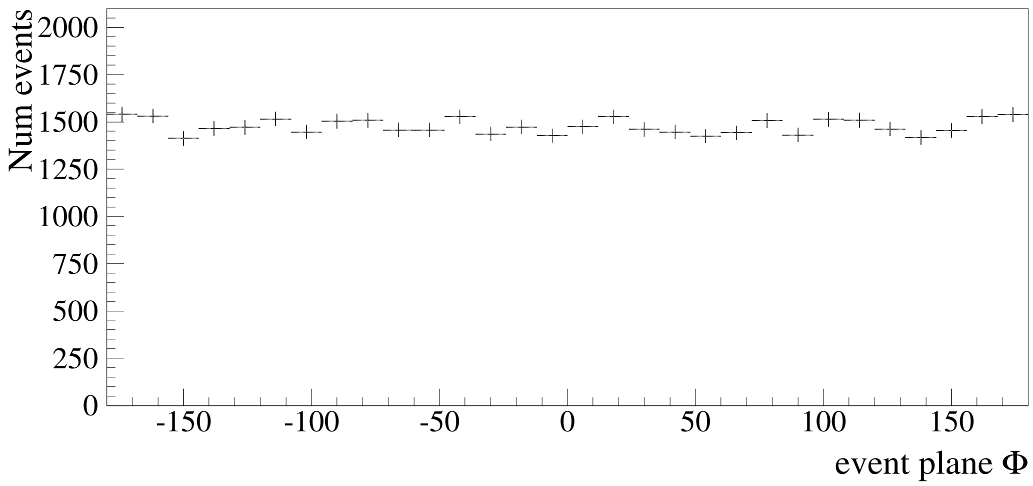

Figure 5.6: Event plane distribution calculated with acceptance correction.

A useful measure of the size of the $\cos(\phi)$ and $\cos(2\phi)$ terms is

$$\frac{B_n}{2A}$$

which is simply a measurement of the fraction of the total distribution that is a $\cos(n\phi)$ distribution. These are reported in the figure captions as percent values.

When the acceptance corrections are applied to the data, the resulting distribution is much more even, as seen in figure 5.6. The actual $\cos(\phi)$ and $\cos(2\phi)$ fit is seen in figure 5.7. An important consideration in this calculation is that if these terms are of the same magnitude as the actual measured flow values, then those flow values would be suspect.

5.4 Applying Acceptance Corrections to Flow

In all previous experiments that measured transverse flow, acceptance corrections were used to correct the event plane calculation but not in calculating the values in any way. When the net flow of all particles in a run is measured (the traditional

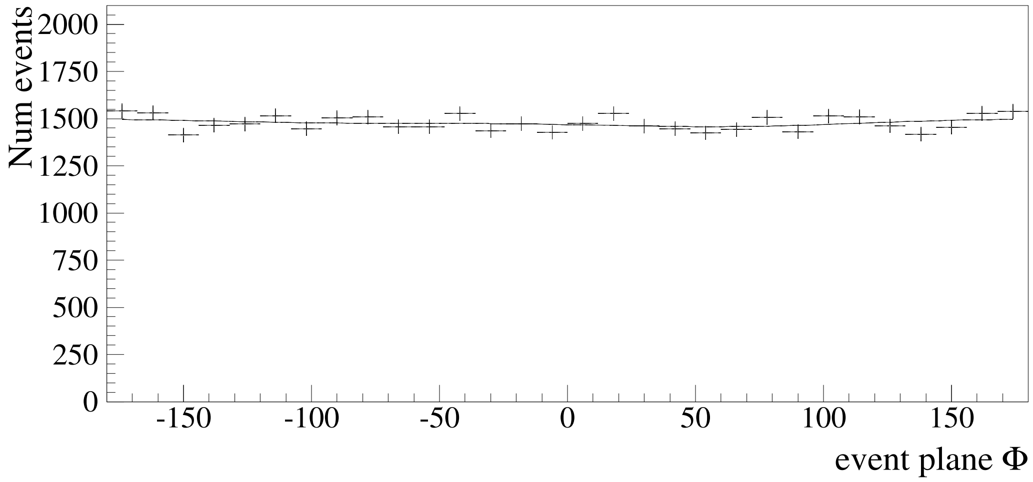

Figure 5.7: Corrected event plane distribution with fits. The $cos(\phi)$ term has a 0.051% magnitude, while the $cos(2\phi)$ term has a 0.234% magnitude.

method), the detector acceptance assymetry will average out due to the random orientation of the event plane from event to event. On the other hand, if flow is measured separately for each event and the acceptance correction is applied to the particles, then the uncertainly in the flow values for each event is limited only by the statistics and not by the acceptance biases.

In the NA49 MTPCs, this is especially the case – in many kinematic regions the p_T acceptance changes drastically with ϕ.

To partially correct for this, two things are done: first, the particles used for flow measurements are restricted to regions of complete ϕ coverage, i.e. only regions of p_T that have particles in all bins along ϕ are used, as was done for the event plane calculation. Second, the correction factor calculated in section 5.4 is applied to the flow value of each particle, where the μ_{max} was chosen as the bin with the maximum number of counts. This has the effect of "filling in" the regions where particles are lost due to accepance limitations by increasing the weight of any particles that were accepted in that region.

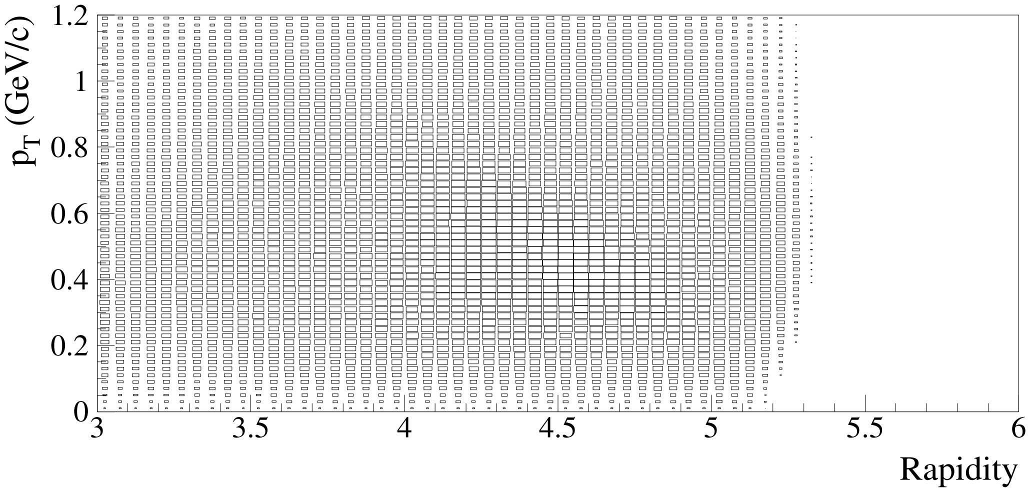

Figure 5.8: p_T vs. rapidity distribution of protons in the main TPCs. Compare to the pions distribution in figure 5.9.

To avoid any holes in ϕ coverage, the detector acceptance was examined in p-θ-ϕ space (where $\theta = p_T/p_z$) and maximum and minimum values of θ were chosen to enclose regions of complete ϕ coverage. This phase space was chosen over the rapidity-p_T-ϕ phase space because it provided better event plane resolution; however, the improvement may simply be an effect of the finer binning used in the p-θ-ϕ calculation. In future studies a finly-binned rapidity-p_T-ϕ acceptance would most likely provide similar resolution. The particles that are accepted by these cuts can be seen in figures 5.10 and 5.11. Note that these stringent cuts will have a definite effect on the p_T-weighted flow measurements.

This approach assumes that, for given values of rapidity and p_T, there is at least one ϕ bin with no track loss (the bin with the most counts) and corrects the remaining regions of ϕ to that expected value. This should improve the flow values, but of course it does not correct for p_T acceptance, which is not complete. A p_T hole exists in the pion distribution due to the detector acceptance, as can be seen in figure 5.9. At rapidities above the p_T hole, p_T coverage looks reasonable. This can be seen by

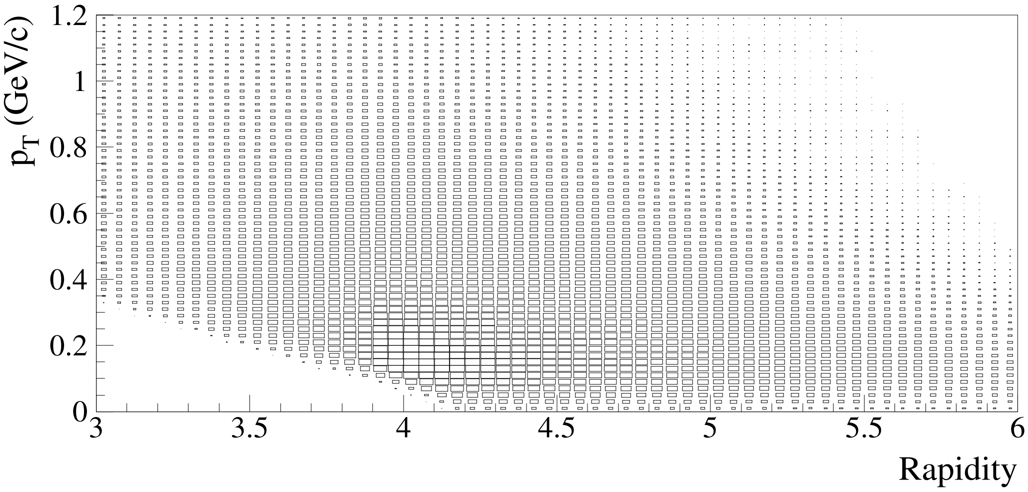

Figure 5.9: p_T vs. rapidity distribution of pions in the main TPCs. Note the hole at low p_T caused by detector acceptance.

looking at figure 5.3: the p_T side of the plot is approximately an exponential dropoff, which is expected. For lower rapidity regions, however, the loss of low p_T particles will affect the flow measurements.

The p_T acceptance could be corrected for as well by fitting the p_T distribution with the well-known exponential curve, and this has been done in calorimeter experiments that have particularly limited acceptance [Ahle98], but was not done for this thesis due to time constraints.

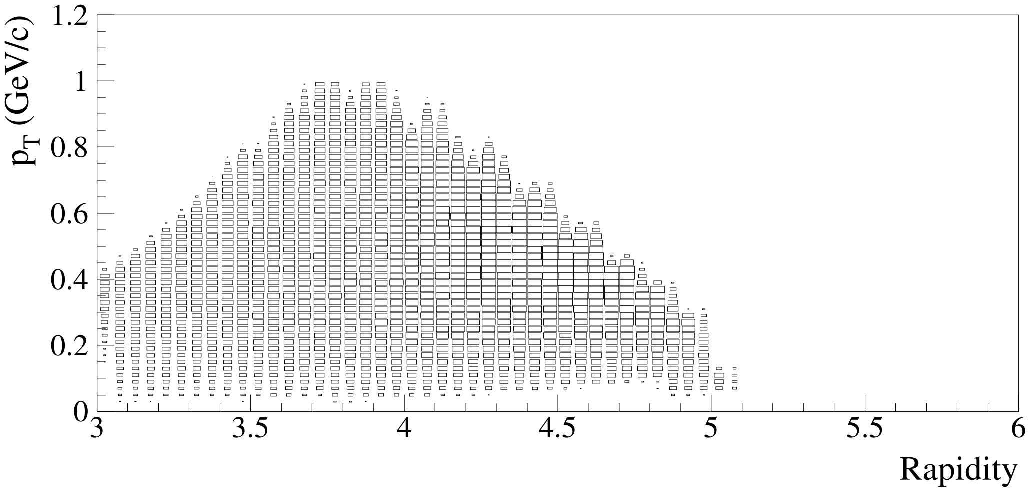

Figure 5.10: p_T vs. rapidity distribution of protons in the main TPCs with cuts for complete ϕ coverage in all p_T ranges. This selection of particles was used for the acceptance correction-weighted flow measurements.

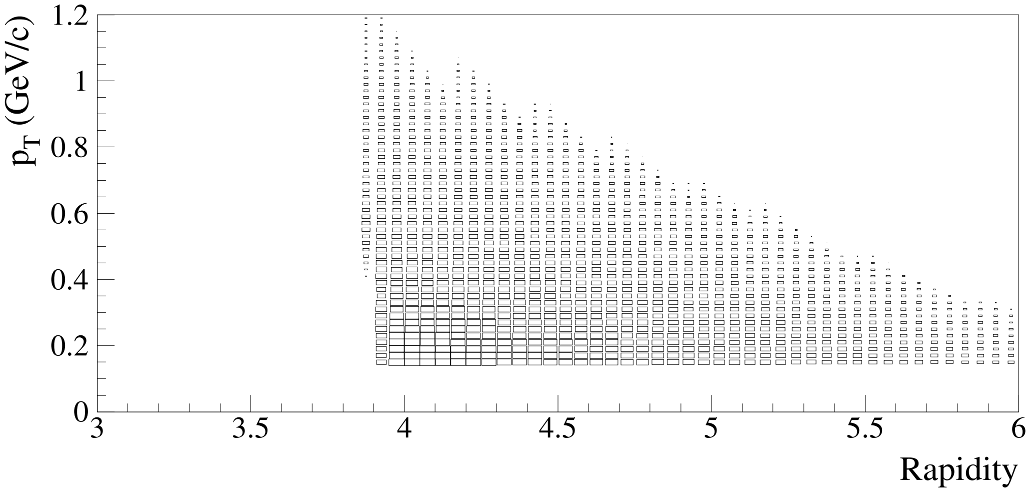

Figure 5.11: p_T vs. rapidity distribution of pions in the main TPCs with cuts for complete ϕ coverage in all p_T ranges. This selection of particles was used for the event plane determination as well as the acceptance correction-weighted flow measurements.

Chapter 6

Results

6.1 Event Selection

The events used in this thesis were medium-bias events selected via the veto calorimeter, as described in section 2.3. However, some contamination of unwanted events is always present in any trigger, and this one was no exception.

Figure 6.1 shows total multiplicity in Vertex TPC 2 plotted against total multiplicity in the right Main TPC (positive particles). It is obvious that the most likely event values fall along a diagonal line with the bulk of the events near the point $N_{VTPC2} \simeq 400$, $N_{MTR} \simeq 225$. It is also obvious that at least one other event subclass exists: the cluster of events that fall at low multiplicity (~ 100) in VTPC2. Note also the spread of events with higher multiplicities in VTPC2 above the most likely values.

Most of the particles that pass through VTPC2 also pass through the MTPCs, creating the correlation seen in figure 6.1. If a collision occurs anywhere other than the target, however, this correlation is changed. The events with low VTPC2 multiplicity probably occur from a collision inside the VTPC2 detector.

To remove unwanted events, a simple cut is made:

$$N_{MTR} > 160$$

$$1.75 \cdot N_{MTR} - 100 < N_{VTPC2} < 1.75 \cdot N_{MTR} + 100$$

These cuts are displayed in figure 6.1. This cut drops the total number of events available for analysis down to about 45,000.

6.2 Track Selection

A number of cuts were applied to the tracks in each event to ensure that only reasonable tracks were used for analysis. Three requirements were used for a track to be valid for analysis:

- It must be long enough to have a large number of clusters to ensure a good average dE/dx. A minimum of 50 clusters per track (out of 90 maximum) was required.
- It must have a reasonable value of dE/dx (doubled tracks are fairly common in the high-resolution sectors of the MTPCs). Values of dE/dx were required to be between 250 and 650 ADC counts.
- The particle's lab momentum must be between 2.7 and 150 GeV to be valid for the particle identification routine.

6.3 Event Plane Evaluation

The event plane uncertainties must be well understood for a good analysis of flow values. Acceptance biases must be removed and corrections must be made to the flow values for the uncertainty in actually determining the plane. These results are discussed next.

6.3.1 Event Plane Calculation

The event plane was found using the Danielewicz and Odyniec method as described in section 4.2.1. The one notable difference was that pions were used instead of protons. The ratio of pions to protons at SPS energies is on the order of $10 : 1$, so many more pions are available per event for event by event calculations. In addition,

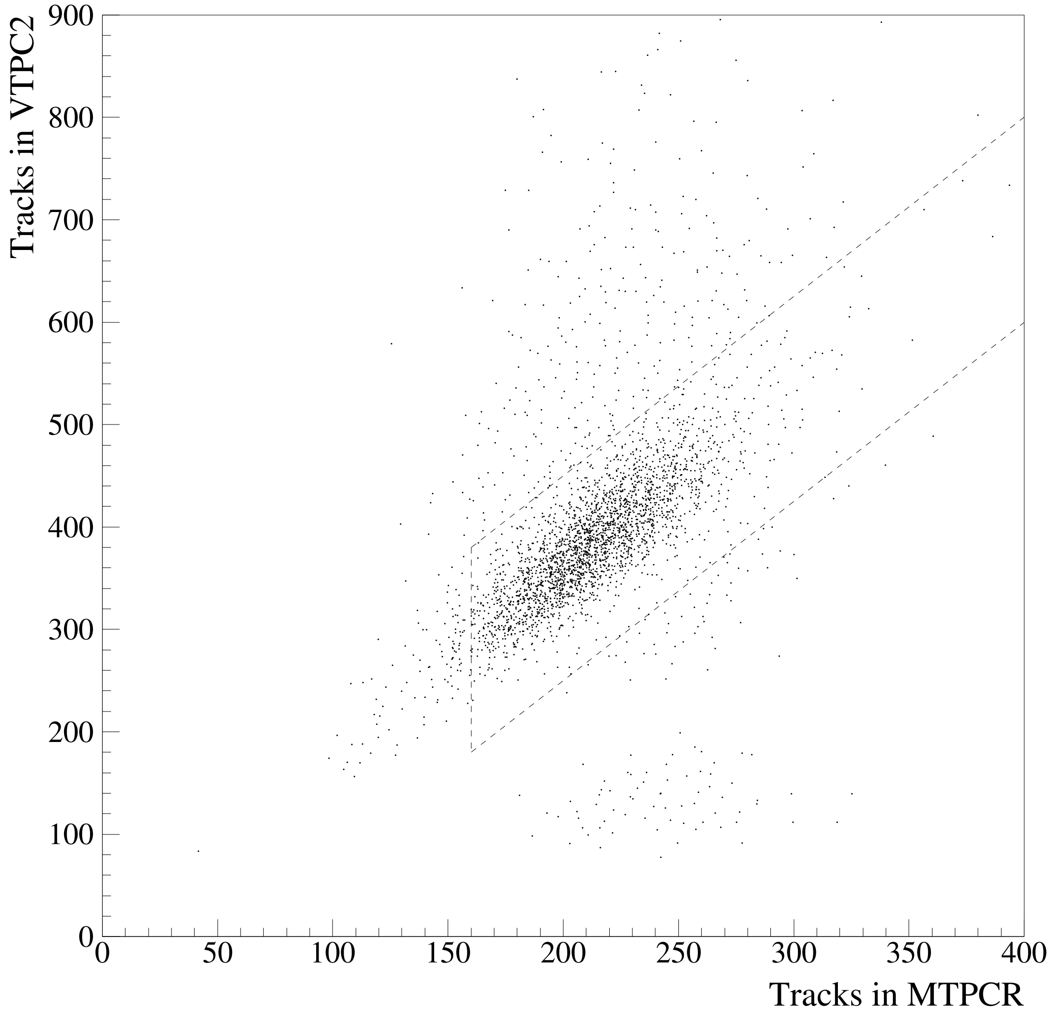

Figure 6.1: Event multiplicity distribution of VTPC2 plotted against MTPCR with cuts for "good" events.

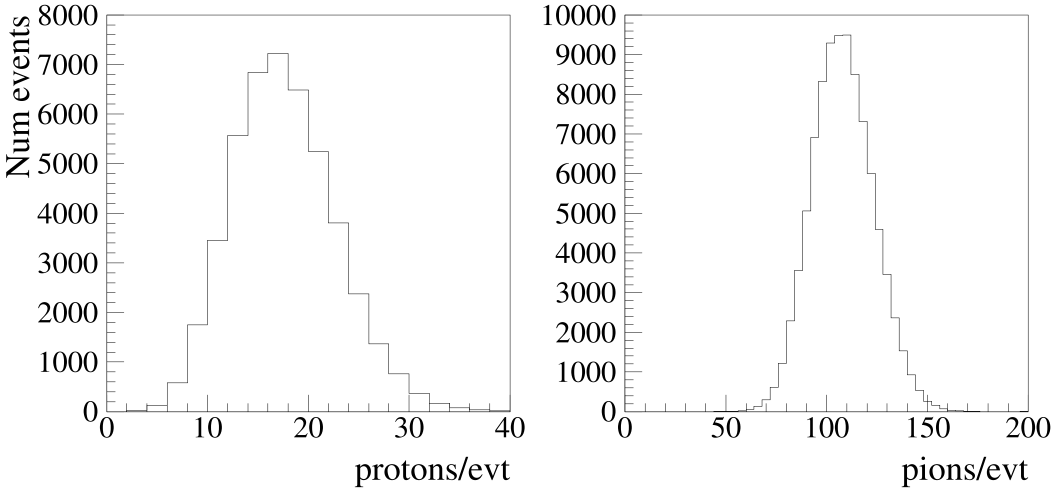

Figure 6.2: Protons and pions identified per event for the medium-bias data.

the requirements for clean dE/dx particle identification (see section 3.6) reduced the number of identified particles to mean values of ~ 17 protons and ~ 108 pions per event. The distribution of particles per event for the medium-bias data can be seen in figure 6.2.

Both positive and negative pions were used in the final event plane. Using negative pions only for the event plane calculation to avoid contamination by protons was also studied, but the statistical improvements of including all pions made the event plane resolution correction smaller. The cuts on momentum and θ described in section 5.4 are also used to avoid any gaps in ϕ coverage that cannot be corrected.

The distribution of event planes with respect to the lab frame should be flat due to the random distribution of the azimuthal orientation of collision impact parameters in ϕ. This distribution is shown in figure 5.7 after the acceptance correction discussed in chapter 5 has been applied, and is a significant improvement over the uncorrected distribution seen in figure 5.5. The results are summarized in table 6.1.

Term		Magnitude
Before:	$\cos(\phi)$	13.88 %
	$\cos(2\phi)$	1.33 %
After:	$\cos(\phi)$	0.051 %
	$\cos(2\phi)$	0.234 %

Table 6.1: Results of acceptance correction on event plane distribution. In the ideal case both terms would be 0%.

Parameter	Value
χ	0.439
C_F	2.693

Table 6.2: Correction values for flow due to event plane resolution.

6.3.2 Event Plane Resolution

As described in section 4.2.3, the resolution of the event plane determination can be evaluated by splitting each event into two random subevents and examining the correlation between them. This correlation can then be used to determine a correction factor for the flow values measured via equation 4.4.

For each event, the pions were randomly divided into two subevents. The event plane azimuthal angle, Φ, was calculated separately for each subevent, subtracted, and plotted in figure 6.3. The value of χ as determined from equation 4.4 as well as the correction factor required for the flow measurements are listed in table 6.2.

This value compares favorably to the value found for NA49 in [Appe98] of $C_F = 2.857$. The present slight improvement is most likely due to either the multidimensional acceptance correction ([Appe98] corrects for acceptance in ϕ only), improved particle identification, and/or improved selection of particles for the event plane calculation.

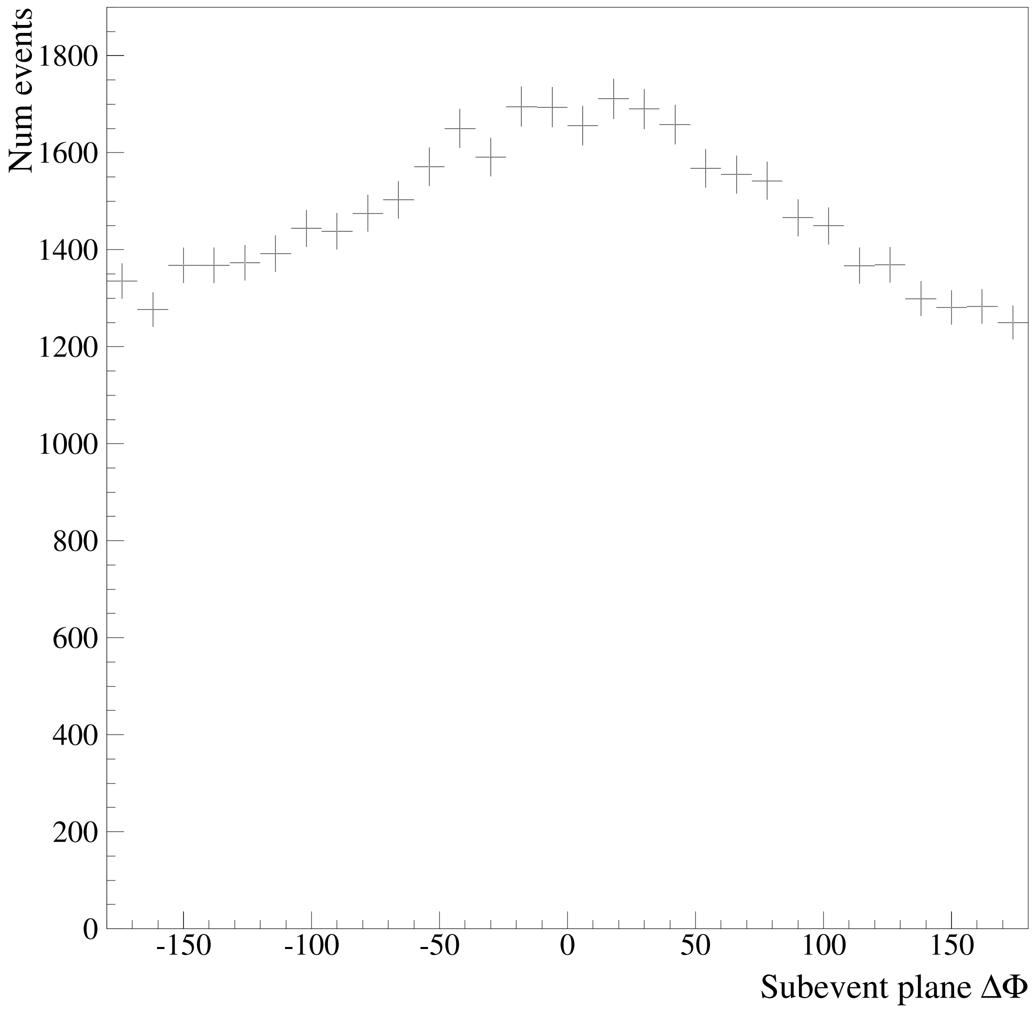

Figure 6.3: Correlation between subevents for pion event plane. This corresponds to a flow correction factor of 2.693.

Cut	**Protons**	**Pions**
rapidity	3.0 - 5.5	3.5 - 6.0
p (GeV/c)	0 - 75	0 - 75
p_T (GeV/c)	0.0 - 1.0	0.14 - 2.0

Table 6.3: Cuts used for flow measurements.

6.4 Transverse Flow Results

Both number and p_T-weighted flow were measured for protons and both signs of pions for the following two subsets of particles:

- all particles identified,
- particles that fall within the cuts in table 6.3 and are weighted by the acceptance correction.

In the first case, the mean flow for all particles in the run was measured, while in the second case the mean particle flow per event was measured. Measuring flow event by event will be important when a quark-gluon plasma is formed, since the amount of plasma created is expected to fluctuate from event to event.

For flow to be measured when the acceptance correction weighting method is used, care must be taken to avoid regions of p_T where there is incomplete ϕ coverage, just as when then event plane was found. To this end, cuts were applied to the particles as listed in table 6.3. In addition, the cuts on θ as described in section 5.4 were also applied when flow was weighted by the acceptance correction.

All flow results are plotted against normalized rapidity:

$$y_N = (y - y_{CM})/y_{CM}$$

6.4.1 Number Flow

As mentioned in chapter 4, number flow directly measures $<\cos(\phi)>$. It is becoming a more common transverse flow measurement as beam energies increase and 4π detectors become more difficult to build.

The difficulty inherent in measuring small flow values can be seen from figures 6.4 and 6.5. In figure 6.4, the distribution of number flow measured in each event with respect to rapidity is shown. The overall number flow is simply the mean of each rapidity bin. It can be seen that the number flow measured is a small deviation in a large spread of values. In figure 6.5, the number of tracks per event is shown, also as a function of rapidity. The low number of particles per event in the lowest and highest rapidity bins makes the event by event flow values more uncertain. This should be taken into account when the event by event flow plots (those weighted by the acceptance correction) are examined next.

The proton number flow results can be seen in figures 6.6 and 6.7. The uncorrected flow looks like what would be expected from lower-energy experiments, although with a much smaller magnitude. The flow weighted by the acceptance correction is more problematic – the increase of flow near midrapidity is not expected. Note however that similar problems occur to some degree in the upcoming pion flow results, and that the rapidity bins near midrapidity have the worst acceptance problems (see Appendix A).

The effect of the acceptance correction is less in the pion flow, and it actually appears to improve the results in figures 6.8 and 6.9. The negative pions were seen throughout this analysis to have greater problems at lower rapidities, as can be seen in figures 6.10 and 6.11. The turn-up of the negative pion curve as it approaches midrapidity is still clearly present in the two lowest bins, but the curve at higher rapidities has gone up.

The actual form of these curves is actually still unknown at SPS energies. It appears that the "S-shaped" curves seen at lower energies may no longer be valid at this beam energy. In fact, a flattening of the flow distribution near midrapidity is hinted at in all particle types shown here. An example fit of the third-order polynomial

$$y = a_0 + a_1 x + a_2 x^2 + a_3 x^3$$

to the acceptance correction-weighted positive pions is shown in figure 6.12. Note that the terms a_0 and a_2 are forced to zero due to symmetry. The theoretical results presented later also seem to show this trend away from the "S-shaped" curve.

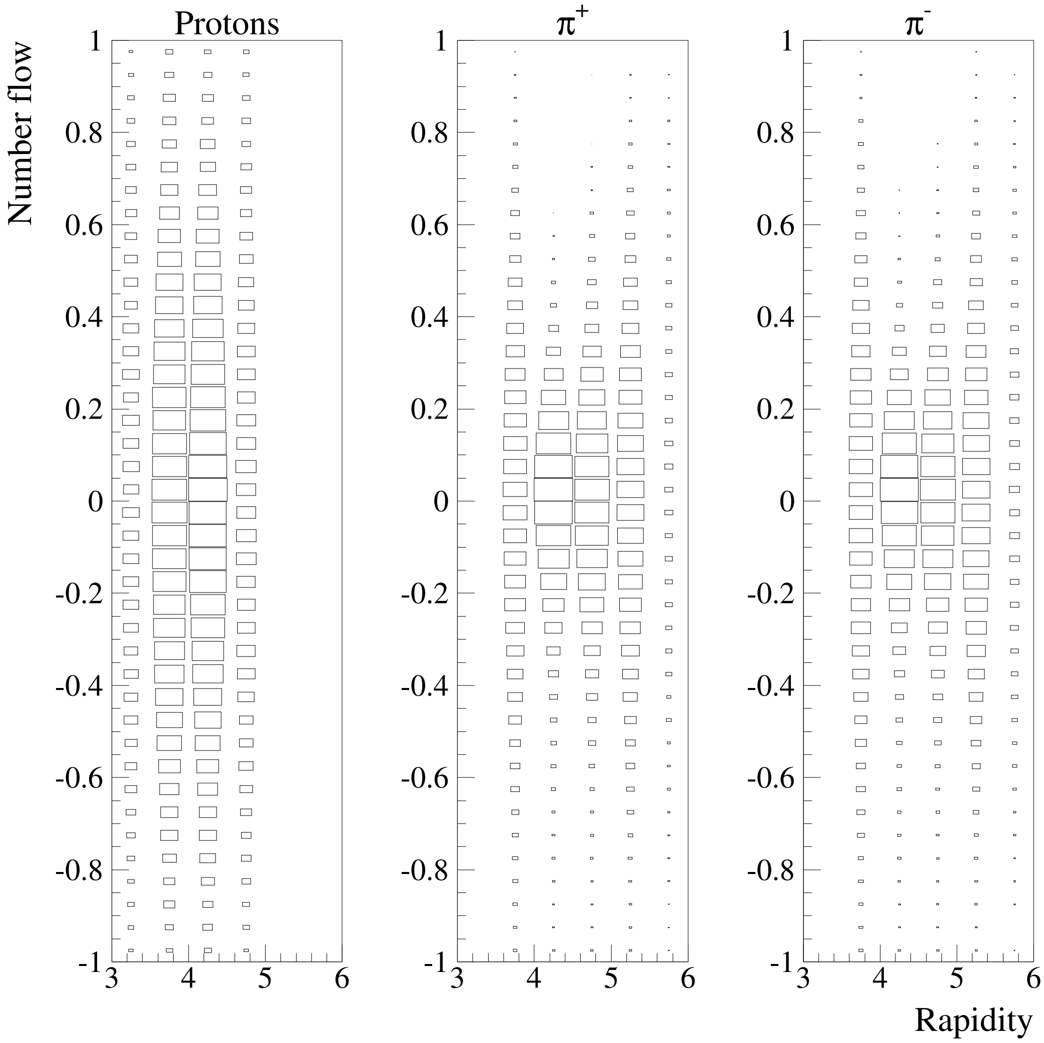

Figure 6.4: Spread in number flow for all particles, weighted with the acceptance correction. The actual number flow measurements are the mean values in each of the rapidity bins.

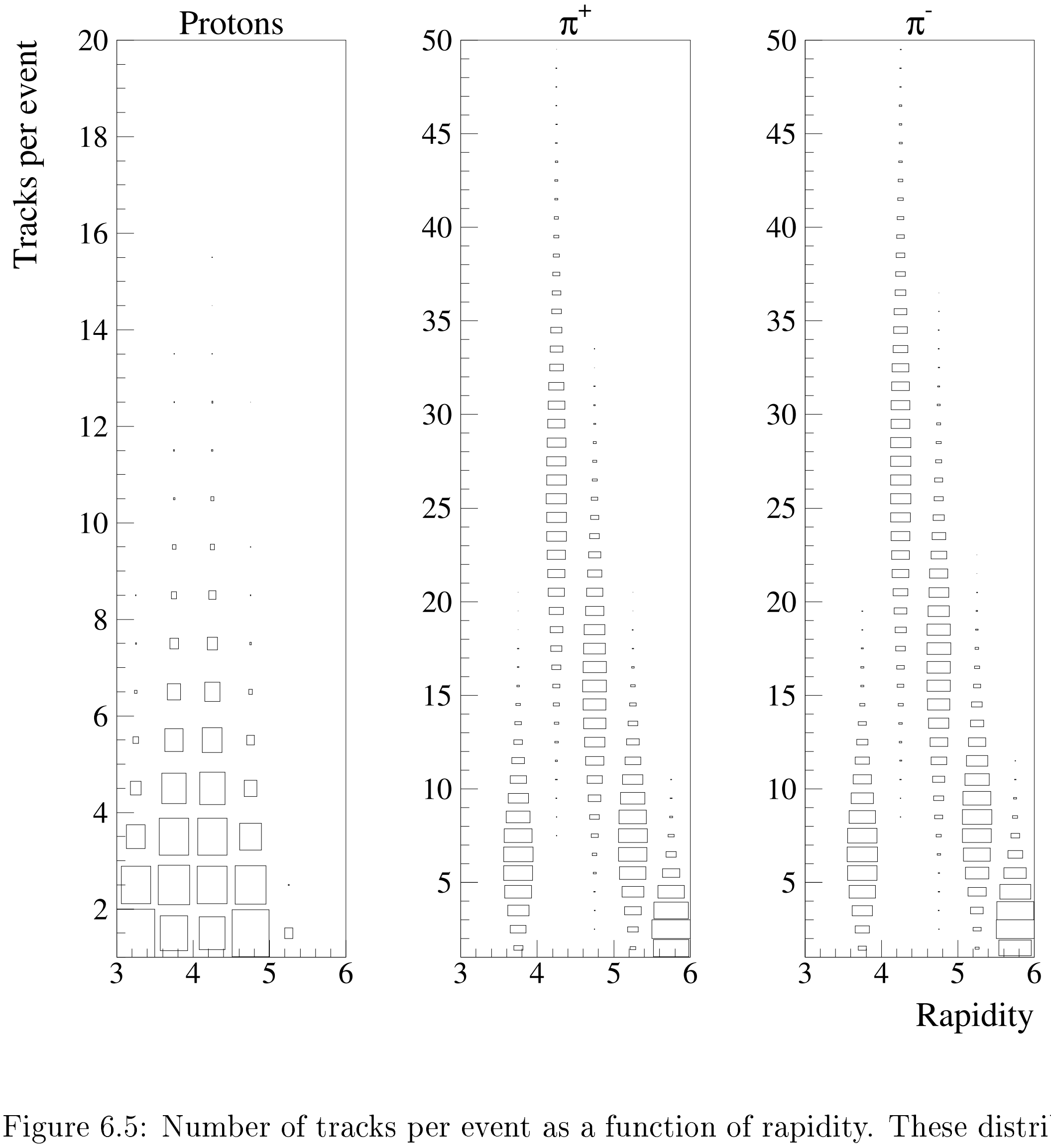

Figure 6.5: Number of tracks per event as a function of rapidity. These distributions reflect the acceptance of the detector as a function of rapidity. The low number of particles in the lowest rapidity bins in particular makes the event by event flow values measured there more uncertain.

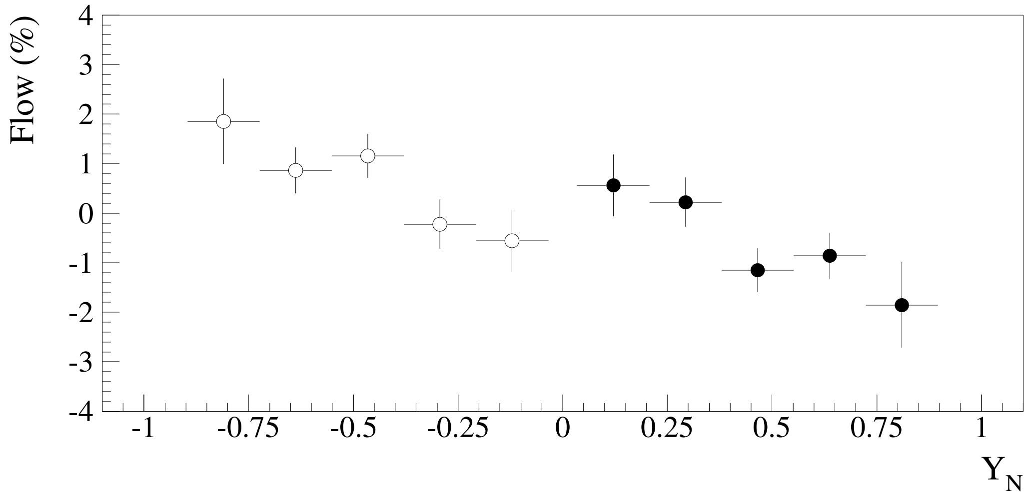

Figure 6.6: Number flow of all protons, unweighted. Open points are reflected about y_{CM} and inverted.

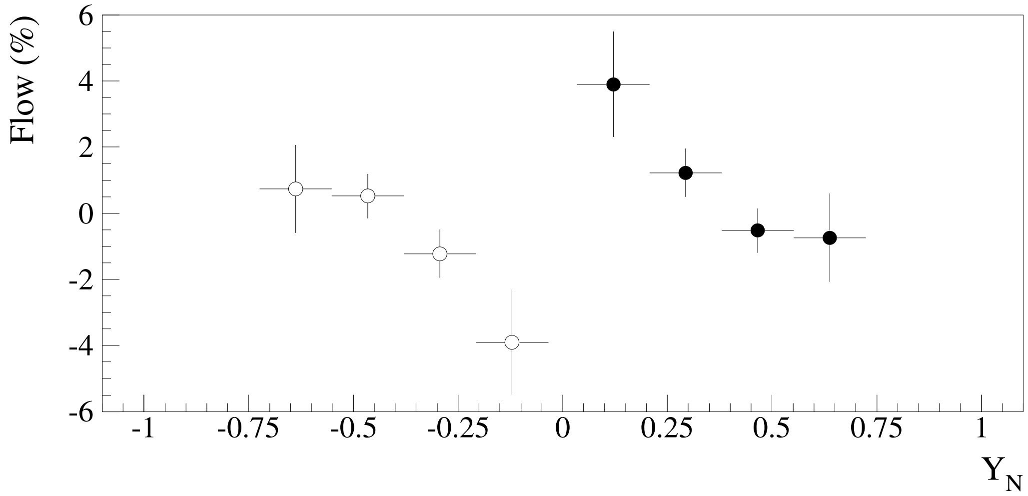

Figure 6.7: Number flow of protons, weighted by the acceptance correction. Open points are reflected about y_{CM} and inverted.

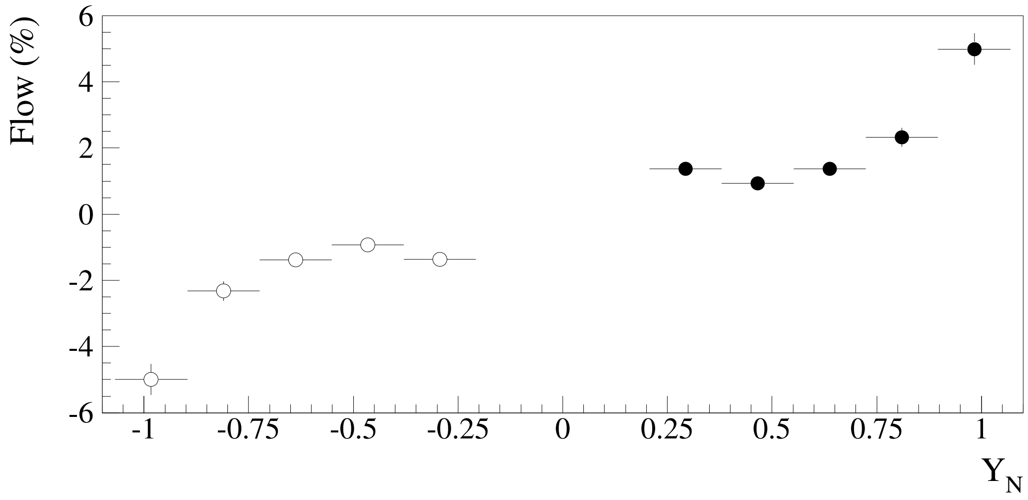

Figure 6.8: Number flow of all π^+, unweighted. Open points are reflected about y_{CM} and inverted.

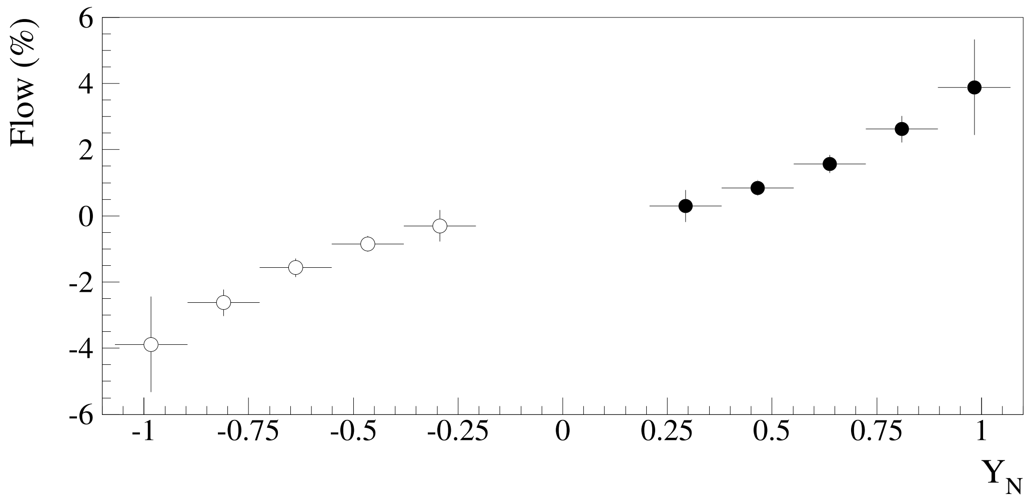

Figure 6.9: Number flow of π^+, weighted by the acceptance correction. Open points are reflected about y_{CM} and inverted.

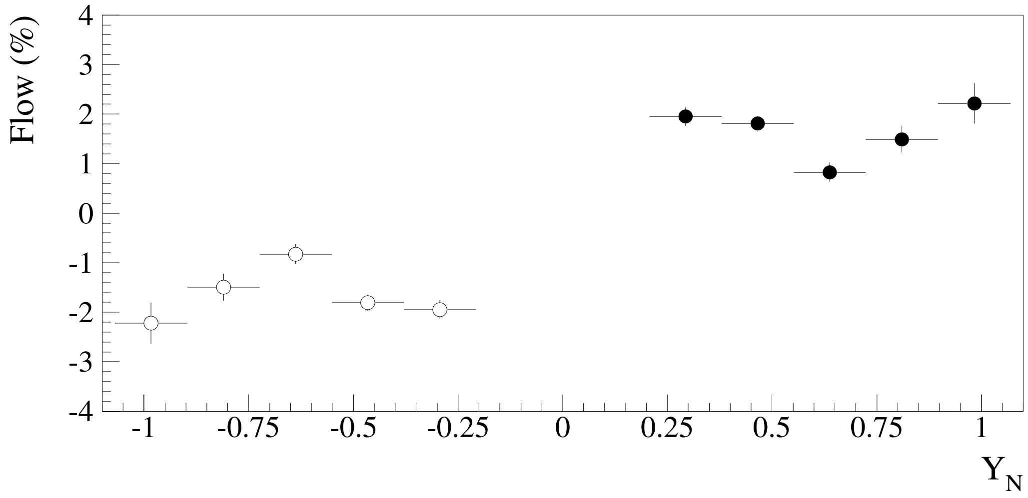

Figure 6.10: Number flow of all π^-, unweighted. Open points are reflected about y_{CM} and inverted.

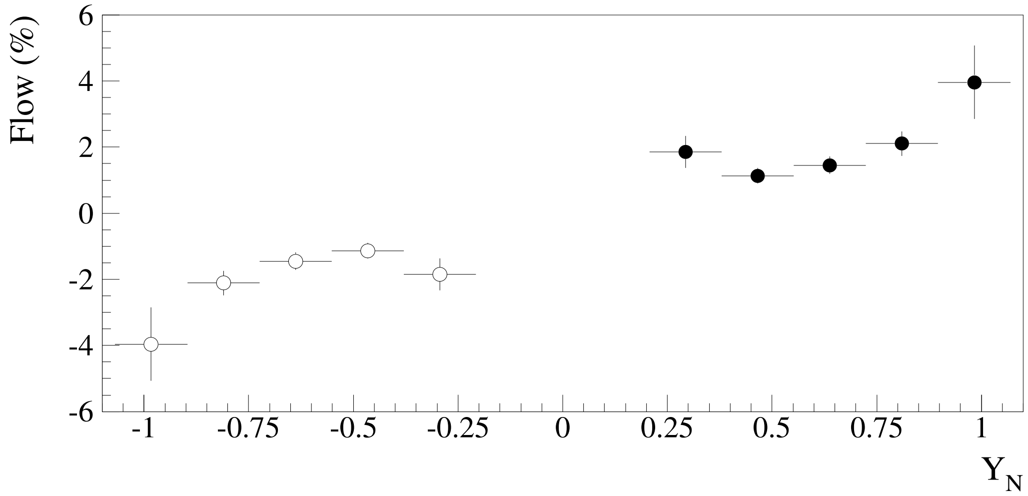

Figure 6.11: Number flow of π^-, weighted by the acceptance correction. Open points are reflected about y_{CM} and inverted.

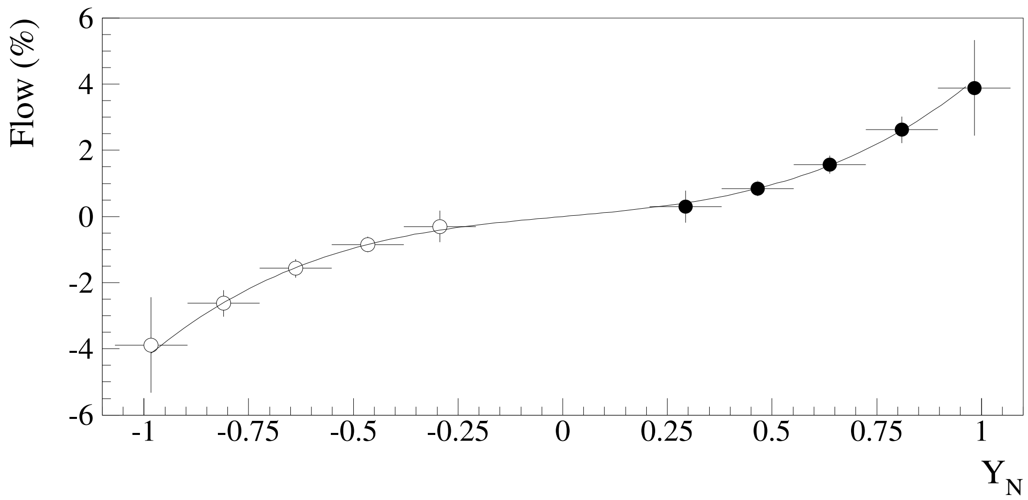

Figure 6.12: Example polynomial fit of π^+ number flow. The data points are identical to figure 6.9.

6.4.2 p_T Flow

The p_T-weighted flow is examined next. For the protons, the shape of the curves does not change significantly, and a straight-line fit the data in figure 6.13 produces a slope of -16.9 ± 2.5 MeV/c.

It should be pointed out that the hole at low p_T for rapidities below 4.25 in the pions will artificially increase the flow measurements in those bins. This effect is clearly seen, especially in the negative pions. Straight-line fits of the acceptance correction-weighted positive and negative pions produce slopes of 8.6 ± 0.7 and 8.2 ± 0.7 MeV/c, respectively.

6.4.3 Comparison With Other NA49 Results

Results for flow at NA49 have been recently published [Appe98]. In this flow measurement, an acceptance correction was made in in ϕ only – no rapidity or p_T dependence was used. The event plane was determined with the pions as in this thesis, and number flow signals were measured for the protons and for all pions. The

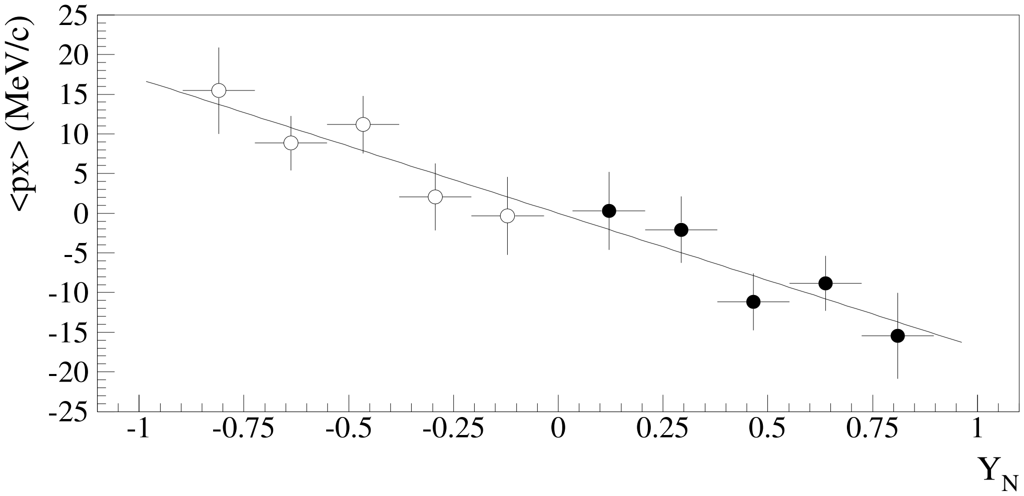

Figure 6.13: $<px>$ of all protons, unweighted. Open points are reflected about y_{CM} and inverted. A straight-line fit of the data produces a slope of -16.9 $\pm$ 2.5 MeV/c.

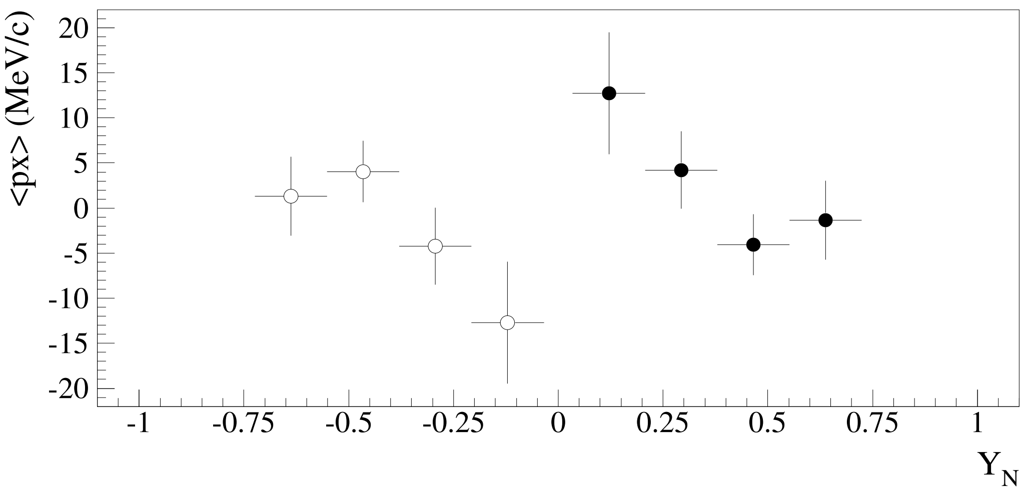

Figure 6.14: $<px>$ flow of protons, weighted by the acceptance correction. Open points are reflected about y_{CM} and inverted.

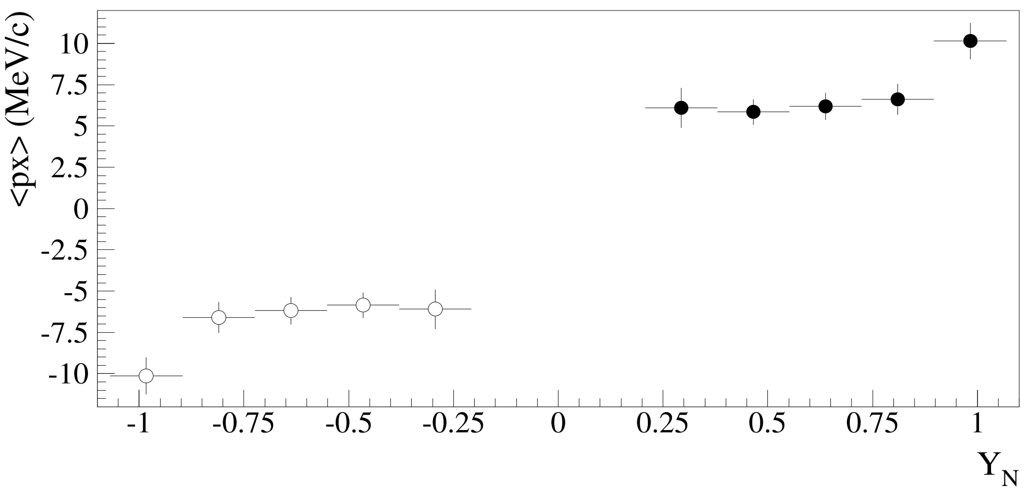

Figure 6.15: <px> of all π^+, unweighted. Open points are reflected about y_{CM} and inverted.

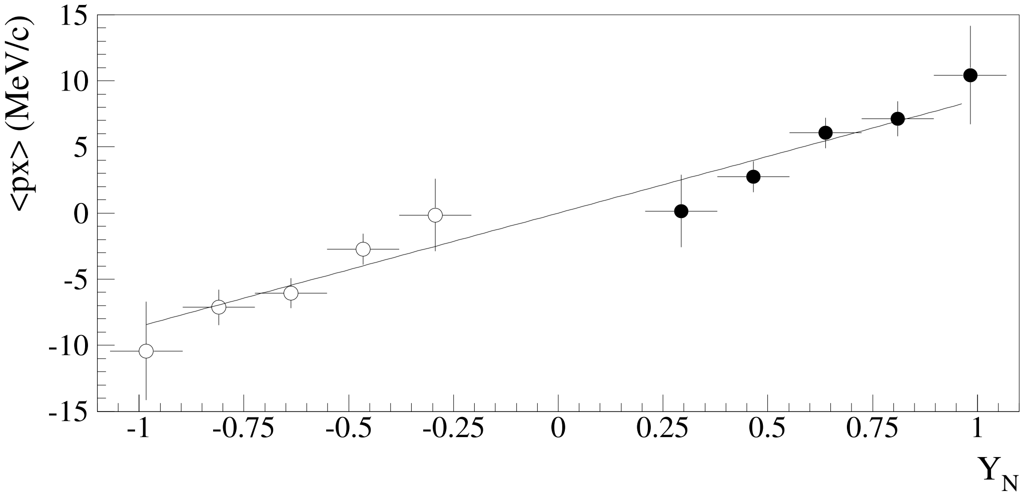

Figure 6.16: <px> flow of π^+, weighted by the acceptance correction. Open points are reflected about y_{CM} and inverted. A straight-line fit of the data produces a slope of 8.6 $\pm$ 0.7 MeV/c.

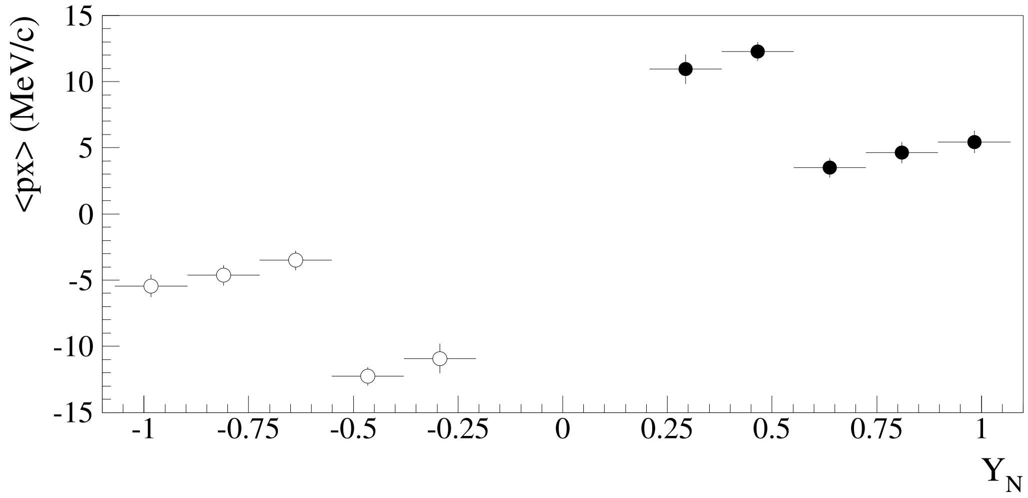

Figure 6.17: $<px>$ of all π^-, unweighted. Open points are reflected about y_{CM} and inverted.

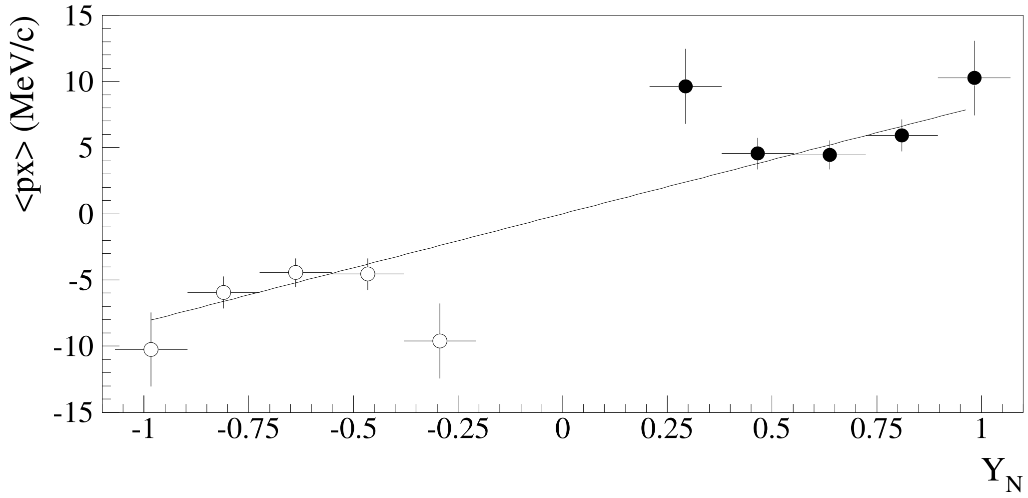

Figure 6.18: $<px>$ flow of π^-, weighted by the acceptance correction. Open points are reflected about y_{CM} and inverted. A straight-line fit of the data produces a slope of 8.2 $\pm$ 0.7 MeV/c.

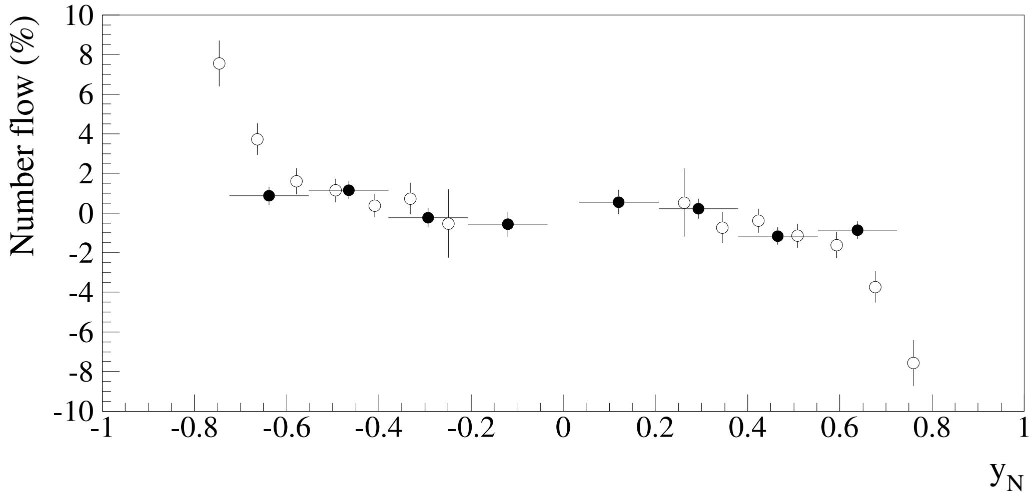

Figure 6.19: Number flow comparison of NA49 proton results. The data from this thesis are plotted in black and the data from [Appe98] are in white. Data points are reflected about y_{CM} and inverted.

comparison between this result and the results of this thesis can be seen in figures 6.19, 6.20, and 6.21.

The protons compare favorably. In the regions near midrapidity, little difference is seen between the two results. The large flow signals at high rapidities were not seen in this thesis, but the particle identification method also differed between the two analyses and very few protons were accepted in that region using the identification method described in chapter 3. It should also be pointed out that the protons from [Appe98] also exhibit a significant third-order polynomial shape.

The pion distributions vary more strongly. The "plateau" regions seen in the earlier analysis are absent from the more recent work for this thesis, and a more linear curve is seen. Unfortunately, positive and negative pions were not measured separately in [Appe98], and that comparison cannot be directly made.

Elliptical flow was examined as well. Although a signal was seen in both the protons and pions, the uncorrected value was quite small (less than 1%) and had significant error (also around 1%). In addition, when 2nd-order flow is measured

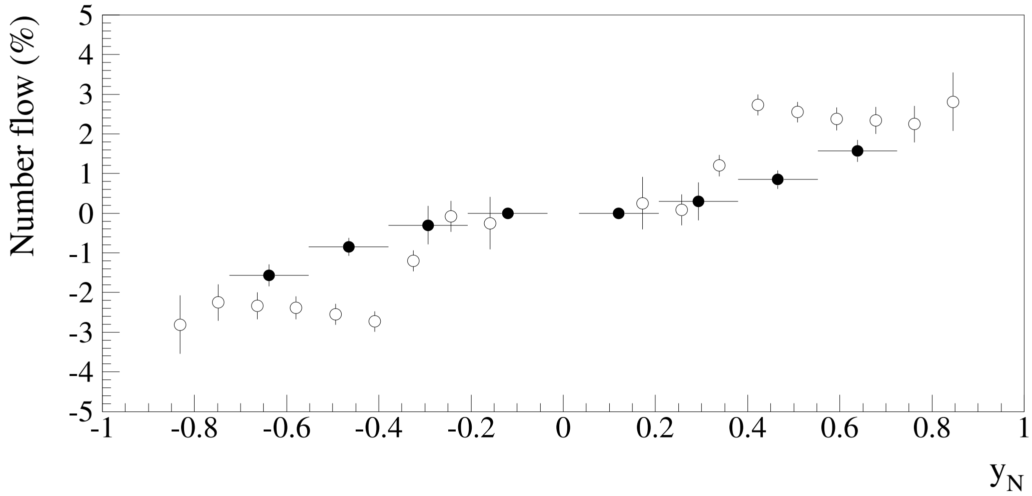

Figure 6.20: Number flow comparison of NA49 positive pion results to earlier flow measurements of all pions. The data from this thesis are plotted in black and the data from [Appe98] are in white. Data points are reflected about y_{CM} and inverted.

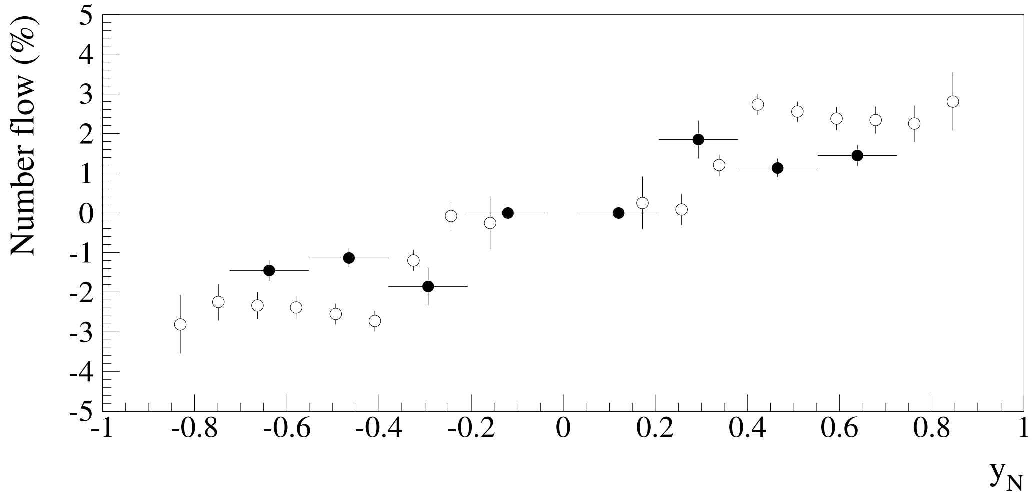

Figure 6.21: Number flow comparison of NA49 negative pion results to earlier flow measurements of all pions. The data from this thesis are plotted in black and the data from [Appe98] are in white. Data points are reflected about y_{CM} and inverted.

using the event plane found from 1st-order flow, as was done here, the event plane resolution correction factor needs to be found using the $n = 2$ curve in figure 4.2 [Posk98]. This provides a correction factor on the order of 20, which while it brings the flow values up significantly also scales the error bars. Overall, the elliptical flow results showed promise, but to provide reasonable errors the event plane needs to be found using the 2nd-order flow, which again allows the use of the $n = 1$ relation in figure 4.2.

Overall, the comparison is favorable. Flow values are similar, and although shapes are not identical the same trends are present in both analyses.

6.4.4 Comparison With Theory

Although transverse flow has been observed for nearly twenty years, theoretical models have been slow to reproduce the effect. Ideal-fluid hydrodynamic models were first used to examine transverse flow, but early results showed no dependence on system size or beam energy, effects that were clearly seen in the laboratory (see [Reis98] for a summary of efforts). The use of semiclassical transport models such as Boltzmann-Uehling-Uhlenbeck, relativistic cascades, and relativistic quantum molecular dynamics improved results, and promising comparisons with AGS-energy data is currently being examined [Kaha97, Ahle98].

At SPS energies, models such as VENUS [Wern87, Wern88] and RQMD [Sorg89] have been used to successfully reproduce many observables, but not transverse flow. VENUS produces no measurable transverse flow, apparently due to the relatively simple nature of the code (it is essentially a mix of some QCD properties and empirical data) [Huan97]. RQMD has been shown to produce some flow when a mean field is included, but minimal flow otherwise [Amel91]. Elliptical flow was examined in [Huan97] in the midrapidity region and the RQMD calculation produced about half the number flow observed in the experiment.

Another model that has been used to examine transverse flow at SPS energies is the quark-gluon string model (QGSM) [Amel89, Amel90]. Like most string models, it uses a quark-parton structure that forms "strings" representing the gluons during collisions. After a certain amount of time, the strings are broken into separate hadrons, each with a certain fraction of the leading hadrons' momenta. This model provides a reasonably good fit to most experimental data over a wide range of beam energies, but has only recently been used to examine transverse flow.

Figure 6.22 shows the QGSM model transverse flow measurement for protons superimposed with the proton flow results from this thesis. As can be seen, the QGSM model predicts much more transverse flow. It should be pointed out that the transverse flow effect present in the QGSM model is due only to the rescattering of secondaries in the model [Amel91]; when the rescattering is turned off no clear flow signal is seen. Also, the impact parameters are different for the model and the data (4 fm as compared to 7.7 fm); although impact parameter dependence of transverse flow has not been studied at SPS energies, lower-energy studies suggest that this could reduce the flow in the data by a factor of two [Reis96, Kint97].

A three-dimensional, relativistic, one-fluid hydrodynamic model was also examined in [Stau89, Amel91] in two versions: one which included a first-order phase transition from normal hadronic matter to a quark-gluon plasma (T_c = 216 MeV), and one with no phase transition. The predictions for an impact parameter of 4 fm can be seen in figure 6.23. As can be seen, the hydrodynamic models overpredict the flow signal even more than the QGSM model. The slopes of the transverse flow distributions (F as described in section 4.2.2) are provided in table 6.4.4. Note that several values of F are quoted for each model; a nonlinear shape is clearly apparent in the models so separate linear fits were made to several regions of rapidity. Error bars are lacking on the hydrodynamic curves due to the continuous nature of fluid models (see [Amel91]).

In both of these model comparisons, the system input to the model was 160 A·GeV Pb + Pb with an impact parameter of 4 fm, while the actual event had a mean impact parameter of $\sim$ 7.7 fm. Data at much lower energies imply maximum transverse flow of protons at an impact parameter of about 4 fm for Au [Reis96], so it could be assumed that transverse flow at larger impact parameters would be less by roughly half. On the other hand, [Huan97] has seen maximum *elliptical* flow around 7-8 fm. Unfortunately, at these energies it is unclear whether transverse and elliptical flow

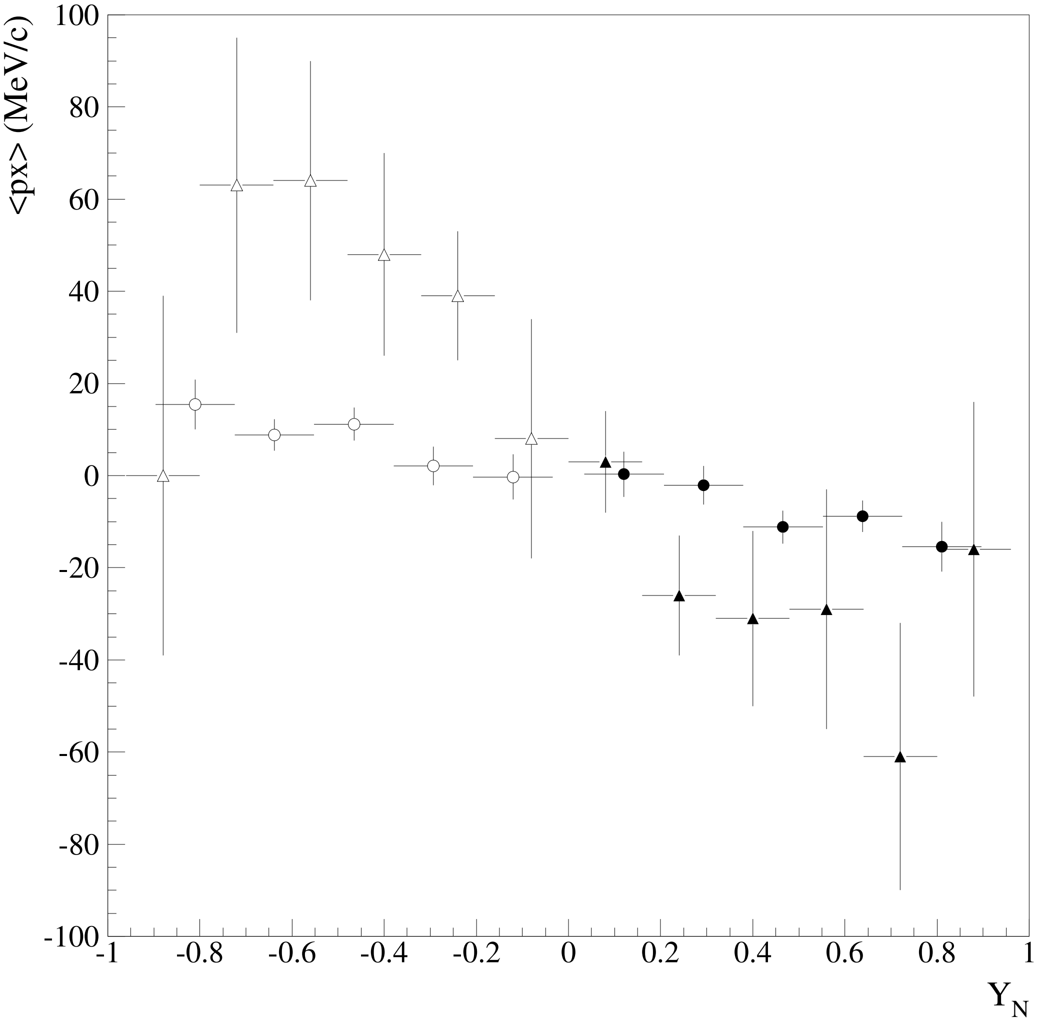

Figure 6.22: Comparison of proton flow results (circles) with QGSM model (triangles) [Amel91]. Note the the model results are for 160 A·GeV Pb + Pb with an impact parameter of 4 fm, while the actual data have a mean impact parameter of $\sim$ 7.7 fm.

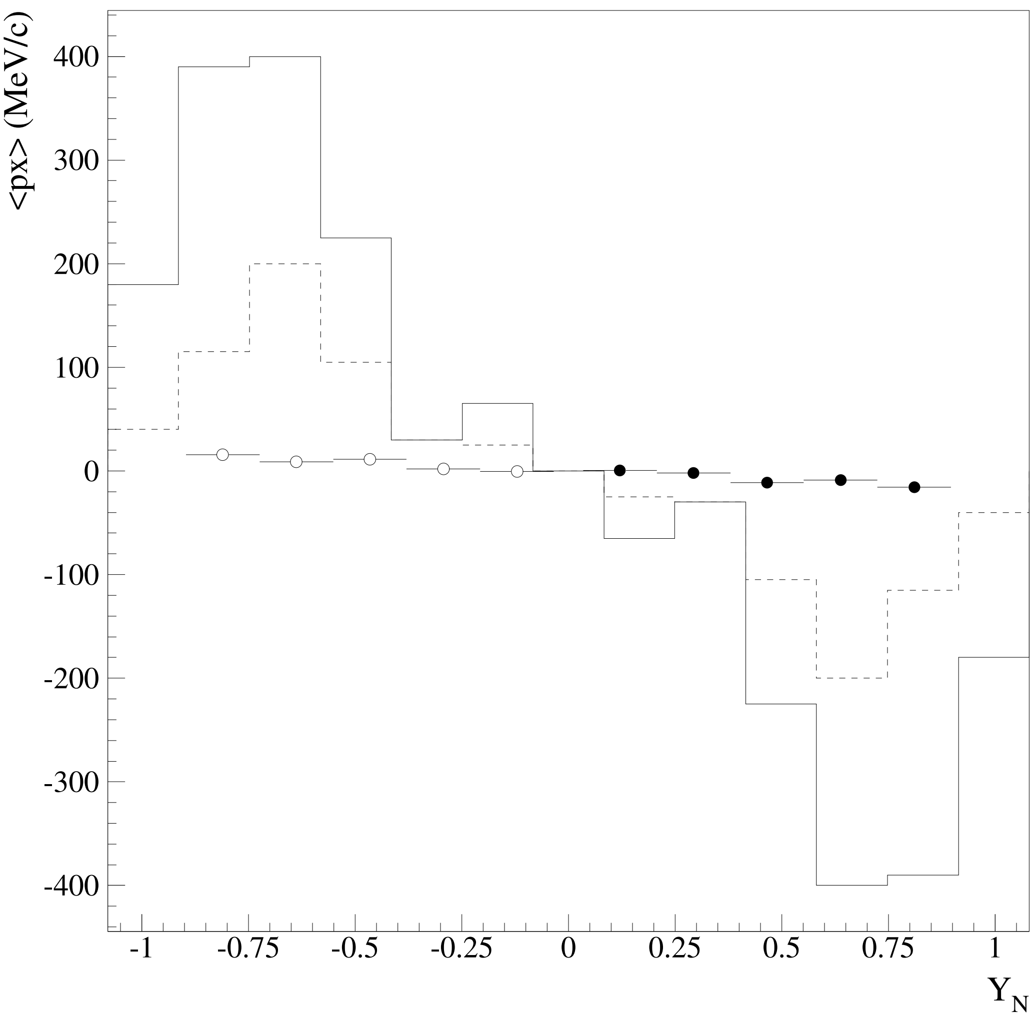

Figure 6.23: Comparison of proton flow results (circles) with hydrodynamic model [Amel91]. The dashed line is the hydrodynamic model with a first-order phase transition to the QGP included; the solid line is the same model without a QGP phase transition. Note the the model results are for 160 A·GeV Pb + Pb with an impact parameter of 4 fm, while the actual data has a mean impact parameter of ~ 7.7 fm.

Source	b (fm)	Fit region	F (MeV/c)
NA49 data shown	7.7	$-1 < y_N < 1$	16.9 ± 2.5
NA49 data shown × 2	(∼ 4)	$-1 < y_N < 1$	33.8 ± 5.0
QGSM	4	$-0.5 < y_N < 0.5$	112.9 ± 26.4
QGSM	4	$-1 < y_N < 1$	74.2 ± 14.6
Hydrodynamic	4	$-1 < y_N < 1$	359.1
Hydrodynamic	4	$-0.4 < y_N < 0.4$	150.5
Hydrodynamic with QGP	4	$-1 < y_N < 1$	133.3
Hydrodynamic with QGP	4	$-0.4 < y_N < 0.4$	102.3

Table 6.4: F values for theory and data. Note that the absolute value of F has been taken for this thesis (see section 6.3.1). At lower energies, F is a maximum near 4 fm and reduces by about half at 8 fm.

will both peak at the same impact parameter. However, it can still be reasonably said that the proton transverse flow measured at NA49 is less than either the QGSM or hydrodynamic model shown here.

6.5 Comparison With Other Energies

A number of other experiments have measured transverse flow at other energies, providing a systematic study of the effect. Transverse flow at energies below 1 GeV/c have been studied by the EOS experiment at the Bevalac [Part95] and the FOPI experiment at GSI [Ritm95, Reis96]. Recent results from AGS energies have been obtained by the E895 [Liu97, Cask98] and E877 experiments [Hemm96, Barr97]. These results are compared to the NA49 results in the following sections.

6.5.1 Proton Flow

The proton p_T-weighted flow at the SPS can be systematically compared to other beam energies. In figure 6.24 are Au + Au data for a variety of experiments. The turnover of transverse flow is clearly seen near 2 A·GeV, and the current E895 [Liu97] and E877 [Barr97] results at the AGS show a clear downward trend at higher beam energies.

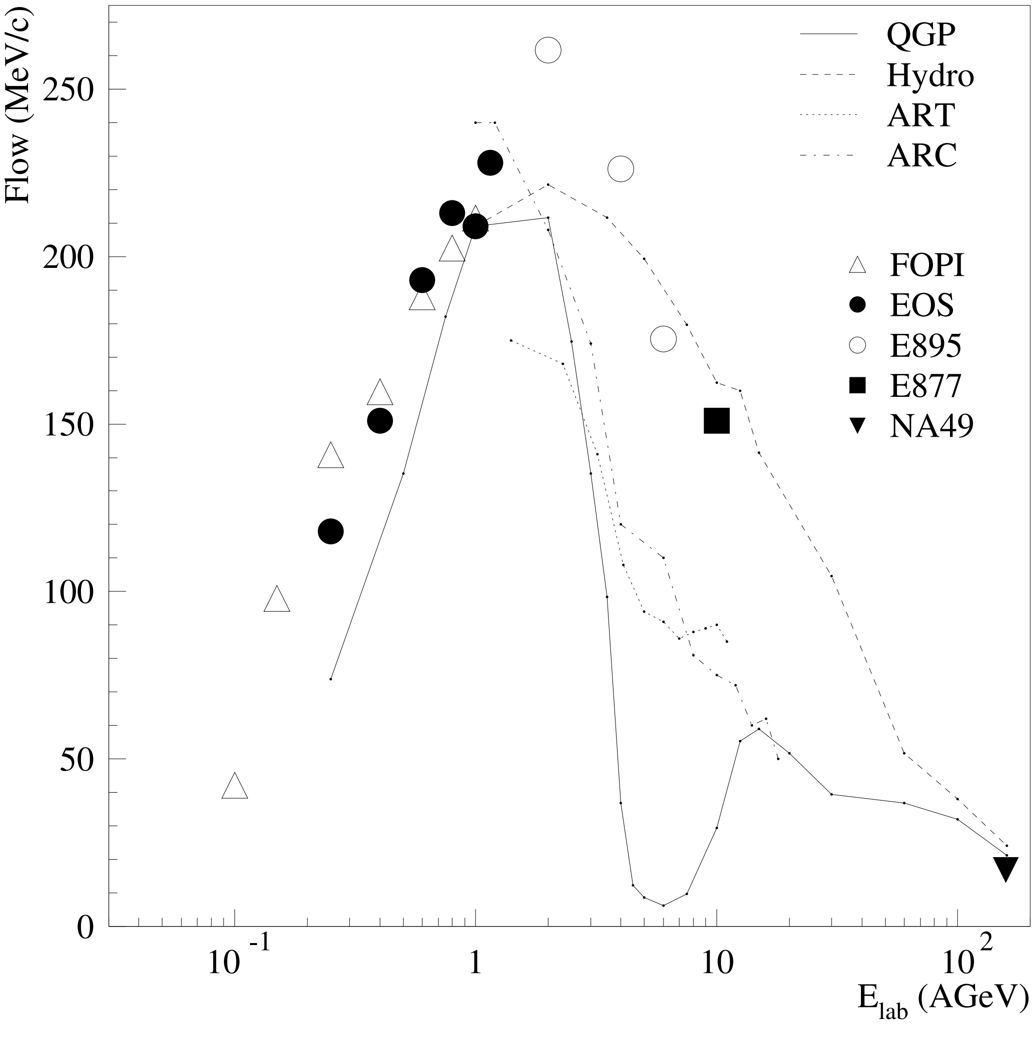

Figure 6.24: Energy dependence of proton transverse flow results. The theoretical curves are described in more detail in the text. EOS data was obtained from [Part95], FOPI data from [Ritm95], E895 data from [Liu97], and E877 data from [Barr97].

The curves plotted in the figure represent several different models, mostly tuned for AGS energies. ARC [Kaha97] is a relativistic cascade model that has proven successful at AGS energies. It is noted for its success in fitting transverse flow measurements without including a mean field. ART stands for "a relativistic transport model" and is essentially the BUU transport model with heavier resonances and their reactions added [Li96].

The curved labeled "Hydro" is a 3+1 dimensional hydrodynamic model [Stau89, Risc96]. The model marked "QGP" is that same hydrodynamic model with a phase transition to a quark-gluon plasma specifically added ($T_c \sim 160$ MeV). The effect of this addition is clearly seen as a dip in the curve at $E_{lab} \sim 6$ A·GeV, caused by the reduction of internal pressure due to the changing equation of state during the phase transition. It has been pointed out, however, that this effect will be lessened if the QGP phase transition is not a first-order transition [Risc96].

6.5.2 Pion Flow

Pion flow has not been studied in great detail in the past, but recent results have shown interesting trends. It is useful to plot pion flow in units of velocity instead of transverse momentum. This allows comparisons with other particle types. Figure 6.25 contains the pion (and proton) flow results for the experiments mentioned above. It should be pointed out that at all these beam energies the pions are seen to antiflow, i.e. flow in the direction opposite the proton flow. The absolute magnitude of the flow signal is actually plotted.

A significant difference in flow between the positive and negative pions was seen at the EOS experiment [Kint97] and this trend has continued at AGS energies [Barr97, Cask98], although the separation between the two gets smaller with increasing beam energy. As was seen earlier in this chapter, there is little difference in transverse flow between the positive and negative pions at SPS energies.

It has been suggested that the difference in flow between positive and negative pions may be due to Coulomb effects with the protons, or that the role of Δ's in pion production and absorbtion have a different effect on negative pions than on positive ones [Kint97]. This result may imply that Δ's have a much reduced role in pion production at SPS energies, but this need to be explored in more detail.

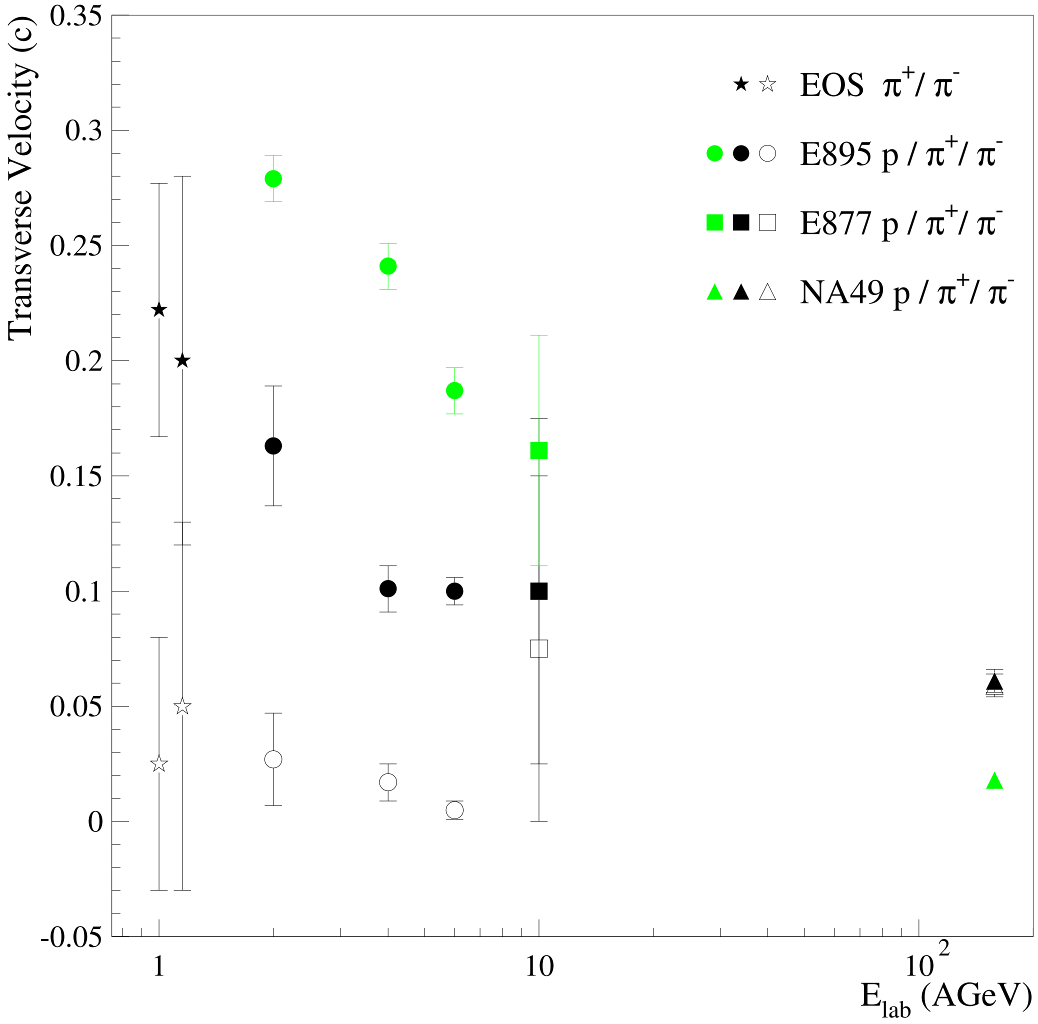

Figure 6.25: Energy dependence of pion (and proton) transverse flow results. EOS data was obtained from [Kint97], E895 data from [Liu97] and [Cask98], and E877 data from [Barr97]. Note that at all these beam energies, the pions and protons actually flow in opposite directions; the absolute magnitude of the flow signal is plotted here.

Chapter 7

Conclusions

7.1 Overview

In this thesis, results on transverse flow in Pb + Pb at 158 A·GeV/c at the CERN SPS have been presented. Particle identification methods have been examined, methods of correcting for significant acceptance bias have been developed and utilized and transverse flow for protons and pions has been measured. Several methods of flow measurement were used and the results compared. Further comparison was made with flow measurements from some of the currently available theoretical models.

The event plane detection at SPS energies has proven to be too difficult to find in the protons, but the abundance of pions with a clear flow signal has made transverse flow analysis still possible, and reasonable event plane resolutions have been seen.

Transverse flow has been measured in various ways. Number flow has been gaining popularity in recent years, and has been seen in this thesis to provide clear flow signals. The more traditional p_T-weighted flow measurement has greater problems at higher beam energies, where building a 4π detector becomes increasingly difficult.

The method of correcting for acceptance biases in event by event transverse flow measurements has been successful. There remain some differences between event by event flow measurements and the run-summing method. These differences are thought to be related to the severity of the acceptance correction and the multiplicity of the particles in that rapidity bin. This method shows distinct promise and should be pursued in the future, especially since event by event flow measurements will be important for studying fluctuations in quark-gluon plasma production.

The measured proton transverse flow was compared to proton flow from other experiments. While not deviating from the trend of decreasing flow above 2 A·GeV, this result does put a new point on the world systematics plot that expands the range being studied. Results from next year's 40 A·GeV run at the CERN SPS should fill in points between the AGS and SPS energies and help determine if any phase transition is occurring in that energy range.

Pion transverse flow was also compared to other experiments. While the magnitude of the flow did not change significantly, the positive and negative pions were seen to have the same flow velocity, something not seen at lower energies. The reason for this has yet to be understood, although Coulomb effects and differing pion absorbtion methods at varying beam energies have been suggested.

Of prime importance is greater physical understanding of the flow signal at high beam energies. Current models are only beginning to reasonably reproduce transverse flow at AGS energies, and flow at SPS energies. Elliptical flow, at least, will definitely be measured at RHIC with data being taken in 1999, and a clear understanding of the physical processes involved at lower beam energies will greatly aid interpretation of RHIC data.

7.2 The Future

As little as two years ago, many people doubted that transverse flow would exist at all at SPS energies, or if it did exist, be large enough to measure. However, recent work including this thesis has shown that not only is measurement possible but that new and exciting results are being obtained.

New methods of measuring flow have been and are still being developed, and recent physical insights into observables like elliptical flow and the possibility of event by event flow measurements have opened opportunities for studying transverse flow at SPS energies and beyond. Transverse flow has been reexamined as a potential signal for the quark-gluon plasma, and will definitely be forefront in the measurements made at RHIC.

Appendix A

Detector acceptance plots

This appendix contains histograms showing the detector acceptance for the various particle types. The size of the box is proportional to the number of counts in the bin, and each plot is renormalized separately so comparisons of box size between plots are not valid. For an idea of the p_T dependence of the particle production, see figures 5.8 and 5.9.

These plots helped provide reasonable locations for p_T cuts as well as an idea of how nonsymmetric the detector acceptance truly is. For more information about how these acceptance biases was corrected for, see chapter 5.

The unusual shapes of the particle acceptances are due to the rectangular shape of the MTPCs. At very low rapidities, only particle that have a large p_T in the direction of the MTPC actually make it into the detector. As rapidity increases, tracks traverse the center of the main TPCs. Tracks that have large values of p_x are aligned with the horizontal spread of the MTPC ($0°$ and $180°$ in these figures) and are accepted even at high p_T, while tracks with large p_y travel outside the top or bottom of the detector. This effect creates the double-hole structure seen in the figures on the next few pages.

As rapidity increases further, the double-hole structure changes into a single hole, aligned with the the horizonal direction lab frame. This is effectively the same effect as at low rapidity, and is due to the inner edge of the MTPC near the beampipe. Tracks with high rapidity are making it into the detector only if then have a large p_T

away from the beampipe.

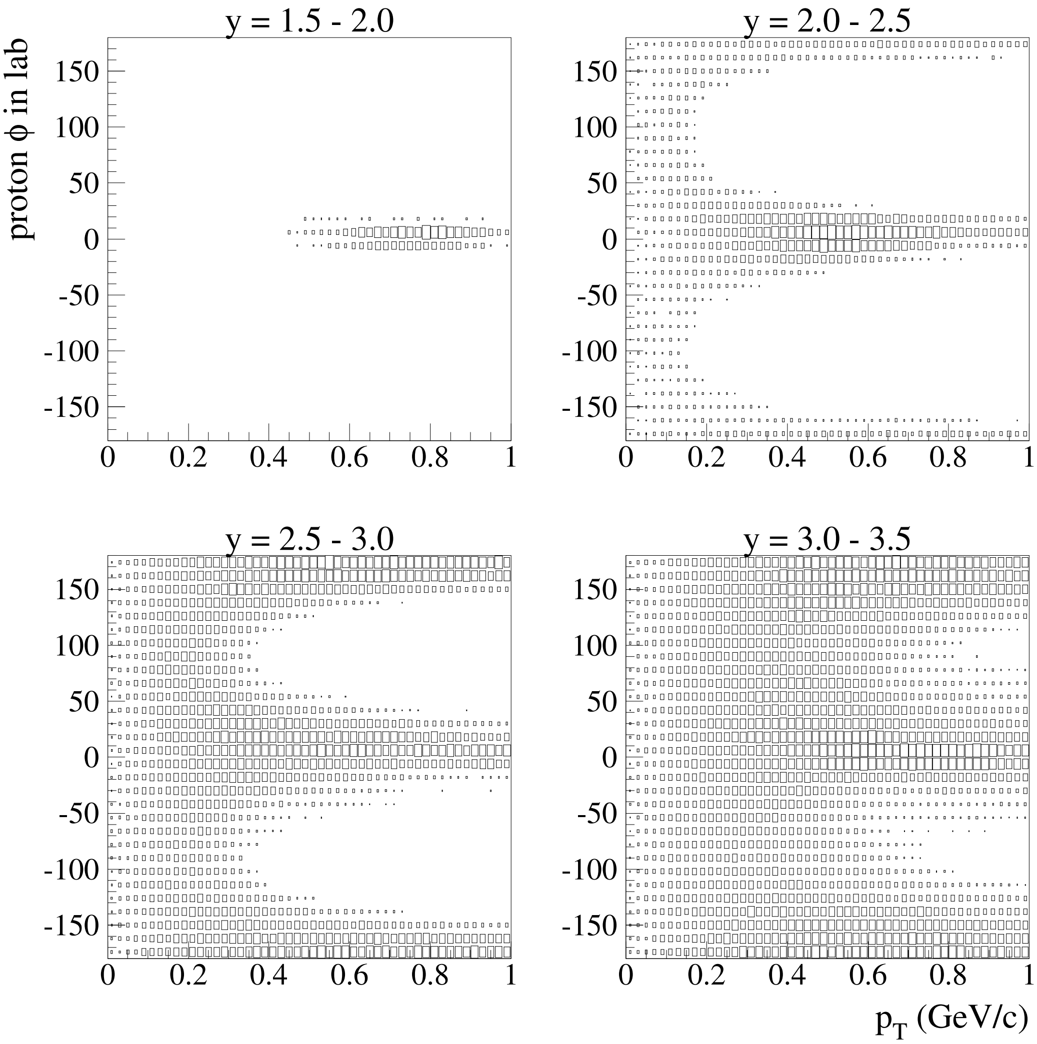

Figure A.1: Protons accepted in the MTPCs for various rapidity ranges (continued in next figure).

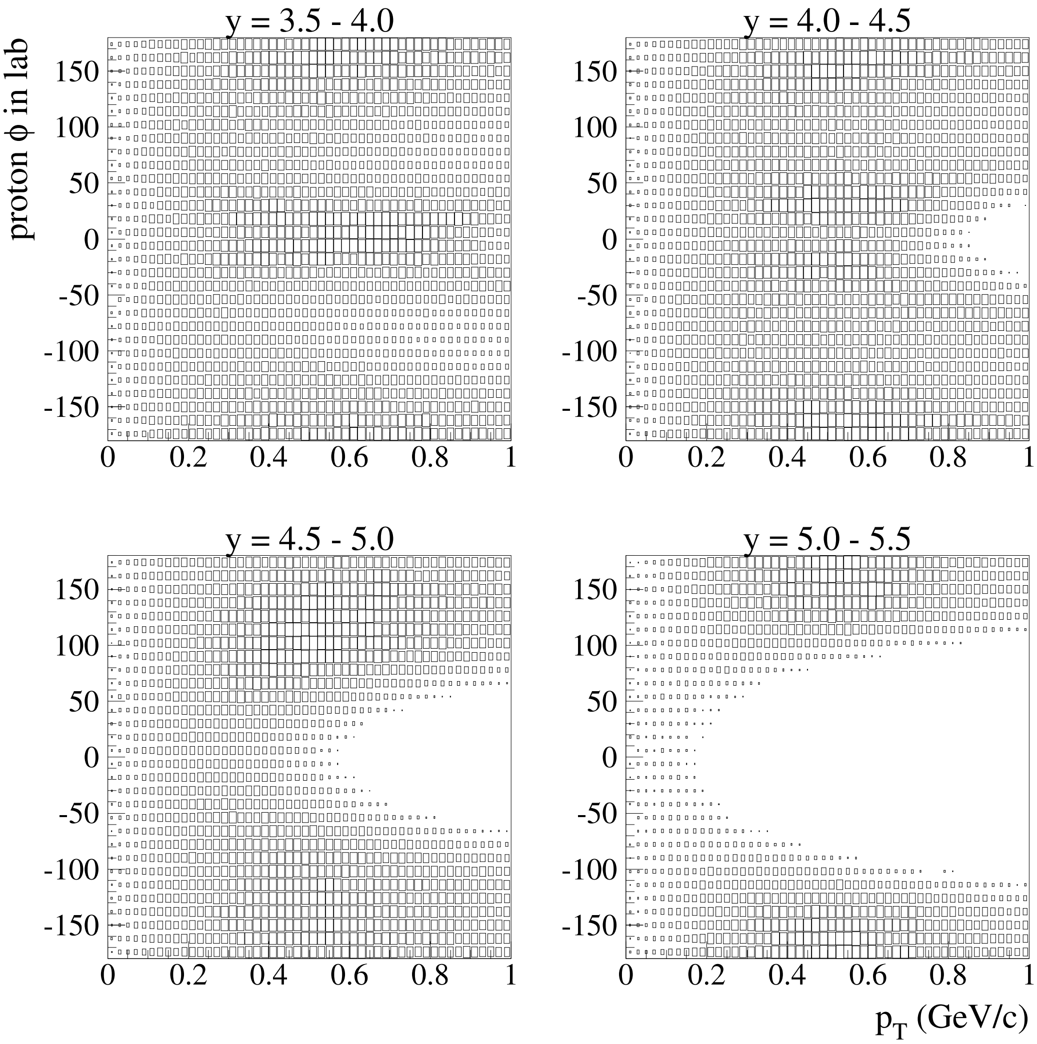

Figure A.2: Protons accepted in the MTPCs for various rapidity ranges (continued from previous figure).

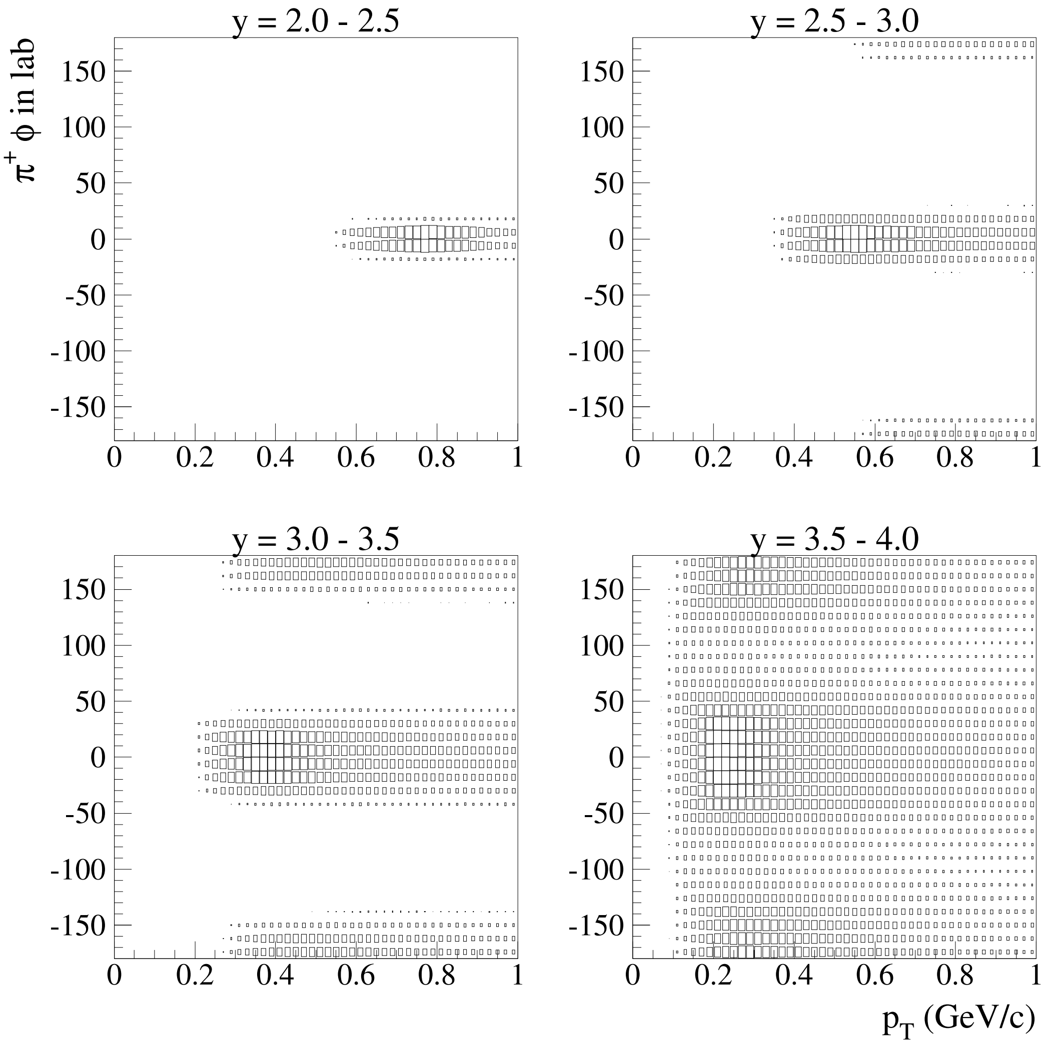

Figure A.3: Positive pions accepted in the MTPCs for various rapidity ranges (continued in next figure).

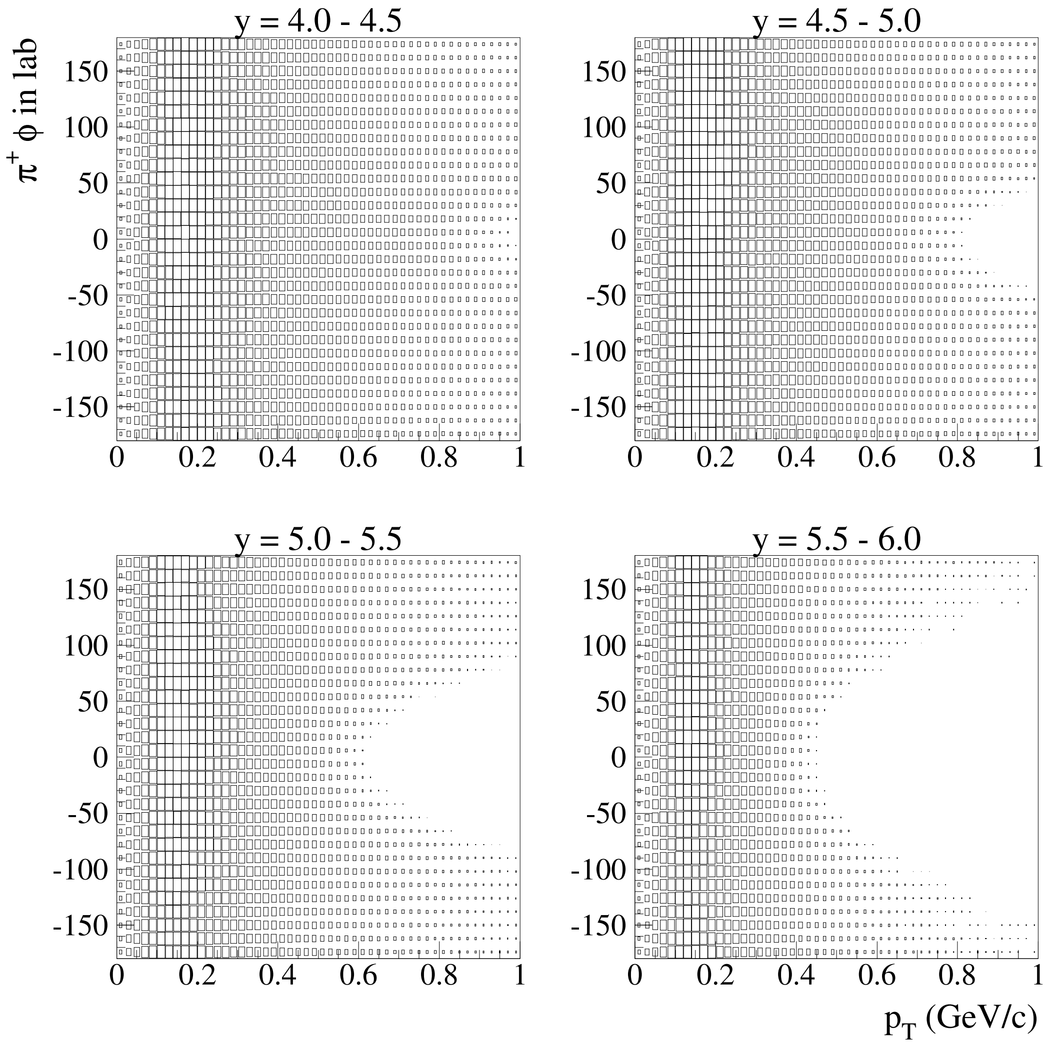

Figure A.4: Positive pions accepted in the MTPCs for various rapidity ranges (continued from previous figure).

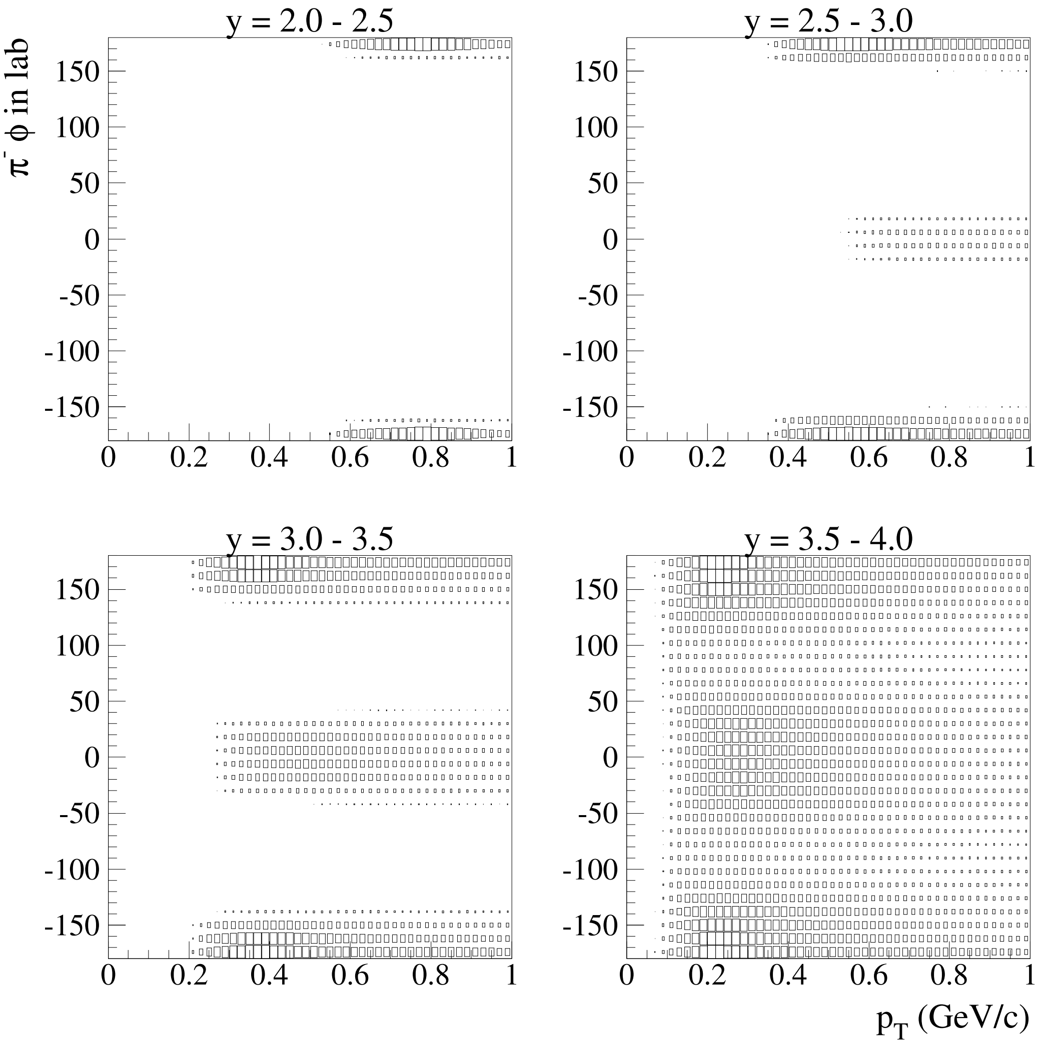

Figure A.5: Negative pions accepted in the MTPCs for various rapidity ranges (continued in next figure).

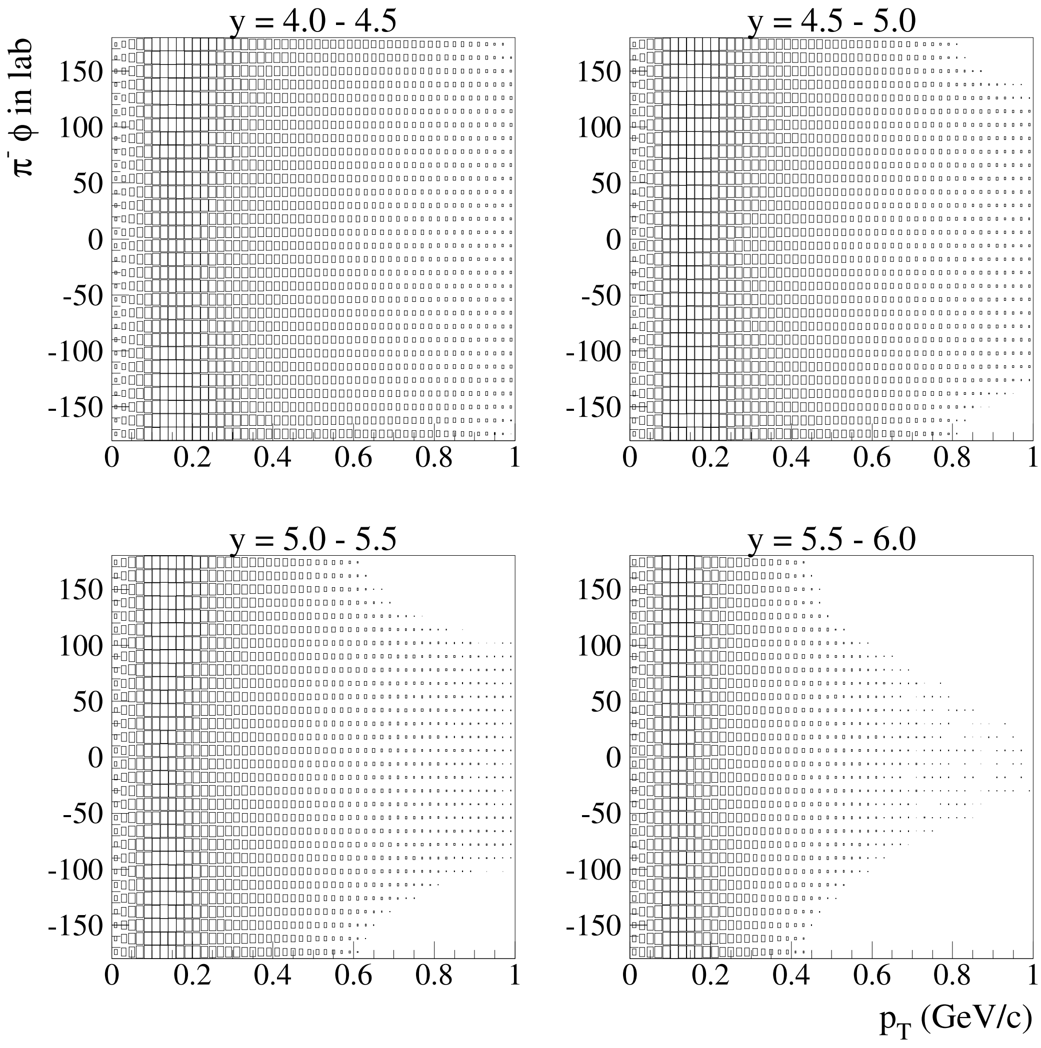

Figure A.6: Negative pions accepted in the MTPCs for various rapidity ranges (continued from previous figure).

Appendix B

Calculation of medium-bias cross section fraction

We can estimate the fraction of the total cross section that the medium-bias trigger selects from the known values of the central trigger. The central trigger selects events with impact parameters less than 3.3 fm, which corresponds to 5% of the total Pb+Pb cross section [Huan97]. From this information, we can calculate the total cross section, which includes the "halo" region where the nuclei interact at impact parameters greater than twice their radii. This non-geometric addition accounts for over half the total cross sectional area and cannot be ignored.

From the information we have about the central trigger, we can calculate the total cross section, A_{total}:

$$f_{central} = \frac{A_{central}}{A_{total}} = 5\%$$

Solving for A_{total}, we get:

$$A_{total} = \frac{\pi(3.3\ fm)^2}{5\%} = 684.2\ fm^2$$

Now we can calculate $A_{medbias}$. Figure B.1 [Huan96] shows the probability of a given event being accepted as a function of impact parameter. This can be very closely approximated by a gaussian:

$$g(b)_{medbias} = 0.88e^{-0.5(\frac{b-7.7}{0.7})^2}$$

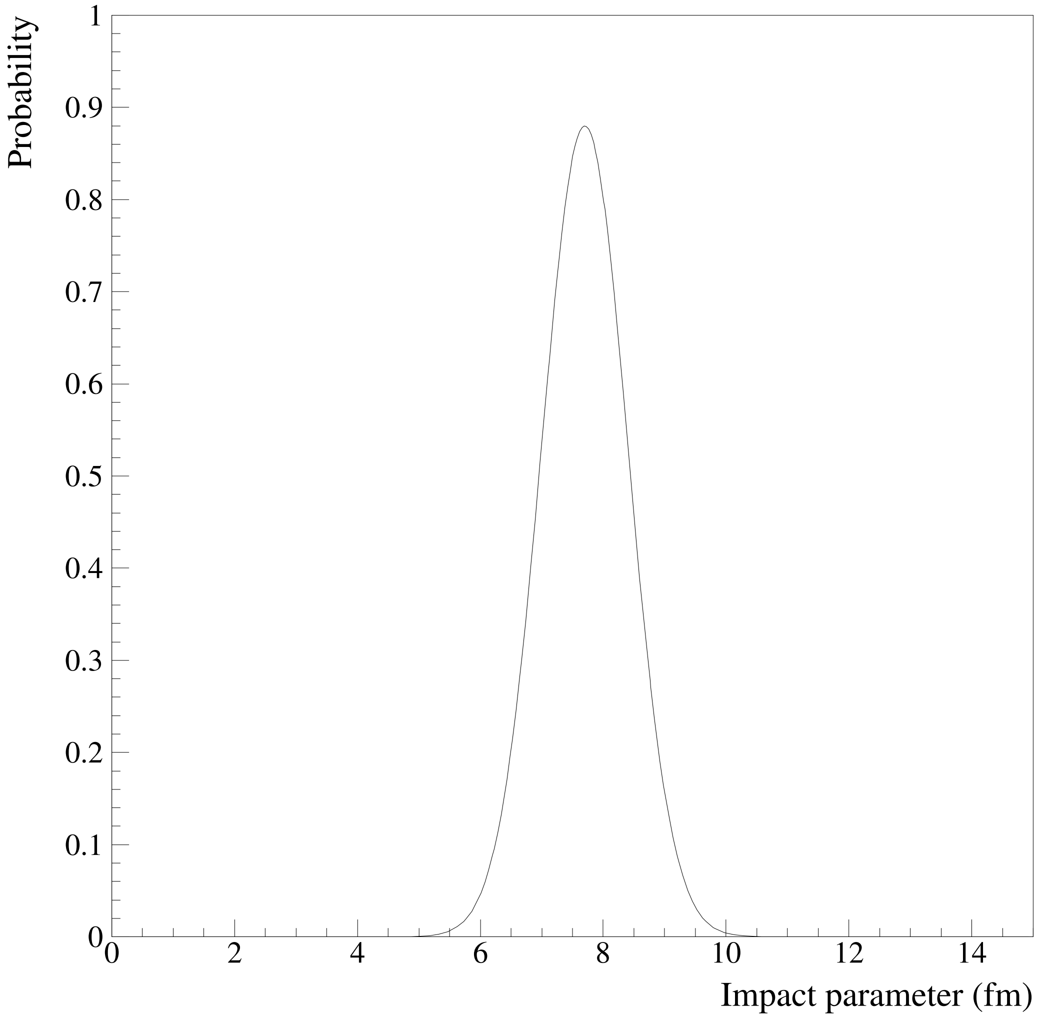

Figure B.1: Medium-bias trigger event acceptance probability [Huan96].

To determine the total cross-sectional area for the medium-bias trigger, we need to integrate this gaussian over total area then divide by A_{total}:

$$A_{medbias} = 2\pi \int_0^{2r_0} g(r)\ r\ dr = 93.9 fm^2$$

$$f_{medbias} = \frac{A_{medbias}}{A_{total}} = \frac{93.9}{984.2} = 13.7\%$$

So the fraction of the total cross section selected by the medium bias trigger is near 14%, as compared with 5% for the central trigger. Although this implies that more events are accepted per spill, each event would be smaller in size than a central event. By selecting an impact parameter range that provided a similar fraction ($\sim$ 5%) of the total cross section, the selected event total storage size was not significantly affected, thus avoiding any need for changes to the data acquisition system for the medium-bias trigger during the 1995 run.

Appendix C

Adding number flow to a particle distribution

Number flow, as described in section 4.2.5, can be added to a random distribution of particles in a simple manner. This is useful for testing programs that analyze data for transverse flow. A common test used in this thesis is to randomize the ϕ of every particle in an event, then adjust its ϕ to add a known amount of number flow to the event. This has the effect of removing any acceptance problems in ϕ, although any p_T acceptance problems remain. Note that the acceptance correction is not necessary and should be set to 1 everywhere for this test.

The number flow signal can be described by the distribution of particles around the event plane, and is easily described (for 1st and 2nd-order terms here) by

$$N = A + B_1 \cos(\mu_1 + \phi) + B_2 \cos(\mu_2 + 2\phi) \tag{C.1}$$

The magnitude of the flow signals is easily described by

$$\frac{B_n}{2A}$$

as in section 5.3. Distributions of equation C.1 for various values of $B_n/2A$ can be seen in figure C.1.

To produce these distributions, the following procedure is used. The particle's ϕ

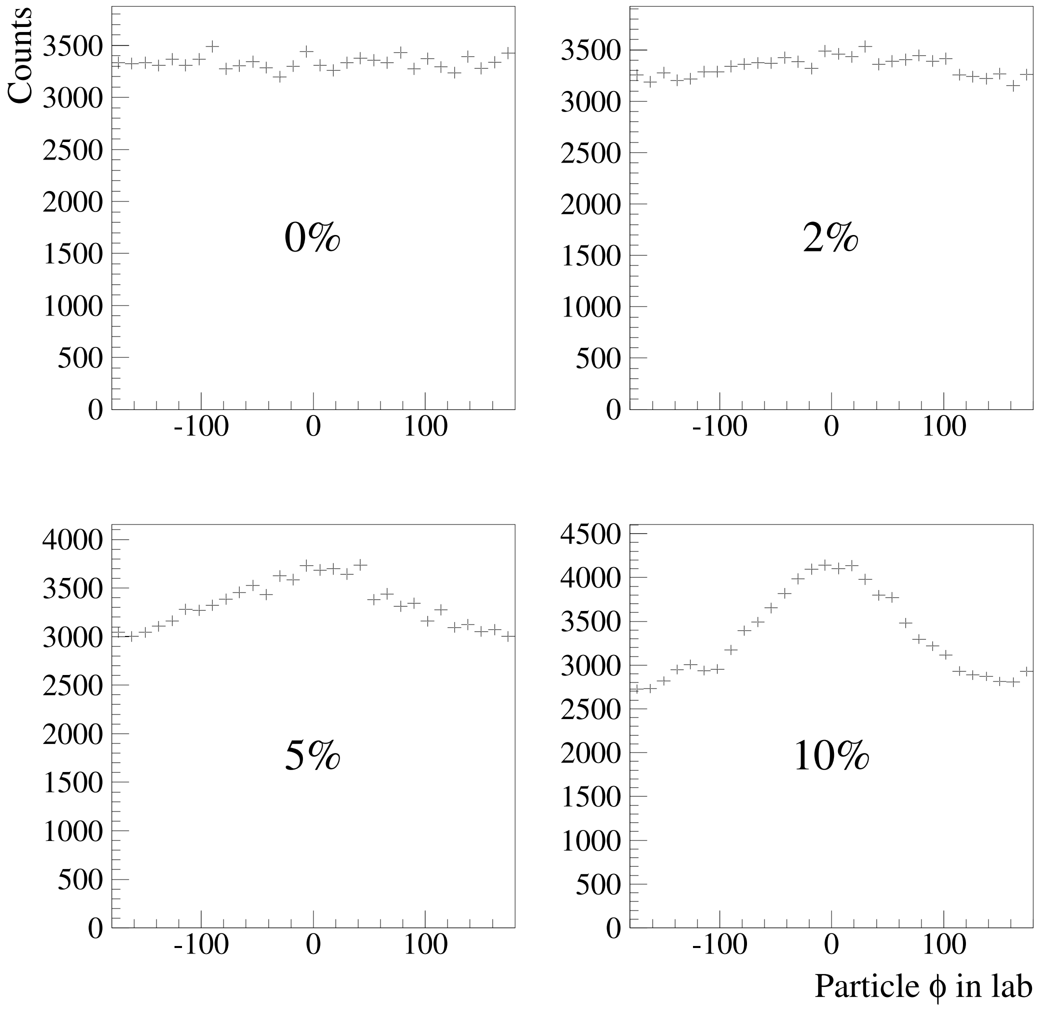

Figure C.1: Distributions of particles in ϕ representing various flow values. In each plot, 100,000 particles were distributed according to equation C.1 to produce the stated number flow signal. The event plane is at 0° for these simulations.

value is modified by the following relation:

$$\phi' = \phi - 2F\sin(\phi) \tag{C.2}$$

where

$$F = \frac{B_n}{2A}$$

A plot of this function for $F = 0.10$ (10% number flow) is given in figure C.2.

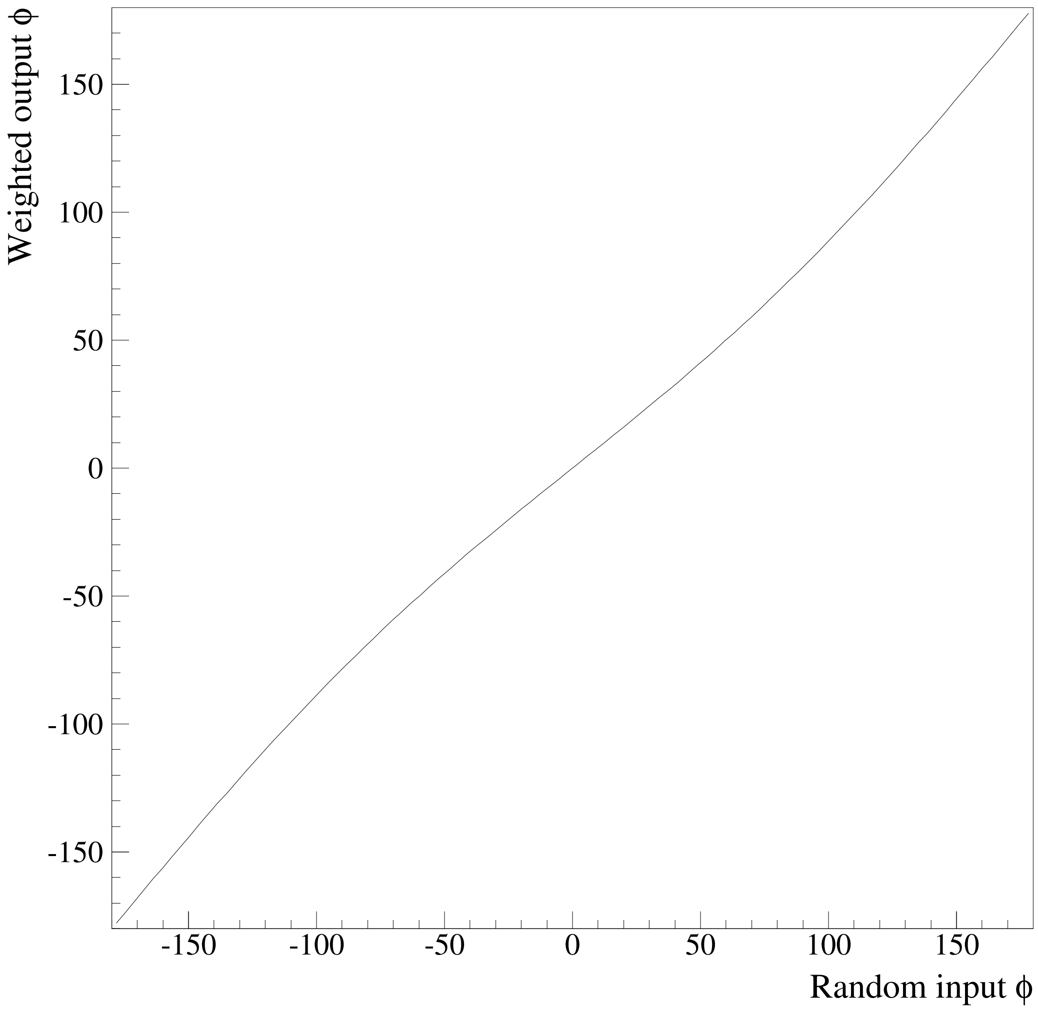

Figure C.2: Function used to provide 10% flow in particle distribution (equation C.2).

Bibliography

[Abre97] M.C. Abreu and the NA50 Collaboration, "Anomalous J/Ψ suppression in Pb-Pb interactions at 158 GeV/c per nucleon", *Physics Letters B* 410(1997):337-43.

[Agga97] M. M. Aggarwal and the WA93 Collaboration, "Azimuthal Anisotropy in S + Au Reaction at 200 A GeV", *Physics Letters B* 403(1997):390-6.

[Ahle98] L. Ahle and the E802/E866 Collaboration, "Proton, deuteron, and triton emission at target rapidity in Au + Au collisions at 10.20A GeV: Spectra and directed flow", *Physical Review C* 57(1998):1416-27.

[Alli80] W. W. M. Allison and J. H. Cobb, "Relativistic Charged Particle Identification by Energy Loss", *Annual Review of Nuclear and Particle Science* 30(1980):253-98.

[Amel89] N. S. Amelin, K. K. Gudima, and V. D. Toneev, "Ultrarelativistic heavy-ion collisions within the independent quark-gluon string model", *The Nuclear Equation of State, Proceedings of the NATO Advanced Study Institute*, Peñiscola, Spain, New York:Plenum Press, 1989.

[Amel90] N. S. Amelin, K. K. Gudima, S. Yu. Sivoklokov and V. D. Toneev, "Further development of the model of quark-gluon strings for the description of high-energy collisions with a target nucleus", *Soviet Journal of Nuclear Physics* 52(1990):172-8.

[Amel91] N. S. Amelin, E. F. Staubo, L. P. Csernai, V. D. Toneev, K. K. Gudima, and D. Strottman, "Transverse Flow and Collectivity in Ultrarelativistic Heavy-Ion Collisions", *Physical Review Letters* 67(1991):1523-6.

[Appe98] H. Appelshäuser and the NA49 Collaboration, "Directed and Elliptic Flow in 158 GeV/Nucleon Pb + Pb Collisions", *Physical Review Letters* 80(1998):4136-40.

[Arfk85] George Arfken, *Mathematical Methods for Physicists*, 3rd edition, San Diego:Academic Press, Inc., 1985.

[Awes96] T.C. Awes and the WA80 Collaboration, "Azimuthal correlations in the target fragmentation region of high energy nuclear collisions", *Physics Letters B* 381(1996):29-34.

[Barr94] J. Barette and the E877 Collaboration, "Observation of Anisotropic Event Shapes and Transverse Flow in Ultrarelativistic Au + Au Collisions", *Physical Review Letters* 73(1994):2532-5.

[Barr97] J. Barette and the E877 Collaboration, "Proton and pion production relative to the reaction plane in Au + Au collisions at 11A GeV/c", *Physical Review C* 56(1997):3254-64.

[Beis96] F. Bieser et al., "Design and Performance of TPC Readout Electronics for the NA49 Experiment", *Nuclear Instruments & Methods in Physics Research A* 385(1996):535-46.

[Bjor83] J. D. Bjorken, "Highly relativistic nucleus-nucleus collisions: The central rapidity region", *Physical Review D* 27(1983):140-51.

[Blai76] J. P. Blaizot, D. Gogney, and B. Grammaticos, "Nuclear Compressibility and Monopole Resonances", *Nuclear Physics A* 265(1976):315-36.

[Brau93] P. Braun-Munzinger and the E877 Collaboration, "Compression, Expansion, and Freeze-Out in Nucleus-Nucleus Collisions at the AGS", *Hot and Dense Nuclear Matter*, edited by W. Greiner et al., Bodrum, Turkey, 1993, New York:Plenum (1993).

[Brow91] G. E. Brown, C. M. Ko, Z. G. Wu, and L. H. Xia, "Kaon production from hot and dense matter formed in heavy-ion collisions", *Physical Review C* 43(1991):1881-92.

[Cask98] W. P. Caskey, M. Anderson, M. Heffner, J. Klay, and D. Cebra, "Collective effects of pions from 2 to 8 GeV/nucleon", Joint APS/AAPT Meeting, Columbus, Ohio, April 1998.

[Cser82] László. P. Csernai, Walter Griner, Horst Stöcker, Isao Tanihata, Shoji Nagamiya, and Jörn Knoll, "Macroscopic nucleon-nucleon correlations caused by the bounce-off process in energetic collisions of heavy nuclei", *Physical Review C*25(1982):5.

[Cser94] László. P. Csernai, *Introduction to Relativistic Heavy Ion Collisions*, Guildford:John Wiley & Sons, 1994.

[Dani83] P. Danielewicz and M. Gyulassy, "Jacobian Free Global Event Analysis", *Physics Letters* 129B(1983):283-8.

[Dani85] P. Danielewicz and G. Odyniec, “Transverse Momentum Analysis of Collective Motion in Relativistic Nuclear Collisions”, *Physics Letters* 157B(1985):146-50.

[DeMa83] C. deMarzo et al., “A segmented photon-hadron calorimeter using a two coloured wavelength shifter optical readout system”, *Nuclear Instruments and Methods* 217(1983):405-17.

[DiBa95] Domenico Di Bari an the WA85 Collaboration, “Results on the production of baryons with $|S| = 1, 2, 3$ and strange mesons in S-W collisions at 200 GeV/c per nucleon”, *Nuclear Physics A* 590(1995):307c-16c.

[Dunn97] Jason Dunn, “Identified Particle Spectra from dE/dx Ionization Measurements in Pb + Pb Collisions at 158 A·GeV/c”, doctoral thesis, University of California at Davis, June 1997.

[Esum97] S. Esumi, S. Chapman, H. van Hecke, and Nu Xu, “Transverse flow at ultrarelativistic energies”, *Physical Review C* 55(1997):R2163-6.

[Fai87] George Fai and Wei-ming Zhang, “Optimizing heavy ion experiments to probe dense nuclear matter”, *Physical Review C* 36(1987):597-601.

[Ferg95] M. I. Ferguson and H. G. Fischer, “A Brief Explanation of Kalib Factors”, NA49 internal note #68, 1995.

[Fern86] Richard Fernow, *Introduction to experimental particle physics*, New York:Cambridge University press, 1986.

[Ferm40] Enrico Fermi, “The Ionization Loss of Energy in Gases and in Condensed Materials”, *Physics Review* 57(1940):485-93.

[Fire96] Richard B. Firestone, Virginia S. Shirley, editor, *Table of Isotopes, Eighth Edition*, New York:John Wiley and Sons, 1996.

[Gavi97] Sean Gavin and Ramona Vogt, “Charmonium Suppression by Comover Scattering in Pb + Pb Collisions”, *Physical Review Letters* 78(1997):1006-9.

[Gazd98] Marek Gazdzicki and Mark I. Gorenstein, “On the Early Stage of Nucleus-Nucleus Collisions” NA49 internal note #155, 1998.

[Glen89] Norman K. Glendenning, “Neutron Stars, Fast Pulsars, Supernovae and the Equation of State of Dense Matter”, *The Nuclear Equation of State, Proceedings of the NATO Advanced Study Institute*, Peñiscola, Spain, New York:Plenum Press, 1989.

[Gunt94] J. Günther, "Particle Identification by *dE/dx* in the NA35 Time Projection Chamber", internal report IKF-HENPG/8-94(1994), Institut Für Kernphysik, Universität Frankfurt.

[Gust84] H. A. Gustafsson, H. H. Gutbrod, B. Kolb, H. Löhner, B. Ludewigt, A. M. Poskanzer, T. Renner, H. Riedesel, H. G. Ritter, A. Warwick, F. Weik, and H. Wieman, "Collective Flow Observed in Relativistic Nuclear Collisions", *Physical Review Letters* 52(1984):18.

[Gust88] H. A. Gustafsson and the Plastic Ball Collaboration, "Energy and multiplicity depenence of fragment flow in high energy nuclear collisions", *Modern Physics Letters A* 3(1988):1323-32.

[Gutb90] H. H. Gutbrod, K. H. Kampert, B. Kolb, A. M. Poskanzer, H. G. Ritter, R. Schicker, and H. R. Schmidt, Squeeze-out of nuclear matter as a function of projectile energy and mass", *Physical Review C* 42(1990):640-51.

[Harr96] John W. Harris and Berndt Müller, "The Search for the Quark-Gluon Plasma", *Annual Review of Nuclear and Particle Science* 46(1996):71-107.

[Hemm96] T. K. Hemmick and the E877 Collaboration, "Flow Studies at 10.8 GeV/nucleon", *Nuclear Physics A*610(1996):63c-75c.

[Huan96] Isaac Huang, private correspondence, 1996.

[Huan97] Isaac Huang, "Global and Collective Phenomena in Pb+Pb Collisions at Projectile Energy of 158 GeV/nucleon", doctoral thesis, University of California at Davis, June 1997.

[Jahn94] A. Jahns, C. Spieles, H. Sorge, H. Stöcker, and W. Greiner, "'Antiflow' of antiprotons in Heavy Ion Collisions", *Physical Review Letters* 72(1994):3464-7.

[Judd95] E. G. Judd and the NA36 Collaboration, "Recent results from the NA36 experiment", *Nuclear Physics A* 590(1995):291c-306c.

[Kaha97] D. E. Kahana, Y. Pang, and E. Shuryak, "Flow at Brookhaven AGS Energy (11.6 GeV/nucleon): A barometer for high density effects?", *Physical Review C* 56(1997):481-5.

[Kars95] F. Karsch, "The Phase Transition of the Quark Gluon Plasma: Recent Results from Lattice Calculations", *Nuclear Physics A* 590(1995):367c-82c.

[Kint95] J. C. Kintner, "Squeeze-out and Flow of Pions from 1.15 GeV/nucleon Au + Au", doctoral thesis, University of California at Davis, June 1995.

[Kint97] J. C. Kintner and the EOS Collaboration, "Pion flow and antiflow in 1.15 A GeV Au+Au", *Physical Review Letters* 78(1997):4165-8.

[Laer96] E. Laermann, "Recent Results from Lattice QCD Simulations", *Nuclear Physics a* 610(1996):1c-12c.

[Land53] L. D. Landau and I. Akad, *Nauk. SSSR, Ser. Fitz.* 17(1953):51 (see also *Collected Papers of L. D. Landau*, New York:Gordon and Breach, 1965).

[Lasi97] "Particle Identificaton in the NA49 TPCs", *Proceedings from Frontier Detectors for Frontier Physics*, 7th Pisa Meeting on Advanced Detectors, May 25-31, 1997.

[Latt96] J. M. Lattimer, "The Nuclear Equation of State and Supernovae", *Lecture Notes of the Workshop on Nuclear Equation of State*, Puri, India, 1994, Singapore:World Scientific, 1996.

[Lete92] Jean Letessier and Ahmed Tounsi, "Hot hadronic matter and strange anti-baryons", *Physics Letters B* 292(1992):417-23.

[Li96] Bao-An Li and C. M. Ko, "Excitation functon of compression and collective flow in central Au + Au reactions from Bevalac/SIS to AGS", *Advances in Nuclear Dynamics 2*, New York:Plenum Press, 1996.

[Li95] G. Q. Li, C. M. Ko, and Bao-An Li, "Kaon Flow as a Probe of the Kaon Potential in Nuclear Medium", *Physical Review Letters* 74(1995):235-8.

[Liu97] Heng Lui and the E895 Collaboration, *Quark Matter '97 Proceedings*, to be published in *Nuclear Physics A*.

[Mats86] T. Matsui and H. Satz, "J/psi suppression by quark-gluon plasma formation", *Physics Letters B* 178(1986):416-22.

[Naga81] S. Nagamiya, M.-C. Lemaire, E. Moeller, S. Schnetzer, G. Shapiro, H. Steiner, and I. Tanihata, "Production of pions and light fragments at large angles in high-energy nuclear collisions", *Physical Review C* 24(1081):971-1009.

[Ogil98] Craig Ogilvie, "In-medium kaon properties", seminar, University of California at Davis, April 30, 1998.

[Olli92] J. Y. Ollitrault, "Anisotropy as a signature of transverse collective flow", *Physical Review D* 46(1992):229-45.

[Olli93] J. Y. Ollitrault, "Determination of the reaction plane in ultrarelativistic nuclear collisions", *Physical Review D* 48(1993):1132-9.

[Olli95] J. Y. Ollitrault, “Collective flow from azimuthal correlations”, *Nuclear Physics A*590(1995):561c-564c.

[Olli97] J.-Y. Ollitrault, “On the measurement of azimuthal anisotropies in nucleus-nucleus collisions”, SPIRES preprint nucl-ex/9711003(1997).

[Part95] M. D. Partlan and the EOS Collaboration, “Fragment Flow in Au + Au Collisions”, *Physical Review Letters* 75(1995):2100-3.

[Pear91] J. M. Pearson, “The incompressibility of nuclear matter and the breathing mode”, *Physics Letters B* 271(1991):12-16.

[Posk98] A. M. Poskanzer and S. A. Voloshin, “Methods for analyzing ansiotropic flow in relativistic nuclear collisions”, submitted to *Physical Review C*.

[Prat98] Scott Pratt and Joelle Murray, “Modeling the breakup stage of relativistic heavy-ion collisions”, *Physical Review C* 57(1998):1907-19.

[Rai90] G. Rai and the EOS Collaboration, “A TPC detector for the study of high multiplicity heavy ion collisions”, *IEEE Transactions on Nuclear Science* 37(1990):56-64.

[Rauc94] Wolfgang Rauch, “The NA49 Data Acquisition System”, *IEEE Transactions on Nuclear Science* 41(1994):30-6.

[Reis96] W. Reisdorf and the FOPI Collaboration, “Central collisions of Au on Au at 150, 250, and 400 A·MeV”, *Nuclear Physics A* 612(1996):493-556.

[Reis98] W. Reisdorf and H. G. Ritter, “Collective Flow in Heavy-Ion Collisions”, *Annual Review of Nuclear and Particle Science* 47(1997):663-709.

[Renf84] R. E. Renfordt, D. Schall, R. Bock, R. Brockmann, J. W. Harris, A. Sandoval, R. Stock, H. Ströbele, D. Bangert, W. Rauch, G. Odyniec, H. G. Pugh, and L. S. Schroeder, “Stopping Power and Collective Flow of Nuclear Matter in the Reaction Ar+Pb at 0.8 GeV/u”, *Physical Review Letters* 53(1984):8.

[Risc96] Dirk H. Rischke, “Hydrodynamics and collective behavior in relativistic nuclear collisions”, *Nuclear Physics a* 610(1996):88c-101c.

[Ritm95] J. L. Ritman and the FOPI Collaboration, “On the transverse momentum distribution of strange hadrons produced in relativistic heavy ion collisions”, *Zeitschrift Für Physik A* 352(1995):355-357.

[Sche74] W. Scheid, H Müller, and W. Greiner, “Nuclear Shock Waves in Heavy-Ion Collisions”, *Physical Review Letters* 32(1971):741-5.

[Siem79] Philip J. Siemens and John O. Rasmussen, “Evidence for a Blast Wave from Compressed Nuclear Matter”, *Physical Review Letters* 42(1979):880-3.

[Sorg89] “Covariant Nonequilibrium Dynamics And The Search For The Quark Gluon Plasma In Ultrarelativistic Nucleus-Nucleus Collisions”, *The Nuclear Equation of State, Proceedings of the NATO Advanced Study Institute*, Peñiscola, Spain, New York:Plenum Press, 1989.

[Sorg97] Heinz Sorge, “Elliptical Flow: A Signature for Early Pressure in Ultrarelativistic Nucleus-Nucleus Collisions”, *Physical Review Letters* 78(1997):2309-12.

[Spie98] C. Spieles, H. Stöcker, and C. Greiner, “Phase transition of a finite quark-gluon plasma”, *Physical Review C* 57(1998):908-15.

[Stau89] E. F. Staubo, A. K. Holme, L. P. Csernai, M. Gong, and D. Strottman, “ Pion distributions from the fluid dynamical model of ultra-relativistic heavy ion collisions.”, *Physics Letters B* 229(1989):351-8.

[Stöc86] Horst Stöcker and Walter Greiner, “High energy heavy ion collisions – probing the equation of state of highly excited hadronic matter”, *Physics Reports* 137(1986):277-392.

[Ster71] R. M. Sternheimer and R. F. Peierls, “General Expression for the Density Effect for the Ionization Loss of Charged Particles”, *Physics Review B* 3(1971):3681-92.

[Vogt91] R. Vogt, S. J. Brodsky and P. Hoyer, “Systematics of J/psi production in nuclear collisions”, *Nuclear Physics B* 360(1991):67-96.

[Volo96] S. Voloshin and Y. Zhang, “Flow study in relativistic nuclear collisions by Fourier expansion of azimuthal particle distributions”, *Zeitschrift Für Physik C* 70(1996):665-71.

[Wein96] T. Wienold and the NA49 Collaboration, “Stopping and Collective Effects at SPS Energies”, *Nuclear Physics A* 610(1996):76c-87c.

[Wern87] K Werner, J. Hufner, M. Kutschera, and O. Nachtmann, “Particle production in hadron-nucleus collisions at 100 GeV from a parton-string shell”, *Zeitschrift fur Physik C* 37(1987):57-67.

[Wern88] K Werner, “analysis of proton-nculeus and nucleus-nucleus scattering at 200 *A* GeV by the multistring model VENUS”, *Physics Letters B* 208(1988):520-4.

[West90] G. WEstfall et al., “Event-shape analysis: sequention versus simultaneous multifragment emission”, *Physical Review Letters* 64(1990):2246-9.

[Wong94] Cheuk-Yin Wong, *Introduction to High-Energy Heavy-Ion Collisions*, Singapore:World Scientific Publishing, 1994.